

TRANSITION FROM LAMINAR TO TURBULENT FLOW IN NON-NEWTONIAN CHANNEL  
FLOWS: THE IMPACT OF DRAG REDUCING POLYMER ADDITIVES  
by

Ali Fathizadeh

A thesis submitted in partial fulfillment of the requirements for the degree of

Master of Science

Department of Mechanical Engineering  
University of Alberta

© Ali Fathizadeh, 2023

## Abstract

This thesis investigates the effect of a drag-reducing polymer on laminar-turbulent transition in a gravity-driven channel flow. The drag-reducing polymer is polyacrylamide (PAM) dissolved in water at concentrations of 50, 75, 100, and 150 parts per million (ppm). An extensive experimental campaign utilizing particle image velocimetry is conducted to measure the velocity field in streamwise-wall-normal and streamwise-spanwise planes across a range of Reynolds numbers ( $Re$ ). The transition to turbulence is delayed by the introduction of PAM, with the delay increasing with the relaxation time of the polymer solution.

For low PAM concentrations of 50 and 75 ppm, the skin friction coefficient ( $C_f$ ) increases with increasing  $Re$  before the onset of drag reduction around  $Re = 2500$ . After the drag reduction onset,  $C_f$  values will decline with further increase in  $Re$ . The transitional flow structures in the streamwise-wall-normal plane resemble Newtonian turbulence, containing recognizable turbulent spots. In the streamwise-spanwise plane, the turbulent core appears connected to chaotic streaks attached to the leading edge of the spot.

In contrast, the higher PAM concentrations of 100 and 150 ppm display substantially different transitional physics. The  $C_f$  values depart the laminar trend at  $Re \approx 3000$ , approaching the maximum drag reduction asymptote without demonstrating an onset point. The solutions undergo a remarkably smoother transition spanning over a  $Re$  range of approximately 1000 units. Turbulent spots are minimal, and elongated streamwise streaks dominate the flows instead.

Analysis of turbulence statistics reveals concentration-dependent modifications. At 50 and 75 ppm, turbulence intensity matches the Newtonian value of around 1% in laminar regions between turbulent spots. However, at 100 and 150 ppm, the intensity grows to 1.7% in laminar regions, indicating enhanced fluctuations. Within turbulent regions, intensity declines from 5% in Newtonian cases to 3% at 150 ppm, suggesting substantial turbulence attenuation.

In summary, this thesis demonstrates the impact of polymer additives on transitional channel flows. The additives expand the transitional regime and transform the emergence of coherent structures in a concentration-dependent manner, as evidenced by elongated streaks dominating at higher concentrations.

## **Preface**

The research, experiments and analysis described in this thesis were carried out by me under the supervision of Dr. Sina Ghaemi in the Department of Mechanical Engineering at the University of Alberta. The results from this study are currently being prepared for submission to a peer-reviewed journal. I have written the entirety of both this thesis document and the manuscript under the guidance of my supervisor. In this document, the content and structure conform to the requirements for a thesis while retaining the core ideas and results from my research work which will appear in further publications.

## **Acknowledgments**

I would like to express my gratitude to my supervisor, Dr. Sina Ghaemi, for his invaluable guidance and feedback throughout this research project.

I also wish to thank Lucas Warwaruk and Joel Fenske for their assistance with rheology measurements, as well as my fellow research group members for creating a collaborative environment.

Most importantly, I wish to profoundly thank my family and friends for their unwavering love, patience and steadfast support throughout my studies. To my parents, Niloofar, my brother, and loved ones - thank you for always believing in me, inspiring me, and being my foundation. Your encouragement gave me strength during the most difficult times of this journey. I am forever grateful.

# Table of Contents

1. Introduction.....	1
1.1 Motivation .....	1
1.2 Thesis Overview .....	3
2. Literature Review.....	4
2.1 Laminar-Turbulent Transition in Newtonian Flows.....	4
2.1.1 Coherent Structures in Transition .....	5
2.1.2 Critical Reynolds Number.....	11
2.2 Laminar-Turbulent Transition in Non-Newtonian Flows .....	14
2.3 Elasto-Inertial Turbulence .....	24
3. Experimental Methodology .....	28
3.1 Flow Facility.....	29
3.2 Polymer solution preparation.....	35
3.3 Rheology measurements.....	37
3.3.1 Shear viscosity measurements.....	37
3.3.2 Extensional rheology measurements.....	39
3.4 Particle image velocimetry (PIV).....	44
3.4.1 Long-duration wall-normal PIV .....	45
3.4.2 Time-resolved wall-normal PIV.....	46

3.4.3	Long-duration spanwise PIV.....	47
3.5	Laminar/Turbulent Detection.....	48
3.6	Uncertainty Analysis.....	51
4.	Results.....	57
4.1	Transition in Newtonian channel flow.....	58
4.2	Transition for low-concentration PAM solutions.....	71
4.3	Transition for high-concentration PAM solutions.....	84
5.	Discussion.....	98
6.	Conclusions.....	105
6.1	Future Work.....	107
	Bibliography.....	109
	Appendices.....	118
A	MATLAB Code for Laminar/Turbulent Detection.....	118
B	Technical Drawings of the Flow Facility.....	120

## List of Tables

Table 1 Notable Investigations on critical $Re$ in pipe and channel flows. ....	13
Table 2 Experimental studies on laminar to turbulent transition of polyacrylamide solutions .....	23
Table 3 Valve Openings Tested for Each Solution .....	34
Table 4 Measured rheological parameters for experimented solutions .....	43
Table 4 Estimated total uncertainties associated with independent flow variables. ....	56
Table 5 Estimated total uncertainties associated with calculated flow variables.....	56

## List of Figures

Figure 2.1 Turbulent spot as observed by Carlson <i>et al.</i> (1982).....	9
Figure 2.2 Turbulence spatial variation as observed by Sano & Tamai (2016).....	10
Figure 2.3 The parameter space of turbulence in dilute polymer solutions.....	27
Figure 3.1 Annotated schematic view of the experimental facility.....	31
Figure 3.2 Molecular structure of polyacrylamide.....	35
Figure 3.3 Schematic of the cone and plate rheometer.....	38
Figure 3.4 The relationship between shear rate and apparent viscosity.....	39
Figure 3.5 Schematic of the dripping-onto-substrate (DoS) setup.....	40
Figure 3.6 Semi-logarithmic plot of filament diameter as a function of time.....	42
Figure 3.7 Laminar/turbulent identification technique of water flow.....	51
Figure 4.1 Skin friction factor ( $C_f$ ) for water flow versus Reynolds number.....	61
Figure 4.2 The turbulent fraction ( $F_T$ ) for water as a function of Reynolds number...	63
Figure 4.3 Spatial contours of normalized streamwise velocity ( $U/\langle U_c \rangle$ ) from streamwise-wall-normal PIV measurements of water flow.....	65
Figure 4.4 Spatial contours of normalized streamwise velocity ( $U/\langle U_c \rangle$ ) from streamwise-spanwise PIV measurements of water flow.....	68
Figure 4.5 The velocity profiles for various turbulent fractions of water flow.....	71
Figure 4.6 Skin friction factor ( $C_f$ ) for 50 ppm PAM flow versus Reynolds number.	72
Figure 4.7 Skin friction factor ( $C_f$ ) for 75 ppm PAM flow versus Reynolds number .	74
Figure 4.8 The turbulent fraction ( $F_T$ ) for 50 ppm solutions of PAM versus the Reynolds number.....	75



Figure 4.9 The turbulent fraction ( $F_T$ ) for 75 ppm solutions of PAM versus the Reynolds number .....	77
Figure 4.10 Spatial contours of normalized streamwise velocity ( $U/\langle U_c \rangle$ ) from streamwise wall-normal PIV measurements of low-concentration PAM solutions .....	78
Figure 4.11 Spatial contours of normalized streamwise velocity, ( $U/\langle U_c \rangle$ ), from streamwise spanwise PIV measurements of low-concentration PAM solutions .....	80
Figure 4.12 The velocity profile for laminar, transitional and turbulent cases for low-concentration solutions .....	83
Figure 4.13 Skin friction factor ( $C_f$ ) for 100 ppm PAM flow versus Reynolds number .....	85
Figure 4.14 Skin friction factor ( $C_f$ ) for 150 ppm PAM flow versus Reynolds number .....	86
Figure 4.15 The turbulent fraction ( $F_T$ ) for 100 ppm solutions of PAM versus the Reynolds number .....	87
Figure 4.16 The turbulent fraction ( $F_T$ ) for 150 ppm solutions of PAM versus the Reynolds number .....	89
Figure 4.17 Spatial contours of normalized streamwise velocity ( $U/\langle U_c \rangle$ ) from streamwise wall-normal PIV measurements of high-concentration PAM solutions .....	91
Figure 4.18 Spatial contours of normalized streamwise velocity, ( $U/\langle U_c \rangle$ ), from streamwise spanwise PIV measurements of high-concentration PAM solutions .....	94
Figure 4.19 The velocity profiles for laminar, DOSttransitional and turbulent cases for high-concentration PAM solution .....	97

Figure 5.1 Turbulence intensity (TI) separated for laminar and turbulent parts of flow field .....	102
Figure 5.2 Our data for all five solutions in Weissenberg number and Reynolds number space.....	104

# 1. Introduction

## 1.1 Motivation

Turbulent flows are ubiquitous in nature and engineering applications, from ocean currents to airplane wings. Turbulence arises from instabilities in laminar flows as the Reynolds number ( $Re$ ) increases past a critical point, initiating a transition to chaotic and irregular motion. This laminar-turbulent transition process is complex and a longstanding topic of fluid mechanics research dating back to the pioneering work of Reynolds (1883). While much progress has been made, gaps remain in understanding key aspects of the transition physics.

In wall-bounded shear flows like pipes and channels, the transition is characterized by localized turbulent regions (spots, streaks, puffs) emerging within the laminar flow. The gradual proliferation and merging of these coherent structures ultimately leads to fully turbulent flow (Corrsin 1943; Emmons 1951; Wygnanski & Champagne 1973).

However, the specific transitional structures and evolution pathway varies for different flow geometries and fluids.

Significant complications arise when viscoelastic polymer additives are introduced typically for drag-reduction applications. Even trace amounts of flexible polymers can dramatically alter the transition process and turbulence dynamics through elastic turbulence mechanisms. Polymers are observed to delay and smooth the transition, expand the transitional regime over a wider Reynolds number range, and modify the coherent structures that emerge (Virk 1975; White & Mungal 2008). Yet many open questions persist regarding polymer effects on transitional flows.

Advancing the fundamental knowledge in this area will aid the optimization of polymeric drag reduction and efforts to control turbulence for energy savings. Furthermore, non-Newtonian fluids are widely encountered in applications, so improved transition understanding is invaluable for predicting behaviour in industrial flows. Therefore, extensive research focused explicitly on mapping polymer impacts on transitional statistics, critical parameters, coherent structures, and flow morphology is imperative.

The primary objective of this thesis is to elucidate the effects of polymer additives on the transitional flow physics of rectangular channel flows. While prior studies have explored polymer impacts in pipe geometries, little is known about how dilute polymer solutions modify the emergence of coherence structures and evolution of turbulence statistics during transition in channel flows. This work aims to address this knowledge gap through extensive PIV measurements and analysis of critical

parameters. The outcomes are expected to provide new insights into polymer transition delay mechanisms and differences compared to Newtonian fluid behavior in canonical channel flows.

## **1.2 Thesis Overview**

This thesis systematically investigates the influence of polymer additives on laminar-turbulent transition in rectangular channel flows. The fluids examined include a Newtonian solvent and dilute solutions of a flexible polymer, polyacrylamide (PAM), at various concentrations. The study utilizes time-resolved particle image velocimetry to quantify flow statistics and visualize transitional flow fields in streamwise wall-normal and spanwise planes.

The thesis is structured as follows: Chapter 2 reviews relevant literature on transitional flows and polymer effects. Chapter 3 details the experimental methods. Chapter 4 presents results for the Newtonian fluid and polymer solutions. The evolution of skin friction, turbulence fraction, velocity profiles, and flow morphology are analyzed across a range of Reynolds numbers spanning laminar, transitional, and turbulent regimes. Chapter 5 discusses the key findings regarding polymer impacts on the transitional statistics, critical parameters, coherence structures, and flow fields compared to the Newtonian fluid. Finally, Chapter 6 summarizes the conclusions.

## **2. Literature Review**

### **2.1 Laminar-Turbulent Transition in Newtonian Flows**

The study of laminar to turbulent flow transition in shear flows has been a prominent area of research within fluid mechanics, originating from Reynolds's (1883) groundbreaking experiment. Since then, a substantial body of literature has emerged, delving into the instability and laminar-turbulent transition in shear flows, with numerous publications contributing to the evolving comprehension of this phenomenon (Eckhardt *et al.* 1998; Manneville 2016). The broad applicability of wall-bounded flows has accentuated the significance of identifying the "critical Reynolds number" at which this transition occurs.

This literature review commences with an introduction to transitional flow structures, accompanied by a succinct summary of their key attributes. Following this, a brief exploration of various approaches for determining the critical Reynolds number in pipe and channel flows is presented.

### **2.1.1 Coherent Structures in Transition**

At the initial stage of turbulence, localized regions of turbulent flow are encircled by laminar flow. These flow formations, known as coherent structures, are integral to the transition process. The shift from laminar to turbulent flow is contingent upon the growth or decay of these coherent structures.

Coherent structures were first identified during the transition process in a boundary-layer flow and were designated as "Turbulent Spots" by Emmons (1951). However, the recognition of various structures has been found to be dependent on factors such as the type of flow, Reynolds number, and the level of disturbance.

#### **2.1.1.1 Pipe Flows:**

In the 1970s, the concept of coherent structures in pipe flow was first seriously discussed, beginning with Wygnanski and Champagne's (1973) experimental study on transitional pipe flows. They conducted hot-wire measurements in a smooth air pipe with a diameter of 3.3 cm, covering a  $Re$  range of 1,000 to 100,000. Their research identified two distinct transitional structures: "slugs" and "puffs."

Slugs are observed at high  $Re$  values and are caused by minor disturbances in the pipe's inlet region. In contrast, puffs are generated by significant disturbances at the inlet and can appear at relatively lower  $Re$  values. According to Wygnanski and Champagne (1973), the flow within a slug closely resembles the fully developed turbulent flow. Slugs exhibit well-defined interfaces, termed "Leading Edge" and "Trailing Edge," between the turbulent flow inside and the surrounding laminar flow.

As slugs grow, they can occupy a significant portion of the pipe, resulting in a fully turbulent pipe flow.

In the subsequent years, Wygnanski and colleagues (1975) expanded their research to investigate puffs. The experimental setup was modified to incorporate a speaker on the funnel to generate disturbances. The study was carried out within a  $Re$  range of 2,000 to 3,500. The researchers found that the length of the puff is dependent on the  $Re$ , with all puffs at the same  $Re$  having equal lengths. Moreover, as the flow moves downstream towards the puff's rear, the turbulent intensity gradually increases, reaching its maximum at the trailing edge. However, the researchers were unable to identify a distinct interface between turbulent and non-turbulent regions near a puff's leading edge. Further analysis showed that a puff travels at a velocity approximately equal to the pipe's spatial average velocity.

Avila *et al.* (2011) conducted a thorough investigation of puffs in transitional pipe flow, utilizing both experimental and numerical analysis techniques. The researchers selected a pipe diameter of 4 mm and introduced impulsive perturbation to the fully developed laminar flow using a water jet. To experimentally identify and track a puff, pressure was measured at two downstream locations. The acquisition of pressure signals enabled them to determine whether the turbulent fraction of the flow increased, remained constant, or decreased during downstream propagation.

In their numerical analysis, Avila *et al.* (2011) employed direct numerical simulations (DNS) and investigated  $Re$  ranging from 2,032 to 2,385. The numerical simulations corroborated previous observations regarding the leading edge and



trailing edge interfaces of a puff. Avila *et al.* (2011) noted that the upstream boundary of a puff is well-defined, while the downstream boundary is less distinct. They further explained that the increase in turbulence arises from the spatial proliferation of turbulent patches, rather than the temporal complexity of fluid motion. This spatial proliferation was termed "puff splitting." When a puff extends in length to the point where vorticity decays in its central streamwise region, a vorticity patch escapes from the primary puff and forms a new puff. As mentioned earlier, slugs grow in size, while puffs primarily increase in number. Consequently, spatial proliferation serves as another distinguishing factor between puffs and slugs.

Barkley *et al.* (2015) utilized a combination of experimental, theoretical, and computational methods to study the emergence of fully turbulent flow in pipes and ducts. The pipe had a diameter of 10 mm, while the duct had a width of 5 mm. The disturbance generation technique and pressure sensing equipment were similar to those employed by Avila *et al.* (2011). However, for the duct experiments, five pressure sensors were placed at various downstream points. Barkley and colleagues (2015) demonstrated that in both pipe and duct flows, the velocity of the downstream front of a turbulent patch is indistinguishable from the upstream front, indicating localized turbulence at the onset. For pipe flow with  $Re \gtrsim 2,250$  and duct flow with  $Re \gtrsim 2,030$ , the speed of the downstream front increases with the  $Re$ . These values represent the threshold at which turbulence begins to aggressively invade the surrounding laminar fluid.

### 2.1.1.2 Channel Flows:

The visualization of turbulent spots in channel flow has been the subject of early experimental investigations by Carlson *et al.* (1982) and Alavyoon *et al.* (1986). It is worth noting that channel flow and plane Poiseuille flow (PPf) are often treated as the same type of flow in literature due to their similarities. Interestingly, both channel flow and PPf studies are conducted in channel facilities, but PPf studies aim to use channels with higher aspect ratios (the ratio of width to height in channel cross-section) to simulate the infinite plane assumption of Poiseuille flow.

In their study, Carlson *et al.* (1982) investigated the visualization of turbulent spots in plane Poiseuille flow by artificially triggering a transition. To achieve this, they used titanium dioxide-coated mica particles for flow visualization inside a water channel with an aspect ratio of 133. The flow was disturbed by an electromagnetic solenoid, and the resulting turbulent spot is shown in Figure 2.1. The turbulent spot in channel flow has an arrowhead shape, with oblique waves visible at the sides and rear of the spot, as observed by Carlson *et al.* (1982). They also noted that as the turbulent spot travels downstream, it becomes more spread out (primarily in the spanwise direction) until it eventually divides into two separate turbulent spots at sufficiently large  $Re$ . The oblique waves around the turbulent spot resemble those observed in boundary layer flows, but the splitting of coherent structures has not been reported in boundary layers. This is likely due to the bounded geometry of transitional channel flow, which results in an energy transfer mechanism more similar to pipe flow.

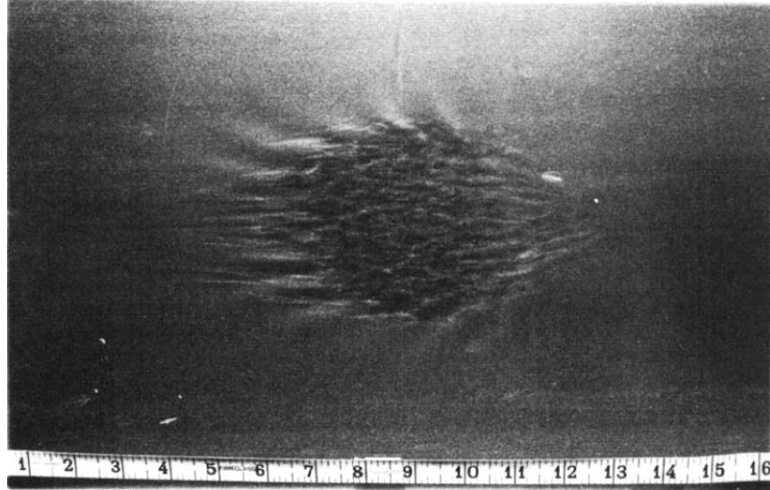


**Figure 2.1 Turbulent spot as observed by Carlson *et al.* (1982). Flow direction from left to right,  $Re = 1000$  and the scale indicates the distance from the disturbance in inches.**

In a subsequent study, Alavyoon *et al.* (1986) expanded upon the work of Carlson *et al.* (1982) by investigating the spreading rate and propagation velocities of turbulent spots over a wider range of  $Re$ . Two channels with aspect ratios of 277 and 166 were used, and the  $Re$  range was from 1,100 to 2,200 based on half-channel height. The flow visualization technique employed was similar to that used by Carlson *et al.* (1982). Interestingly, it was observed that, unlike turbulent spots in the boundary layer, turbulent spots in channel flow lose their arrowhead shape and become concave as they travel downstream. Additionally, the researchers concluded that the ratio between the front and rear propagation velocities of the spot increases with  $Re$ .

In a more recent study, Sano & Tamai (2016) conducted an experimental investigation of transitional channel flow. The channel used in the study had an aspect ratio of 180, and metal-coated mica platelets were employed for flow visualization.

The researchers injected artificial perturbations into the flow at the inlet, which either decayed or spread downstream depending on the  $Re$ . Snapshots of the flow visualization are presented in Figure 2.2.

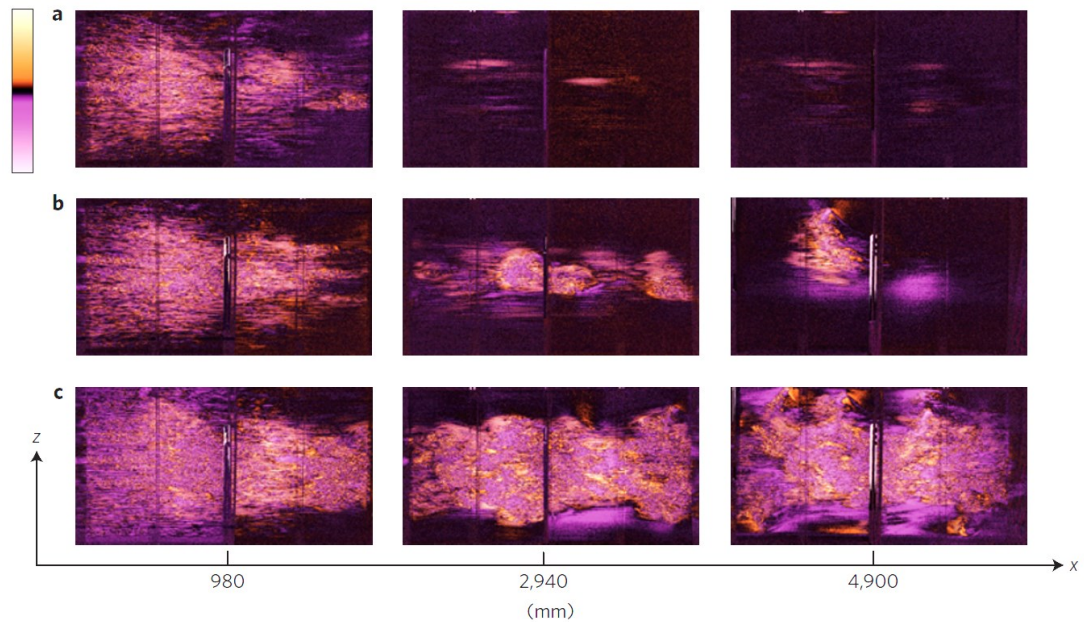


**Figure 2.2 Turbulence spatial variation as observed by Sano & Tamai (2016). Dark regions represent laminar and bright regions show turbulent flow. Mean flow from left to right and the horizontal axis shows the distance from the perturbation. (a)  $Re = 798$ , (b)  $Re = 842$  and (c)  $Re = 1005$**

Figure 2.2(a) shows that for  $Re = 798$  (calculated based on channel half-height and centerline velocity), the injected perturbation separated into localized turbulent spots that quickly decayed as they propagated downstream. However, for  $Re$  greater than approximately 830, the researchers observed the splitting and spreading of turbulent

spots, as depicted in Figure 2.2(b). For sufficiently large Reynolds numbers, such as  $Re \gtrsim 900$ , the turbulent flow was sustained, as shown in Figure 2.2(c).

### 2.1.2 Critical Reynolds Number

Because of the gradual nature of the transition process, defining an explicit critical Reynolds number is intricate. As discussed in the previous section, localized patches of turbulent flow emerge in transitional wall-bounded flows, and they will either decay or grow depending on the  $Re$ . It is widely accepted to define the critical Reynolds number as a  $Re$  at which turbulence becomes sustained. Below we will introduce some studies that attempted to find the critical Reynolds number.

In a stability analysis of plane Poiseuille flow, Orszag (1971) analyzed the linear stability of PPf. He calculated the critical  $Re$  by solving the Orr-Sommerfeld equation numerically using expansions in Chebyshev polynomials. The stability analysis calculated a critical Reynolds number of  $Re = 5,772.22$ . Below this  $Re$ , the laminar base flow can withstand infinitesimally small perturbations and retain the laminar state. However, early experiments showed that the flow becomes turbulent at much lower values of Reynolds number, even at  $Re = 1,000$  (Narayanan & Narayana 1967; Patel & Head 1969).

To detect critical  $Re$ , Patel & Head (1969) carried out skin friction measurements in both pipe and channel flows. They calculated skin friction using the mean flow velocity profile. About the channel flow, it was found to be laminar until  $Re \approx 1,350$ . Afterwards, the transitional state appeared and was found to be in place until  $Re \approx$

2,500-3,000. The fully turbulent state was thought to start with Reynolds numbers greater than  $Re \approx 2,500-3,000$ . For the pipe flow, the transition regime is initiated at  $Re \approx 2,000$  and is terminated at  $Re \approx 3,000$ .

Narayanan & Narayana (1967) along with their experimental investigation of channel flows, obtained the lower range of critical  $Re$  (for large disturbance) theoretically. They stated that the turbulent production and dissipation should be almost equal at the critical  $Re$ . Assuming a logarithmic law for the turbulent velocity profile, they calculated the critical  $Re$  to be 850. At that time, the lower critical  $Re$  obtained from experiments for pipe flow and channel flow was 2,000 (Lindgren 1957) and 1,025, respectively.

Seki & Matsubara (2012) carried out hot-wire anemometry in channel flow at transitional  $Re$  values. They defined lower marginal  $Re$ , the minimum  $Re$  for partial existence of sustainable turbulence, and estimated that to be around 1,400 based on the channel width and the bulk velocity. The upper marginal  $Re$  at which the intermittency factor reaches one is about 2,600. In the study of turbulence, the intermittency factor is defined as the fraction of time the flow remains turbulent at a specific given point of the flow field. The value of the intermittency factor can vary from 0 to 1. In this scaling, a zero value is assigned to a fully laminar region, and the value of one represents a fully turbulent flow. The initial idea of intermittency was proposed by Corrsin (1943).

---

<b>Reference</b>	<b>Flow Geometry</b>	<b>Aspect Ratio</b>	<b>Transition Mechanism</b>	<b>Critical <math>Re</math></b>
Narayanan & Narayana (1967)	Channel	12	Disturbed	1025
Patel & Head (1969)	Channel	48	Natural	1300
Patel & Head (1969)	Pipe	-	Natural	2000
Orszag (1971)	Channel	$\infty$	Natural	5772
Carlson et al. (1982)	Channel	133	Disturbed	1334
Alavyoon et al. (1986)	Channel	166, 277	Disturbed	1200
Avila et al. (2011)	Pipe	-	Disturbed	2040
Seki & Matsubara (2012)	Channel	52	Disturbed	1400
Barkley et al. (2015)	Channel	1	Disturbed	1700
Barkley et al. (2015)	Pipe	-	Disturbed	2000
Sano & Tamai (2016)	Channel	180	Disturbed	904

---

**Table 1 Summary of some notable studies investigating critical  $Re$  in pipe and channel flows.**

## 2.2 Laminar-Turbulent Transition in Non-Newtonian Flows

The transition mechanism to the turbulent regime in non-Newtonian fluids has significant importance due to the various applications of polymeric fluids. Polymer additives have long been considered highly effective drag-reducers. Toms (1948) observed that dissolving a small mass of polymers in a Newtonian solvent may considerably decrease friction drag in a high  $Re$  pipe flow compared to the pure solvent. A large and growing body of literature has investigated the “turbulent drag reduction” phenomenon (Toms 1977; Virk 1975; Virk *et al.* 1997; White & Mungal 2008; Xi 2019). Nevertheless, much uncertainty still exists about the laminar-turbulent transition mechanism in polymeric flows and the transitional state of non-Newtonian flow.

The inaugurating research of Virk (1975) has demonstrated that the laminar-turbulent transition of a dilute polymer solution pipe flow occurs approximately at the same  $Re$  compared to Newtonian solvent. However, both delayed (Castro & Squire 1968; Draad *et al.* 1998; Escudier *et al.* 1998; Giles & Pettit 1967; White & McEligot 1970) and early transition (Forame *et al.* 1972; Hansen & Little 1974; Zakin *et al.* 1977) have been recorded in internal polymeric flow studies. While the transition happens at  $Re \approx 2000$  for pipe flow and  $Re \approx 1000$  for channel flow, it has been reported that transitional  $Re$  can approach values as low as 500 (Hansen & Little 1974;



Hoyt 1977; Ram & Tamir 1964; Zakin *et al.* 1977). The following paragraphs will briefly survey the studies in transitional non-Newtonian shear-thinning fluid flows.

In the 1970s, different researchers noticed an increase in drag force for polymer solutions flow at low  $Re$  compared to the laminar value. In these low  $Re$  regimes, Newtonian fluids cannot sustain turbulence. The term “early turbulence” was commonly used to describe this phenomenon (Forame *et al.* 1972; Zakin *et al.* 1977). This phenomenon is thought to occur when a higher shear rate is obtained because of adequately small pipe diameter (or channel height) and high solvent viscosity. Ram & Tamir (1964) have illustrated that the onset of early turbulence is determined by shear stress rather than  $Re$ . It was also revealed that as molecular weight or concentration increases, the critical  $Re$  for the onset of early turbulence decreases. Nevertheless, the capillary diameter is inversely related to critical  $Re$ . The critical velocity at the onset of turbulence increases linearly with capillary radius. The early transition occurs regardless of inlet disturbances according to (1974). Zakin *et al.* (1977) pressure measurements revealed a smooth transition process to turbulence with reduced drag. No considerable pressure fluctuations were captured in contrast to what happens in Newtonian flows owing to intermittent puffs or slugs. Furthermore, they showed a deviation from the laminar pressure drop profile at  $Re = 1400$ , which is smaller than expected transitional  $Re$  in pipe flows. The onset of early turbulence can be recognized in the absence of pressure rise by the rise in turbulent intensity and the flattening of velocity profile, as these are two critical indicators of turbulence.

While the contradictory results of delayed or early transition could be attributed to the insufficient characterization of the polymer solutions used, theoretical studies have the same contrary conclusions too. On the one hand, calculations with rod-like suspensions predicted a delay in transition (Bark & Tinoco 1978). On the other hand, using the Maxwell model, it was noticed that elasticity in polymer solutions could lower the critical  $Re$  below which no linear growth of disturbances occurs (Porteous & Denn 1972a). These behaviours are respectively linked to the polymer configurations of coiled and stretched polymers. Virk (1975) assorted two distinct types of drag reduction behaviour; Type A for a coiled configuration and type B for a stretched configuration where a delay was observed in transition. Draad *et al.* (1998) carried out detailed experimental research of a pipe flow setup with natural transition  $Re = 60000$  for water. In their setup, fresh polymer solutions with stretched conformation had a natural transition  $Re$  of 8000, and degraded, coiled configuration polymer showed transition at  $Re \approx 30000$ . The reduction in natural transition  $Re$  for polymeric solutions was not apparent. Their observation was attributed to a non-optimal design of the settling chamber contraction or a probable instability of the boundary layer in the entry region due to elastic effects (Porteous & Denn 1972a, 1972b). The friction factor of stretched configuration polymers departed smoothly from the laminar profile, with no distinctive spike visible during the Newtonian transition. The same polymer solution showed a spike in friction factor after being subject to mechanical degradation. Polymers demonstrated a stabilizing effect

concerning artificially triggered transition, and the transition was postponed to a higher  $Re$  than water (Draad *et al.* 1998).

Contrary to Newtonian flows, the  $Re$  is not the only non-dimensional parameter for characterizing the transition of non-Newtonian flows. Weissenberg number is another dimensionless number to consider which compares the elastic forces to the viscous forces, and it can be calculated as follows  $Wi = \lambda\dot{\gamma}$  (in which  $\lambda$  is relaxation time and  $\dot{\gamma}$  is the flow shear rate). As one can point out,  $Wi$  is dependent on the velocity profile of the flow through shear rate. In contrast to  $Wi$ , elasticity number  $E = \lambda v/R^2$  is only dependent on the polymer solution's physical properties and the length scale of internal flow. Therefore, it can be seen that  $Wi$  and  $E$  are both highly dependent on the flow length scale (pipe diameter or channel height).

The early turbulence phenomenon was found mainly in tubes with smaller diameters, but there was little consensus on it in prior studies. Moreover, as mentioned before, the polymer solutions were not precisely characterized in most earlier experiments. Nonetheless, Samanta *et al.* (2013) showed that polymer solutions might undergo early turbulence, and Srinivas & Kumaran (2017) also suggested that rectangle channel flow may go through a similar early transition process. The considerably high polymer concentrations of their solution and the substantially smaller diameter of the tube used by Samanta *et al.* (2013) helped them achieve significantly greater elasticity numbers. Moreover, it allowed them to probe previously unexplored parametric regimes, which is a major difference between their studies and those of others. Indeed, higher elasticity numbers may be responsible for

observing early transition in their study. For example, Draad *et al.* (1998) noticed a drop in the natural transition  $Re$  ( $\approx 40000$ ) with polymer addition but did not observe early turbulence. The recent experiments of Chandra *et al.* (2018, 2020) reported a decrease in the transitional threshold while increasing solution concentration in the range of 300 to 800 parts per million or ppm and substantiated the observations of Samanta *et al.* (2013).

Dubief's group has conducted simulations to examine the existence of elasto-inertial turbulence in high elasticity ( $E$ ) solutions (2013; 2018; 2015). Their results extensively illustrate the possibility of "early turbulence" in polymeric solutions with sufficiently high  $E$ . These observations were in agreement with Samanta *et al.* (2013) experiments. The elasticity number is linked to the polymer solution's longest relaxation time. Due to lower polymer concentrations used for drag reduction studies ( $\approx 50$  ppm), the elasticity number is significantly lower in those experiments than in recent studies that aim to observe "early turbulence.". This fact could be the cause for the absence of early turbulence in drag reduction experiments.

Pan *et al.* (2013) experimentally investigated the instabilities and transition in a long straight microchannel. They disturbed the flow with a number of obstacles at the entrance. Particle image velocimetry was used to capture the velocity profile in addition to dye convection experiments. The result suggested that polymeric fluids in a parallel shear flow can go through a nonlinear subcritical instability at low  $Re$ . However, the  $Re$  scale was too small ( $Re < 0.01$ ) in their experiments because of high solution viscosity and small channel height. They also stated that the critical

Weissenberg number value for the onset of the subcritical instability in the parallel flow is  $Wi = 5.2$  for the disturbance type and level they had in the experiments.

Poole (2016) conducted experiments to study shear-thinning polymer solution flow through both pipe and rectangular channel. The mean velocity profiles at low flow rates appear steady and align with results determined analytically from steady-shear rheology data. At a flow rate higher than the critical flow rate, the mean velocity close to the wall becomes weakly time-dependent, and its magnitude increases with increased flow rate until it reaches saturation. The flow will have a nonmonotonic distribution of velocity gradients, a reduction in wall shear rate, and an overshoot of mean flow velocity close to the duct center because of these fluctuations. As a result of the reduced wall shear rate, the stability leads to a reduction in drag.

In Srinivas & Kumaran's (2017) study, one wall of the channel facility was made from soft material. Although it has been referenced in literature as an example of polymeric channel flow, it is not clear whether the softness of the wall can affect the transition phenomenon or not. The channel height they tested was  $160 \mu\text{m}$ , and it had a laminar turbulence transition at  $Re \approx 290$  for water. They found a concentration threshold below that, in spite of the attenuation of turbulence, the transition  $Re$  remains unchanged. When the polymer concentration increases beyond the threshold, there is a decrease in the transition  $Re$  and the intensity of the turbulent fluctuations. The highest concentration they used reduced the transition Reynolds number to  $Re \approx 115$ .

The flow of viscoelastic fluid in parallel shear geometry at low  $Re$  values is investigated experimentally by Qin and Arratia (2017). They used 300 ppm polyacrylamide solution in a straight duct with 100  $\mu\text{m}$  sides. It was demonstrated that even at low  $Re$ , polymeric fluids flowing in parallel shear geometries could sustain large velocity fluctuations in space and time.

Graham and colleagues (2017) conducted direct numerical simulations on a transitional viscoelastic channel flow. They found a relation between the intermittency of transition of viscoelastic flows and their previously proposed “active and hibernating turbulence” hypothesis (Xi & Graham 2010). When friction Reynolds numbers are increased at a fixed Weissenberg number, the hibernating zones disappear. So the flow is more in the “active” turbulence state; however, these hibernating regions reemerge once viscoelasticity increases and progressively dominate the flow fields at sufficiently high  $Wi$ .

The onset of transition in polymeric flows through microtubes was experimentally studied by Chandra *et al.* (2018). They examined microtube diameters ranging from 390  $\mu\text{m}$  to 470  $\mu\text{m}$  and solution concentrations from 50 to 800 ppm. Due to the small diameter of tubes and high concentration of solutions, the elasticity number  $E$  of their experiments was relatively higher compared to previous studies. Their facility had a natural transition of  $Re \approx 2000$  for the Newtonian case. It was illustrated that increasing polymer concentration first delays the onset of the transition, resulting in a higher transition  $Re$  of 2500. With further increases in polymer concentration, the  $Re$

for transition decreases. The polymer is observed to destabilize the flow at sufficiently high concentrations, and the transition occurs as low as 800.

Choueiri *et al.* (2018) have proposed that the drag reduction resulting from utilizing polymers can go further than the maximum drag reduction (MDR) in a specific domain of parameters. A 10 mm diameter glass pipe was used to test polymer solutions with various concentrations. Newtonian natural transition  $Re$  of their facility was 2800. For concentrations under and equal to 20 ppm, they observed a delay in the onset of turbulence up to  $\sim 25\%$  larger  $Re$ . With increasing  $Re$  to higher values in the low concentration regime, turbulent puffs and slugs were observed. Higher concentrations ( $C \gtrsim 90$  ppm) will lead to elastoinertial instabilities at  $Re$  well below those associated with Newtonian turbulence.

In a recent study, Chandra *et al.* (2020) conducted experiments to study early transition in micro-tubes with diameters of 0.49 to 2.84 mm. They observed a delay in the onset of turbulence for lower concentrations of the added polymer. Still, as the concentration is increased further, the transition  $Re$  drops below 2000, which is transition  $Re$  in Newtonian pipe flows. In small concentrations of polymers, if the  $Re$  is kept above the transition  $Re$  value for Newtonian flows, and the polymer concentration is gradually increased, the flow will relaminarize, and the friction factor will decrease. They also state that the flow undergoes a transition due to elasto-inertial instability as the polymer concentration increases further.

Krishnan *et al.* (2021) utilized velocimetry in a 100 mm diameter pipe to investigate the laminar-turbulent transition of a shear-thinning fluid flow. During

transitions, intermediate structures (puffs and slugs) were observed to form similar to Newtonian transition. The transition occurred in different Reynolds numbers due to their various slurry solutions; however, a delay in transition  $Re$  was recorded in general.



---

<b>Reference</b>	<b>Flow Geometry</b>	<b>Polymer</b>	<b>Concentration (ppm)</b>	<b>Flow Length Scale (mm)</b>	<b>Transition Mechanism</b>	<b>Critical <i>Re</i></b>
Draad <i>et al.</i> (1998)	Pipe	PAMH	20	40	Natural	8000
Samanta <i>et al.</i> (2013)	Pipe	PAM	500	4	Natural	800
Srinivas & Kumaran (2017)	Channel	PAM	50	0.160	Natural	300
Chandra <i>et al.</i> (2018)	Tube	PAM	800	0.390	Natural	800
Chandra <i>et al.</i> (2018)	Tube	PAM	600	0.49	Natural	1080
Chandra <i>et al.</i> (2018)	Tube	PAM	600	2.84	Natural	1462
Chandra <i>et al.</i> (2018)	Tube	PAM	800	0.49	Natural	970

---

**Table 2 Summarizing experimental studies on laminar to turbulent transition of polyacrylamide solutions**

## 2.3 Elasto-Inertial Turbulence

In the '70s, Forame *et al.* (1972) and Zakin *et al.* (1977) made the first observations that polymers cause instability in dilute polymer solutions. These pipe studies observed a friction factor deviation from Poiseuille's law at a Reynolds number below transitional  $Re$  of water.

Samanta *et al.* (2013) had a breakthrough insight into these observations by exploring the flow of polymer solutions in pipes at various concentrations. They observed that for sufficiently high concentrations (500 ppm), the flow goes through a direct transition from a laminar to a chaotic state. This transition even happened at  $Re = 800$ , which is well below the expected transitional  $Re$  for Newtonian pipe flow. This qualitatively distinct chaotic flow regime was named "Elastoinertial turbulence" or EIT. Chandra *et al.* (2018) observations were consistent with Samanta *et al.* (2013) as they first noticed a delay in transition. Increasing concentration led to the transition to EIT at  $Re = 800$ .

There have been more experimental studies of viscoelastic transition in pipes, but Srinivas and Kumaran (2017) showed that the transition state is qualitatively similar in soft-walled microchannels. In their experiments, transition  $Re$  dropped from 300 to 35 for sufficiently high concentrations.

Based on the results described thus far, dilute polymer solutions with sufficient viscoelasticity show robust behaviour in the early transition. The new flow regime following this early transition, referred to as elasto-inertial turbulence (EIT), appears

to display distinct characteristics compared to Newtonian turbulence. The findings point to polymer-driven self-sustaining mechanisms that can support this chaotic flow state with friction factor scalings remarkably close to MDRs (Samanta *et al.* 2013). Nevertheless, EIT remains an active research area as a complete understanding of its mechanisms is still lacking.

Pipe flow experiments by Choueiri *et al.* (2018) provided critical insights into EIT mechanisms. Researchers observed the relaminarization of Newtonian turbulence at low transitional  $Re = 3150$  when polymer concentration was increased in a quasi-static manner. This relaminarization was followed by a “reentrant transition” to EIT marked by “weak, elongated streaks” of flow. The friction factor increased to the MDR limit with this reentrant transition for the chosen parameter set. As a result of these experiments, one can identify two distinct mechanisms of chaos in dilute polymer solutions: Newtonian turbulence, inhibited by viscoelastic flow and elastoinertial turbulence promoted by viscoelasticity. The authors observed a monotonic drop in friction factor at higher transitional  $Re$  (5200 and 10000), which appears to be the more traditional way to convert Newtonian turbulence to MDR. At these higher  $Re$  regimes, the flow state at MDR remained similar to EIT with weak, elongated velocity streaks.

Graham summarized observations and experiments of polymer solutions to illustrate the “parameter space” qualitatively, as shown in Figure 2.3. The elasticity number remains constant on oblique lines shown in the figure. Path A shows studies which keep  $Re$  constant and increase  $Wi$  to explore the parameter space. These studies

demonstrate a direct pathway from Newtonian turbulence, which leads to EIT. Observations made by Choueiri *et al.* (2018) are shown as path B. They kept  $Re$  at 3150 and increased solution concentration, resulting in higher viscoelasticity. Increasing viscoelasticity, they first noticed a relaminarization followed by the transition to EIT. Some polymer drag reduction studies (Escudier *et al.* 2009; Ptasinski *et al.* 2001) report a decrease in velocity fluctuations and Reynolds shear stresses as viscoelasticity increases, which points towards the weakening of near-wall Newtonian turbulent structures. Likewise, as the flow rate increases, we see the switch from Newtonian-style turbulence to MDR/EIT in Path C. According to experimental results by (Forame *et al.* 1972; Samanta *et al.* 2013; Zakin *et al.* 1977), at a sufficiently high elasticity number, a laminar flow can directly go through a transition to a two-dimensional flow with a significantly lower friction factor or better known as EIT, as demonstrated by path D.

Although extensive research has been carried out on polymeric flows, no single experimental study exists that addresses flow states and structures in transition to turbulence. This indicates a need to understand the various perceptions of flow structures that exist among transition. This thesis will investigate the laminar-turbulent transition in non-Newtonian flows.

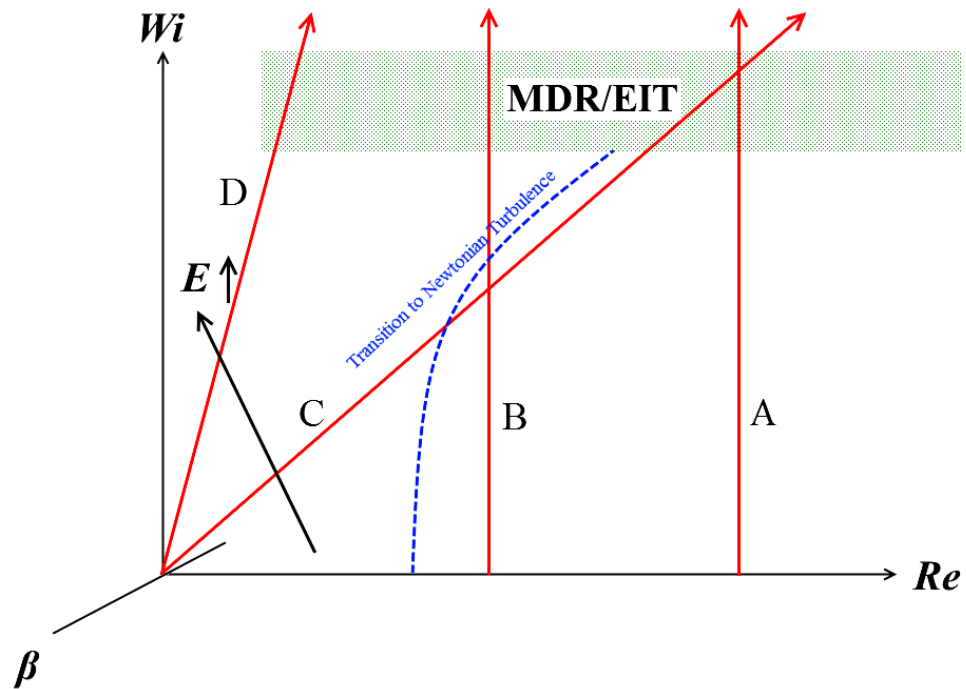


**Figure 2.3** The parameter space of turbulence in dilute polymer solutions. Regenerated figure inspired by (Graham 2014; Shekar 2021; Xi 2019). Boundaries shown here are not necessarily vertical or horizontal, and they might be fuzzy.

### **3. Experimental Methodology**

This thesis encompasses three distinct experimental campaigns, each designed to achieve specific objectives. The first experiment employs two-dimensional time-resolved Particle Image Velocimetry (PIV) in the streamwise-wall-normal plane to investigate the transitional behaviour of water and polymeric flows across a wide range of  $Re$ . The second experiment focuses on collecting long-duration data sequences using double-frame data acquisition to explore the statistical properties of transitional flows. In the third experiment, the streamwise-spanwise plane is examined to study turbulent spots. The outcomes of these experiments for water flow are compared with prior experimental findings and numerical studies to assess the accuracy of the measurements.

The methodology employed in these experiments is detailed in five sections. The first section provides an overview of the flow loop utilized in the experiments. The second and third sections delve into the preparation of the polymer solution and the rheological measurements, respectively. The fourth section outlines the streamwise-

wall-normal plane PIV setup and the image processing procedure employed. Lastly, the fifth section describes the streamwise-spanwise plane PIV setup and the corresponding image processing procedure.

### **3.1 Flow Facility**

This section delineates the gravity-driven closed-flow loop apparatus employed for conducting the experiments. A schematic representation of the flow facility can be found in Figure 3.1. The apparatus comprises an elevated reservoir, a settling chamber, a test section, a diffuser, and a downstream tank. As shown in Figure 3.1 the  $x$ ,  $y$ , and  $z$  axes are in the streamwise, wall-normal and spanwise directions, respectively, and the coordinate system is placed on the channel centerline.

The upstream reservoir, situated 2.6 meters above the test section centerline, has a capacity of 190 litres. The pressure head generated by this elevated reservoir propels the flow within the loop. A 254 mm pipe connects the upstream reservoir to the settling chamber. The settling chamber spans approximately 2 meters in length and features two designated slots for installing honeycombs and meshes. Two layers of honeycombs coupled with mesh layers are installed at distances of 155 mm and 1655 mm from the settling chamber entrance, as well as 3685 mm and 2185 mm upstream of the measurement location. The maximum cross-section of the settling chamber measures  $596 \times 254$  mm.

Connected to the end of the settling chamber is a nozzle with a length of 0.75 meters and a contraction ratio of 48:1, designed to minimize turbulence and non-

uniformity in the test section. The test section, fabricated from acrylic, has dimensions of full height ( $H$ ) 16 mm, half height ( $h$ ) 8 mm, width ( $W$ ) 200 mm, and length ( $L$ ) 2390 mm. This results in an aspect ratio of  $W/H = 12.5$  and a length-to-height ratio of  $L/H = 149$ . The inlet section and connections between all channel components are meticulously designed and constructed to be as smooth as possible, thereby reducing upstream perturbations. The flow rates achieved during the experiments ranged from a minimum of 0.1 l.s<sup>-1</sup> to a maximum of 2.5 l.s<sup>-1</sup>.



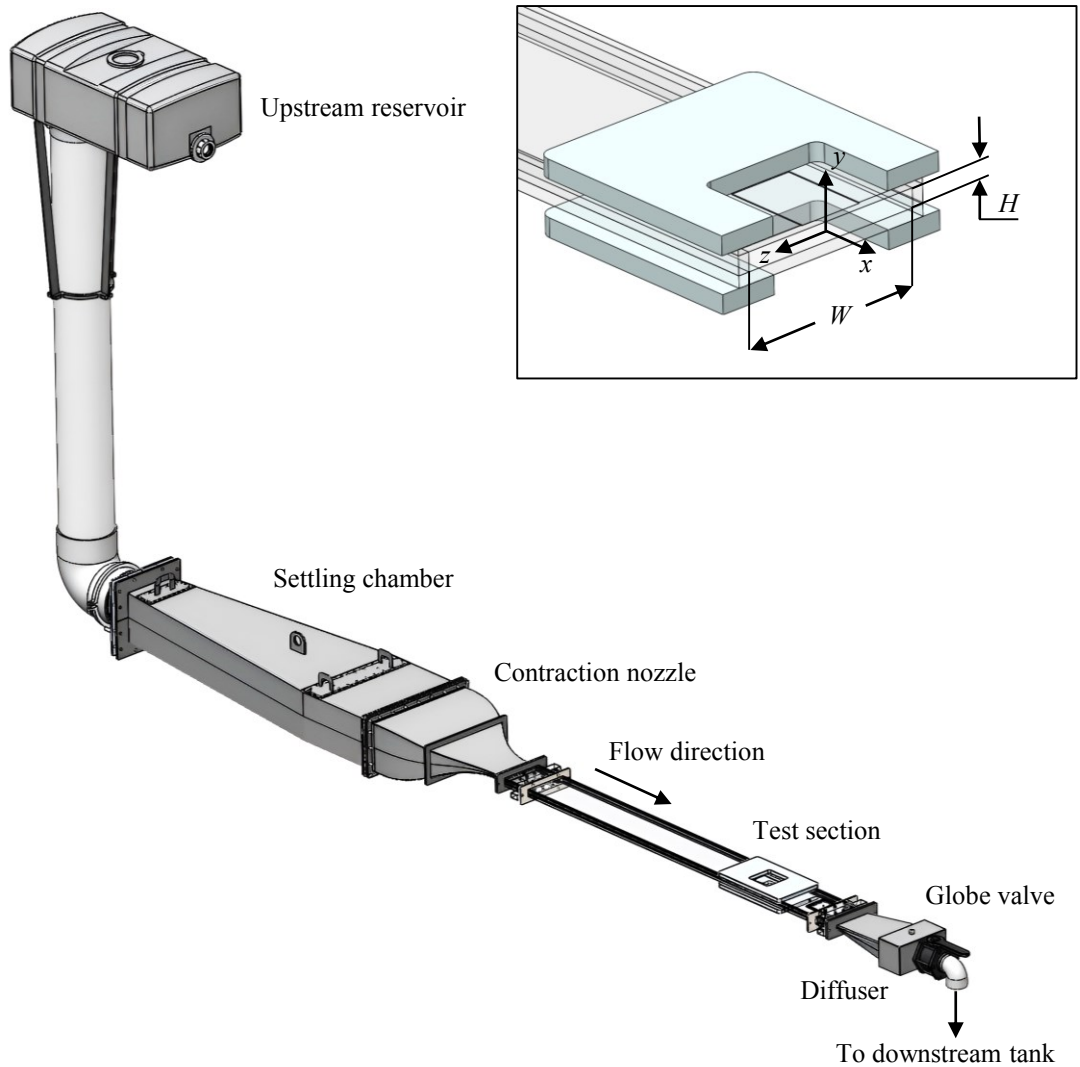


**Figure 3.1 Annotated schematic view of the experimental facility. The inset shows the cross-section of the test section and the coordinate system.**

After passing through the test section, the flow enters a diffuser and is subsequently directed into a downstream tank with a capacity of 760 litres. To maintain consistency, the upstream reservoir is filled to the same level before each experiment. The upstream reservoir can be refilled using a progressing cavity pump (Moyno 36704)

connected to a 1.5 kW motor from the downstream tank to the upstream reservoir placed at the ceiling. The pump's maximum rotational speed is 1755 rpm, regulated by a variable frequency drive (VFD). The acquired signal from the PMC VersaLine® VL3000 level transmitter was fed to National Instruments LabVIEW software, and an output signal was sent to VFD to control the pump and ensure the upstream reservoir was filled to the same level before each experiment. To initiate every experiment, the desired fluid stored in the downstream tank was used to fill the facility.

The loop operating procedure can be described in detail through the following steps:

1. Initiation of the experiment: To begin each experiment, the fluid of choice, which is stored in the downstream tank, is used to fill the facility. This ensures that the desired fluid is readily available for the experiment.
2. Flow rate control: In order to regulate the flow rate of the fluid, a high-precision globe valve is employed. This valve can be adjusted to specific openings, allowing for precise control over the flow rates required for each experiment.
3. Measurement completion: Once the necessary measurements have been taken, the fluid flow is stopped by closing the high-precision globe valve. This ensures that the fluid flow is halted at the appropriate time, allowing for accurate data collection.
4. Refilling the ceiling reservoir: After the fluid flow has been stopped, a feedback control system is utilized to refill the ceiling reservoir to a constant

level. This is done to maintain consistent experimental conditions for each trial, ensuring that the results are reliable and reproducible.

For each solution, at least eight valve openings were tested ranging from laminar flow conditions to turbulent, with each opening being repeated at least five times to ensure accuracy and consistency. Furthermore, to investigate the transitional state, an additional six repetitions of measurements were conducted for the valve openings in the transitional flow rate. The valve openings tested for each solution are shown in Table 3. These rigorous testing procedures were employed to ensure the repeatability and statistical convergence of the experimental results. The change in fluid pressure head was less than 10% when compared to the initial state before the experiment and after its termination, even at the maximum flow rate of 2.5 l/s. Furthermore, examining the flow rate during the data acquisition process revealed that any variations were negligible. Then a feedback control system was used to fill up the ceiling reservoir to a constant level each time with the pump rotation speed being limited to 440 rpm.

<b>Water</b>	<b>50 ppm</b>	<b>75 ppm</b>	<b>100 ppm</b>	<b>150 ppm</b>
1/8	1/4	1/2	3/4	3/4
1/4	1/2	3/4	1	1
1/2	3/4	1	1 1/4	1 1/4
3/4	1	1 1/4	1 1/2	1 1/2
1	1 1/4	1 1/2	2	2
1 1/4	1 1/2	2	2 1/2	2 1/2
1 1/2	2	3	3	3
×	×	5	4	4
×	×	8 1/2	5	5
×	×	×	6	6
×	×	×	7	7
×	×	×	×	10

**Table 3 Valve Openings Tested for Each Solution. The valve openings are presented in units of turns of the valve opening. A 1” globe valve was used for the 50 ppm and 75 ppm solutions. A 1 1/2” globe valve was used for the 100 ppm and 150 ppm solutions.**

### 3.2 Polymer solution preparation

The chosen drag-reducing additive for these experiments is a flexible polymer, polyacrylamide (PAM) (SNF Floerger, 6030S), which has a molecular weight of 30-35 MDa. The chemical structure of PAM is shown in Figure 3.2. Four concentrations of PAM were considered for the study: 50, 75, 100, and 150 parts per million (ppm).

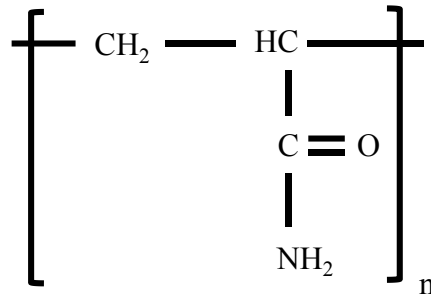


**Figure 3.2 shows the molecular structure of polyacrylamide (PAM), the drag-reducing polymer used in the experiments.**

The preparation process begins with accurately weighing the solid polymer powder using an Ohaus E11140 Explorer digital scale, which offers a resolution of 0.1 mg. The weighed powder is then gradually added to 170 litres of tap water in a cylindrical tank, ensuring a slow and controlled dispersion to prevent the formation of clumps or aggregates. This mixture forms a concentrated master solution.

To facilitate thorough mixing and dispersion of the polymer, a mixer (LIGHTNIN LabMaster L5U10F) equipped with a three-blade marine impeller with a 75 mm diameter is employed. The mixer agitates the master solution at a speed of 75 rpm for

two hours, promoting the formation of a homogeneous solution and minimizing the risk of mechanical degradation.

Once the initial mixing is complete, the master solution is drained into the downstream tank and diluted to the desired concentration using additional tap water. The pump is then used to circulate and gently mix the 720-litre PAM solution within the downstream tank for another two hours at a rotational speed of 225 rpm. This secondary mixing step ensures that the diluted polymer solution is uniform and free of any concentration gradients.

After completing the mixing process, the resulting solution is left to rest for 15 hours overnight. This resting period allows any residual air bubbles, impurities, or undissolved polymer particles to dissipate or settle, further enhancing the homogeneity and quality of the prepared polymer solution.

On the following day, the pump, operating at a rotational speed of 225 rpm, is utilized to fill the upstream reservoir with the PAM solution. This step ensures that the experimental setup is primed and ready for conducting the tests with the carefully prepared polymer solution. The meticulous preparation process described in this section is crucial for obtaining reliable and consistent results in the subsequent experiments involving drag reduction and flow dynamics.

## 3.3 Rheology measurements

### 3.3.1 Shear viscosity measurements

Viscosity is a critical parameter in investigating polymer drag reduction, and its impact on the rheological properties of the fluid cannot be overstated. It is well-known that the addition of a specific amount of polymer to a Newtonian fluid can transform it into a non-Newtonian fluid. Thus, in this study, we will be examining the shear viscosity or apparent viscosity. The rheological characterization of polymer solutions will be conducted using a torsional rheometer (HR-2, TA Instruments) equipped with a cone and plate geometry.

To accurately characterize rheology, it is necessary to measure viscosity at various shear rates for non-Newtonian fluids. A depiction of the cone and plate geometry of the rheometer is presented in Figure 3.3. The rheometer comprises a cone affixed to a rotor and a stationary plate. While the plate remains stationary, the cone is driven by a motor. The geometry used had a radius of  $R = 30$  mm and an angle of  $\beta = 2^\circ$ . Additionally, a temperature control system is attached to the rheometer to maintain the desired temperature.

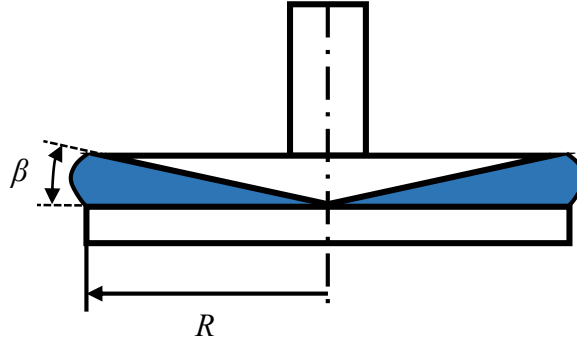


**Figure 3.3 illustrates a schematic diagram of the cone and plate rheometer used to measure the shear viscosity of the test solutions.**

Viscosity measurements were taken at a constant temperature of 25°C and a shear rate of up to 200 s<sup>-1</sup>. For Newtonian fluids, viscosity is shear rate independent. However, with the introduction of polymers to solutions and increasing their concentration, a considerable increase in solution viscosity occurs, leading to non-Newtonian behaviour. Specifically, polymer solutions exhibited shear-thinning behaviour, meaning that viscosity decreases as the shear rate increases. This behaviour is more pronounced at higher polymer concentrations, as expected.

Figure 3.4 shows the shear viscosity  $\mu$  of solutions with increasing shear rates  $\dot{\gamma}$ . All PAM solutions demonstrate noticeable shear-thinning but to varying degrees. Here, shear-thinning is well described by the power-law model of (3.1), which was fit on measurements of  $\mu$  as a function of  $\dot{\gamma}$ .

$$\mu = K \dot{\gamma}^{n-1}, \quad (3.1)$$

the model parameters are presented in Table 4. Note that the rate-index  $n$  describes the slope in  $\mu$  with increasing  $\dot{\gamma}$  and the degree of shear-thinning – as  $n$  decreases the



solution becomes more shear-thinning. Error bars show the standard deviation of five samples taken from the channel flow facility, each of which corresponds to a set of various valve openings tested with the same solution.

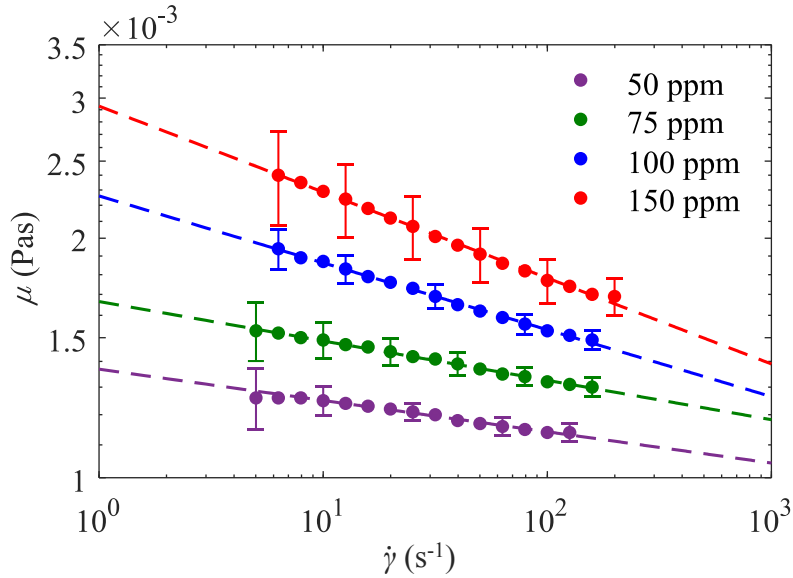


**Figure 3.4 The relationship between shear rate and apparent viscosity is demonstrated for four polymer solutions, highlighting the fluids' rheological behaviour.**

### 3.3.2 Extensional rheology measurements

A bespoke dripping-onto-substrate (DoS) apparatus was utilized to evaluate the extensional rheological properties of PAM solutions. In the employed method for measuring, a minuscule droplet was released from a flat-tipped nozzle featuring a diameter ( $D_0$ ) of 1.27 mm. A syringe pump (Legacy 200, KD Scientific Inc.) facilitated the expulsion of the droplet at a rate of  $0.02 \text{ ml min}^{-1}$ . The pumping process

ceased when the droplet came into contact with a glass substrate positioned 3D0 or 3.81 mm beneath the flat-tipped nozzle outlet. Upon contact with the substrate, a liquid bridge formed between the nozzle outlet and the substrate. The liquid bridge's diameter ( $D_{min}$ ) experienced a rapid reduction due to capillary forces. A schematic of the DoS setup is illustrated in Figure 3.5.

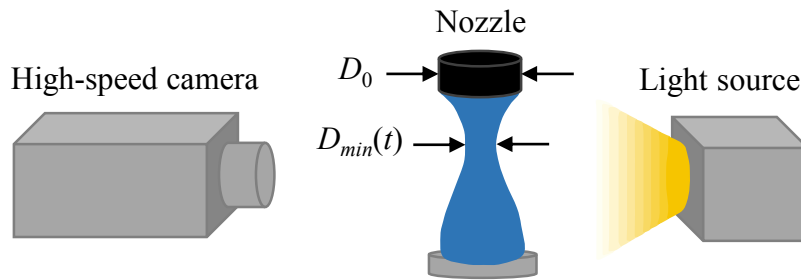


**Figure 3.5 shows a schematic representation of the dripping-onto-substrate (DoS) experimental setup which was employed to evaluate the extensional rheological properties of the polymer solutions..**

A high-speed camera (v611, Vision Research) and LED backlighting were utilized to capture images of the liquid bridge. The camera was equipped with a  $1280 \times 800$  pixel complementary metal-oxide semiconductor sensor, with pixel dimensions of  $20 \times 20 \mu\text{m}^2$  and a 12-bit depth. A zoom lens provided a magnification of 3.8 and a scale of  $5.16 \mu\text{m pixel}^{-1}$ . Images were acquired at a rate of 2 kHz. The liquid bridge's minimum diameter ( $D_{min}$ ) was ascertained using a MATLAB (MathWorks Inc.) script.

The Ohnesorge number,  $Oh = t_v/t_R$ , establishes a connection between the time scale linked to viscous forces and the Rayleigh time  $t_R$ , which is associated with surface tension and inertial forces. In this case,  $t_v = \eta D_0/2\sigma$  represents the characteristic time

scale for visco-capillary thinning,  $t_R = (\rho D_0^3 / 8\sigma)^{1/2}$ , and  $\sigma$  denotes the surface tension. When  $Oh > 1$ , viscous forces play a significant role, and the evolution of  $D_{min}$  is characterized by visco-capillary thinning,  $D_{min}(t)/D_0 = 0.0709(t_b - t)/t_v$ . For elastic fluids, the Deborah number,  $De = t_e/t_R$ , indicates the proportion between the extensional relaxation time  $t_e$  and the Rayleigh time. If  $De > 1$ , the necking process is primarily influenced by elastic and capillary forces. This elastocapillary (EC) regime is represented by:

$$\frac{D_{min}(t)}{D_0} = A \exp\left(-\frac{t}{t_e}\right), \quad (3.2)$$

where  $A$  is a constant. Figure 3.6 illustrates the impact of polymer concentration on filament diameter over time, with zero time signifying the moment the droplet is released. Error bars are determined by calculating the standard deviation of five repeated measurements, each performed on samples obtained prior to flow measurements in the channel flow facility. A noticeable increase in resistance to capillary force is observed at 75 ppm compared to 50 ppm. It is evident that dilute polymer solutions experience a faster filament breakup than concentrated polymer solutions, which can be attributed to the lower elasticity in dilute polymer solutions. Polymer solutions with higher relaxation times exhibit greater elasticity (Marshall & Metzner 1967). Delshad *et al.* (2008) also employed relaxation time to represent elasticity in polymers within a viscoelastic model. Furthermore, it is apparent that the solution's resistance to capillary force escalates with increasing polymer

concentration. Consequently, concentrated polymer solutions possess a higher stretching potential compared to dilute polymer solutions.

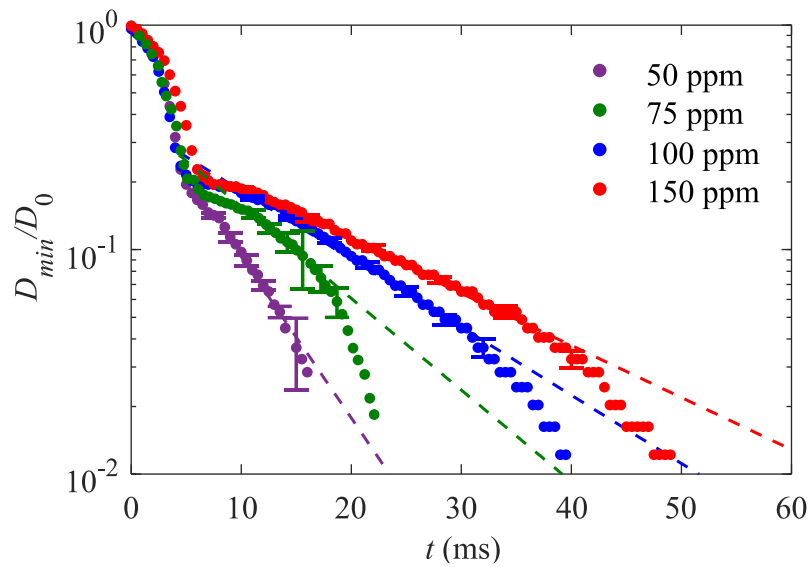


**Figure 3.6 Semi-logarithmic plot of filament diameter as a function of time for four distinct polymer concentrations.**

---

<b>Concentration (ppm)</b>	<b><math>K</math> (Pa s<sup>n</sup>)</b>	<b><math>n</math></b>	<b><math>t_e</math> (ms)</b>
50	$1.37 \times 10^{-3}$	0.961	2.0
75	$1.67 \times 10^{-3}$	0.951	3.5
100	$2.26 \times 10^{-3}$	0.916	4.7
150	$2.93 \times 10^{-3}$	0.892	6.1

---

**Table 4 Parameters used in equation 1 for each PAM solution are shown. Additionally, the relaxation times calculated from DoS measurements are also displayed.**

---

### 3.4 Particle image velocimetry (PIV)

Three separate test campaigns have been conducted in this study: double-frame data collection with extended acquisition times in the streamwise-wall-normal plane, time-resolved data collection in the streamwise-wall-normal plane, and double-frame data collection with extended acquisition times in the streamwise-spanwise plane. The double-frame data collection with extended acquisition times, hereafter referred to as long-duration, involves collecting a large number of image pairs at a lower sampling rate to capture the evolution of flow structures over long time periods. In contrast, the time-resolved data collection refers to acquiring single-frame images at higher sampling rates to provide better temporal resolution of the flow field. However, the maximum duration of time-resolved measurements is limited by the memory of the high-speed camera. Particle image velocimetry (PIV) was used to measure the velocity of the fluid within the test section. The PIV system consisted of a high-speed camera (v611, Phantom) and a dual-cavity Nd:YLF high-repetition laser (DM20-527 Photonics Industries). The high-speed camera has a 1280×800 pixel complementary metal oxide semiconductor (CMOS) sensor with a pixel size of  $20 \times 20 \mu\text{m}^2$  and a resolution of 12 bits. The laser beam has a wavelength of 532 nm, and maximum pulse energy of  $20 \text{ mJ pulse}^{-1}$ . A programmable timing unit (PTU X, LaVision GmbH) synchronized the camera and laser. The flow was seeded with  $2 \mu\text{m}$  diameter silver-coated solid glass spheres (Potters Industries Conduct-O-Fil® SG02S40). PIV measurements were taken along two fields of view (FOV). The first being along the

streamwise-wall-normal plane, and another along the streamwise-spanwise plane. The PIV configuration is described for each test campaign in this section.

### 3.4.1 Long-duration wall-normal PIV

In this test campaign the goal was to collect long data sequences of streamwise wall-normal velocity fields of the transitional Reynolds number range for each solution. A plano-convex spherical lens with a focal length of  $f = +200$  mm and a cylindrical lens with a focal length of  $f = -20$  mm were used were utilized to form a laser sheet with a thickness of 1 mm and a width of 160 mm in the  $x$  direction for streamwise-wall-normal measurements. The camera was equipped with a Sigma lens that had an  $f/11$  aperture and a focal length of  $f = 105$  mm. The sensor resolution was decreased to  $1280 \times 312$  to allow for longer data acquisition times and recording rates when necessary.

This test campaign involved the acquisition of double-frame images at a rate of 60 Hz. The temporal delay between the two laser pulses utilized for double-frame measurements was varied from 700 to 6900  $\mu\text{s}$  and was set accordingly for each flow rate. The desired particle shift was 8 to 12 pixels. Each dataset comprised 13,569 double-frame images. This measurement scheme facilitated extended data collection periods of This measurement scheme permitted long data collection times ranging from approximately  $500T$  to  $2700T$  corresponding to the lowest and highest  $Re$  respectively, where  $T = H/\langle U_c \rangle$  is a representative time scale of the flow.

The velocity vectors for each measurement were calculated using DaVis 8.4 software from LaVision GmbH. The first step involved subtracting the minimum

image intensity from each dataset. Subsequently, the intensity of each image was normalized by the average intensity of the entire image ensemble. Velocity vectors were computed using cross-correlation with a final interrogation window size of  $32 \times 32$  pixels ( $0.45 \times 0.45$  mm) and an overlap of 75% between adjacent interrogation windows.

### **3.4.2 Time-resolved wall-normal PIV**

The objective of this experimental campaign was to enhance the temporal resolution of flow-field measurements. Additionally, the investigation encompassed the evaluation of both higher and lower Reynolds numbers to ensure the accuracy of the transitional Reynolds number range that was obtained.

Similar to long duration wall-normal setup, a combination of lenses was used to shape the laser beam into a laser sheet with 1 mm thickness and 160 mm width in the  $x$  direction. A Sigma lens with a focal length of  $f = 105$  mm and an aperture of  $f/11$  was connected to the camera. Sensor resolution was reduced to  $1280 \times 312$  to achieve the maximum duration of data recording.

In order to acquire time-resolved data, single-frame images were obtained at acquisition rates ranging from 0.2 to 9 kHz. Like the double-frame measurements, the single-frame datasets also consisted of 13,569 images. However, due to the higher acquisition rates, the duration of the single-frame datasets was much shorter. As previously mentioned, eight valve openings were tested ranging from laminar flow conditions to turbulent utilizing the single frame, time-resolved measurement scheme.



The additional six repetitions of valve openings with transitional flow rates were investigated using long-duration double-frame acquisition.

The velocity vectors were calculated using DaVis 8.4 software from LaVision GmbH. The image pre-processing steps were similar to long-duration double frame acquisition. Then the velocity vectors were computed using a sliding ensemble correlation with a final interrogation window size of  $32 \times 32$  pixels ( $0.55 \times 0.55$  mm) and an overlap of 75% between adjacent interrogation windows. Three correlation maps were averaged over a time period that, based on the acquisition rate, ranged from  $6.5 \times 10^{-4}$  to 0.01 seconds in the flow.

### **3.4.3 Long-duration spanwise PIV**

In order to observe turbulent spots from the streamwise spanwise field of view, long-duration double frame data acquisition was conducted for transitional Reynolds numbers of all solutions.

The laser sheet was positioned in the  $xz$  plane at a distance of  $y = 0$  from the wall in measurements taken in the streamwise-spanwise plane. The thickness of the laser sheet was around 1.5 mm and its width in the  $x$  direction was about 70 mm. A camera lens from Nikon with a focal length of  $f = 60$  mm and an aperture of  $f/5.6$  was used. The sensor resolution for experiments in the  $x$  and  $z$  directions was set to  $1280 \times 600$ .

Double-frame images were collected at a rate of 60 Hz. The image pre-processing procedure was the same as long-duration wall-normal measurements. Velocity vectors for the streamwise-spanwise field of view had a final IW size of  $48 \times 48$  pixels ( $1.87 \times 1.87$  mm).

The velocity vectors in the  $x$ ,  $y$  and  $z$  directions are denoted by  $U$ ,  $V$  and  $W$ , respectively. The symbol  $\langle \dots \rangle$  represents time averaging. The  $x$  component of the velocity vector at the centerline of the channel ( $y = 0$ ) is denoted by  $U_c$ , while the streamwise velocity fluctuations are represented by  $u$ , which is calculated using the relationship  $u = U - \langle U \rangle$ . In order to obtain the wall shear rate  $\dot{\gamma}_w$  for laminar cases, a parabolic function was fitted to the  $\langle U \rangle$  versus  $y$  data, and the slope of the parabola at both wall locations was calculated and then averaged to determine  $\dot{\gamma}_w$ . For transitional and turbulent cases, a linear fit was applied to the  $\langle U \rangle$  versus  $y$  data in the near-wall region of  $y^+ \leq 5$  of both walls, and then to obtain  $\dot{\gamma}_w$ . With the wall shear rate determined, fluid viscosity at the wall shear rate ( $\mu_w$ ) was calculated for each test case using equation (1). The Reynolds number was then calculated as  $Re = \rho U_B H / \mu_w$ , where  $U_B$  is the bulk velocity and  $\rho$  is the fluid density. The wall shear stress ( $\tau_w$ ) was computed following  $\tau_w = \mu_w \dot{\gamma}_w$ , and this value was used to calculate the skin friction coefficient,  $C_f = 2\tau_w / (\rho U_B^2)$ . In the following sections, the superscript + denotes inner normalization, where velocity is normalized by the friction velocity  $u_\tau = (\tau_w / \rho)^{1/2}$ , and distance  $y$  is normalized by wall units  $\lambda = \mu_w / \rho u_\tau$ . For turbulent flows, the friction Reynolds number is defined as,  $Re_\tau = \rho u_\tau h / \mu_w$ .

### 3.5 Laminar/Turbulent Detection

The process of distinguishing between laminar and turbulent patches within transitional flow fields relied on the analysis of fluctuations in the centerline velocity, denoted as  $U_c$ . In order to eliminate the influence of high-amplitude, low-frequency

fluctuations that were present in visually laminar sections of the flow, a high-pass filter was initially applied to  $U_c$ . The cut-off frequency for this filter was set at  $f_c = 0.05/T$ . The outcome of this filtering process was a new filtered centerline velocity, referred to as  $u_f$ .

Subsequent to the filtering step, both a moving average and a moving standard deviation were calculated for  $u_f$ . This was achieved by employing a moving window with a length of  $20T$ , which allowed for a more detailed examination of the flow characteristics. In order to determine the nature of the flow within each moving window, a detection parameter  $I$  was introduced. This parameter was computed by taking the ratio between the standard deviation and the average value of  $u_f$  within each window.

The classification of flow as either turbulent or laminar was based on the value of the detection parameter  $I$ . Instances where  $I$  exceeded 0.02 were deemed turbulent, while those with lower values were considered laminar. It is important to note that any turbulent or laminar regions with a duration shorter than  $20T$  were disregarded in this analysis, as they were deemed insufficiently representative.

Once the turbulent and laminar regions were identified, further analysis was conducted to quantify the turbulence characteristics. The turbulence fraction ( $F_T$ ) was calculated by dividing the total duration of the turbulent flow by the overall acquisition time, providing insight into the prevalence of turbulence within the flow. In addition, the turbulence intensity (TI) for each region was determined by

calculating the ratio of the standard deviation ( $\sigma$ ) of the filtered velocity fluctuations to the mean velocity,

$$TI = \sigma / \langle U_c \rangle. \quad (3.3)$$

Figure 3.7 presents an example of the transitional water flow at  $Re = 2000$ , along with the application of the laminar/turbulent detection algorithm. The horizontal axis displays time, normalized by the representative time scale of the flow, denoted as  $t' = t/T$ . In Figure 3.7(a), the contour of streamwise velocity is depicted in relation to  $t'$ , revealing alternating regions of turbulent patches and laminar flow. The extraction of the channel centerline velocity yields the signal displayed in Figure 3.7(b). Upon calculating the velocity fluctuations and applying the high-pass filter, the resulting signal,  $u_f$ , is illustrated in Figure 3.7(c). The high-pass filter effectively eliminates the low-frequency variations in  $U_c$  observed in visually laminar sections of the flow, specifically between  $t'$  values of 220 and 550 in Figure 3.7(a) and (b).

The detection parameter  $I$  is subsequently plotted in Figure 3.7(d). Laminar flow regions, characterized by  $I < 0.02$ , are represented by blue lines in the  $U_c$ ,  $u_f$ , and  $I$  plots in Figure 3.7(b) through (d), while turbulent areas ( $I > 0.02$ ) are indicated by red lines. A visual comparison of Figure 3.7(a) with the subsequent subplots demonstrates the detection algorithm's effectiveness in identifying the four turbulent patches present within the transitional water flow.

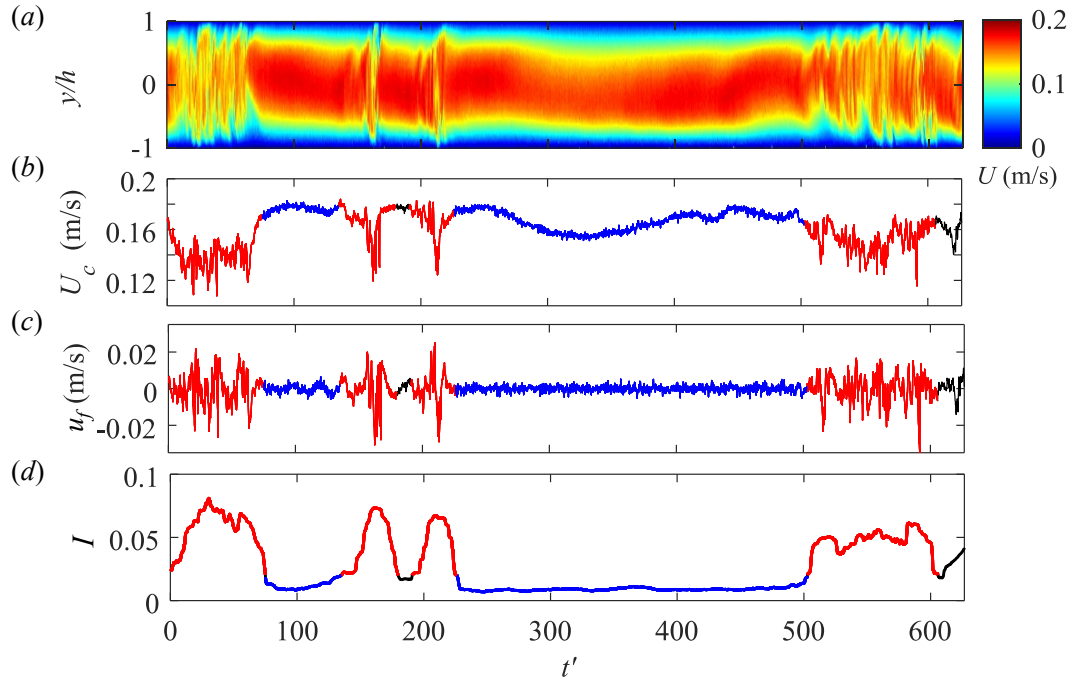


**Figure 3.7 Laminar/turbulent identification technique of water flow. (a) a flow visualization contour, (b) the extracted centerline velocity signal, (c) filtered velocity fluctuations, (d) the detection parameter  $I$ . Turbulent regions are shown in red, laminar regions in blue, and short-length instances that are disregarded are in black.**

### 3.6 Uncertainty Analysis

In this section, we will discuss the sources of uncertainty in our experiments. Uncertainties in particle image velocimetry measurements, shear viscosity measurements, and calculated parameters such as Reynolds number, friction factor, and inner-scaled velocity profiles are considered and presented. Understanding and quantifying these uncertainties is crucial for the accurate interpretation of our results and the reliability of our conclusions.

A frequently used approximation for the uncertainty linked to an individual PIV measurement is a displacement of 0.1 pixels. Sciacchitano (2019) argues that this "all-encompassing constant" for PIV uncertainty might be an oversimplification, as the uncertainty is largely influenced by the specific features of each experiment. Nevertheless, studies focused on assessing PIV uncertainty often report uncertainties close to 0.1 pixels (Raffel *et al.* 2018), which is why this value has been adopted in this work to represent the error associated with the PIV processing algorithm.

Shear viscosity measurements were conducted individually for each solution. Temperature variations have the potential to influence viscosity values; therefore, we carried out viscosity measurements at the same temperature as the experiments to minimize this impact. Inhomogeneities in the polymeric solutions or the presence of air bubbles may lead to errors in the viscosity measurements. To mitigate these effects, we ensured thorough sample preparation and degassing. Furthermore, each concentration was prepared and tested nine times. The standard deviation of these repetitions is presented in Figure 3.4.

The calculated parameters, such as Reynolds number, friction factor, and inner scaled velocity profiles, are derived from the PIV, shear viscosity measurements, and wall location. Wall location affects these parameters because it determines the boundary conditions for the fluid flow, which in turn influences the velocity gradients and shear stresses near the wall. As a result, the uncertainties in wall location measurements can impact the accuracy of the calculated parameters. Therefore, the uncertainties in these measurements propagate to the calculated parameters. Standard

error propagation techniques were used to estimate the uncertainties in these parameters.

As mentioned before, Reynolds number was calculated as  $Re = \rho U_B H / \mu_w$ . Then the uncertainty in the Reynolds number ( $\Delta Re$ ) can be calculated using the formula for uncertainty propagation considering the uncertainty in fluid density is negligible,

$$\Delta Re = \sqrt{\left(\frac{\partial Re}{\partial U_B} \Delta U_B\right)^2 + \left(\frac{\partial Re}{\partial H} \Delta H\right)^2 + \left(\frac{\partial Re}{\partial \mu_w} \Delta \mu_w\right)^2}, \quad (3.4)$$

where  $\frac{\partial Re}{\partial U_B} = \frac{\rho H}{\mu_w}$ ,  $\frac{\partial Re}{\partial H} = \frac{\rho U_B}{\mu_w}$ , and  $\frac{\partial Re}{\partial \mu_w} = -\frac{\rho U_B H}{\mu_w^2}$  are the partial derivatives of the Reynolds number with respect to independent variables and evaluated at the nominal values of the variables. In this context, the uncertainty associated with the channel height can be considered negligible. To calculate the relative uncertainty of the Reynolds number ( $\Delta Re/Re$ ), the following formula is derived from equation (3.4),

$$\frac{\Delta Re}{Re} = \sqrt{\left(\frac{\Delta U_B}{U_B}\right)^2 + \left(\frac{\Delta \mu_w}{\mu_w}\right)^2}. \quad (3.5)$$

Furthermore, as previously mentioned, the skin friction coefficient was determined using the formula  $C_f = 2\tau_w/(\rho U_B^2)$ . Employing a similar approach and assuming the uncertainty in fluid density to be negligible, the propagated error in the skin friction coefficient can be calculated as follows:

$$\Delta C_f = \sqrt{\left(\frac{\partial C_f}{\partial \tau_w} \Delta \tau_w\right)^2 + \left(\frac{\partial C_f}{\partial U_B} \Delta U_B\right)^2}, \quad (3.6)$$

the relative uncertainty in skin friction factor ( $\Delta C_f/C_f$ ) is calculated using the following formula,

$$\frac{\Delta C_f}{C_f} = \sqrt{\left(\frac{\Delta \tau_w}{\tau_w}\right)^2 + \left(2 \frac{\Delta U_B}{U_B}\right)^2}. \quad (3.7)$$

Since the wall shear stress is obtained as  $\tau_w = \mu_w \dot{\gamma}_w$  and  $\dot{\gamma}_w = \frac{du}{dy}$  at the wall location, the uncertainty in wall shear stress ( $\Delta \tau_w$ ) is calculated as,

$$\Delta \tau_w = \sqrt{\left(\frac{\partial \tau_w}{\partial y} \Delta y\right)^2 + \left(\frac{\partial \tau_w}{\partial \mu_w} \Delta \mu_w\right)^2}, \quad (3.8)$$

considering the partial derivatives to be derived as follows,

$$\frac{\partial}{\partial y} (\tau_w) = \mu_w \frac{\partial}{\partial y} \left(\frac{du}{dy}\right), \quad (3.9a)$$

$$\frac{\partial}{\partial u} (\tau_w) = \frac{\partial}{\partial u} \left(\mu_w \frac{du}{dy}\right) = \frac{\partial}{\partial u} \left(\frac{du}{dy}\right) \mu_w = 0, \quad (3.9b)$$

$$\frac{\partial}{\partial \mu_w} (\tau_w) = \frac{du}{dy}, \quad (3.9c)$$

the relative uncertainty in wall shear stress ( $\Delta \tau_w / \tau_w$ ) could be derived as

$$\frac{\Delta \tau_w}{\tau_w} = \sqrt{\left(\frac{\Delta y}{y}\right)^2 + \left(\frac{\Delta \mu_w}{\mu_w}\right)^2}. \quad (3.10)$$

For inner scaled velocity ( $u^+$ ), the error propagation will result in the following uncertainty formula:

$$\Delta u^+ = \sqrt{\left(\frac{\partial u^+}{\partial u} \Delta u\right)^2 + \left(\frac{\partial u^+}{\partial u_\tau} \Delta u_\tau\right)^2}, \quad (3.11)$$

and the relative uncertainty in inner scaled velocity ( $\Delta u^+ / u^+$ ) will be calculated as

$$\frac{\Delta u^+}{u^+} = \sqrt{\left(\frac{\Delta u}{u}\right)^2 + \left(\frac{\Delta u_\tau}{u_\tau}\right)^2}, \quad (3.12)$$

where relative uncertainty in friction velocity ( $\Delta u_\tau / u_\tau$ ) is calculated as follows:



$$\frac{\Delta u_\tau}{u_\tau} = 1/2 \sqrt{\left(\frac{\Delta \tau_w}{\tau_w}\right)^2 + \left(\frac{\Delta \rho}{\rho}\right)^2}, \quad (3.13)$$

and the uncertainty in solution density is deemed negligible.

The total relative uncertainty for the independent variables is presented in Table 5, while Table 6 displays the calculated total relative uncertainty for the aforementioned flow parameters in our experimental setup. In this context,  $\langle U \rangle$  denotes the bulk velocity,  $\mu_w$  represents the viscosity at the wall shear rate,  $Re$  signifies the Reynolds number,  $y$  denotes the wall-normal location,  $\tau_w$  represents the wall shear stress,  $u_\tau$  indicates the friction velocity,  $u^+$  denotes the inner scaled velocity, and  $C_f$  refers to the skin friction coefficient.

<b>Solution</b>	$\frac{\Delta\langle U \rangle}{\langle U \rangle}$	$\frac{\Delta\mu_w}{\mu_w}$	$\frac{\Delta y}{y}$
Water	0.071%	2.0%	1.24%
50 ppm PAM	0.078%	2.6%	1.24%
75 ppm PAM	0.075%	2.9%	1.26%
100 ppm PAM	0.077%	2.9%	1.16%
150 ppm PAM	0.072%	4.9%	1.17%

**Table 5 Estimated total uncertainties associated with independent flow variables.**

<b>Solution</b>	$\frac{\Delta Re}{Re}$	$\frac{\Delta\tau_w}{\tau_w}$	$\frac{\Delta u_\tau}{u_\tau}$	$\frac{\Delta u^+}{u^+}$	$\frac{\Delta C_f}{C_f}$
Water	2.00%	2.35%	1.18%	1.18%	2.36%
50 ppm PAM	2.60%	2.88%	1.44%	1.44%	2.88%
75 ppm PAM	2.90%	3.16%	1.58%	1.58%	3.17%
100 ppm PAM	2.90%	3.12%	1.56%	1.56%	3.13%
150 ppm PAM	4.90%	4.93%	2.52%	2.52%	4.93%

**Table 6 Estimated total uncertainties associated with calculated flow variables.**

## 4. Results

The PIV measurements were utilized to investigate the transition from laminar to turbulent flow as the  $Re$  increased for both Newtonian fluids and PAM fluids. Initially, the velocity measurements were conducted for the Newtonian case involving water. Subsequently, the PIV measurements were performed for PAM solutions with low concentrations, specifically at  $c = 50$  and  $75$  ppm. Following that, the measurements were conducted for high-concentration PAM solutions with  $c = 100$  and  $150$  ppm. To account for differences in rheology and the transition from laminar to turbulent behaviour, the results for low and high-concentration PAM solutions were separately presented. Each section showcases the variations in  $C_f$  and  $F_T$  as the Reynolds number increases. Additionally, instantaneous samples of  $U$  were captured along the streamwise-wall-normal and streamwise-spanwise planes at different Reynolds numbers, exhibiting characteristics of laminar, transitional, and turbulent flow fields as indicated by their corresponding  $F_T$  values.

## 4.1 Transition in Newtonian channel flow

Figure 4.1 illustrates the relationship between the skin friction coefficient,  $C_f$  and Reynolds number,  $Re$  for water channel flows. Each distinct cluster of data points, represented by different colours, corresponds to specific valve openings discussed in section chapter 3. The legend of Figure 4.1 provides the nominal Reynolds number for each valve opening. To ensure utmost accuracy and reliability, each valve opening was meticulously repeated six times, accompanied by the acquisition of long-duration double-frame data. This comprehensive approach aimed to achieve improved statistical convergence, especially in transitional flows characterized by sporadic intermittent turbulent patches.

For turbulent flows at higher  $Re$  the statistical convergence becomes less crucial. As a result, three repetitions of short-duration time-resolved measurements were performed for each valve setting with higher  $Re$ . The corresponding data, represented by hollow markers, are displayed in Figure 4.1. In contrast, the filled markers indicate the results obtained from long-duration double-frame measurements. The measured values of the skin friction coefficient are presented in conjunction with theoretical expectations for both laminar and turbulent channel flows. Specifically, for laminar flows, the expected relationship is  $C_f = 12/Re$ , while the power-law correlation proposed by Dean (1978),  $C_f = 0.073 Re^{-1/4}$ , represents the turbulent flows. To provide a baseline comparison, measurements of  $C_f$  from the channel flow experiments conducted by Patel & Head (1969) in high aspect ratio channels between  $Re$  values of

1000 and 7000 are also included in Figure 4.1, represented by gray markers. Each marker corresponds to a specific data point extracted from the experiments conducted by Patel & Head (1969), and the corresponding  $C_f$  and  $Re$  values have been digitized and recorded for reference.

At the lowest measured nominal  $Re$  of 1470, values of  $C_f$  agree well with the theoretical  $C_f$  line for laminar flows and the experimental results of Patel & Head (1969). As the nominal  $Re$  increases to 1930, the data points overlap with the experimental results of Patel & Head (1969). The repeated measurements show good agreement with one another within the estimated measurement uncertainty. As the nominal  $Re$  continues to increase,  $C_f$  gradually approaches the Dean (1978) equation for turbulent flows, indicating that the flow is becoming turbulent. Measurements of  $C_f$  acquired from short-time data collections form a cluster with a nominal  $Re$  of 2930 that still agrees with the results of Patel & Head (1969) and is slightly below the approaches the Dean (1978) equation for turbulent flows. As the nominal  $Re$  continues to increase beyond 3510 the measurements lie close to the empirical correlation of Dean's (1978). This implies that the measurements of  $C_f$  as a function of  $Re$  of water show good agreement with empirical Newtonian expectations in laminar and turbulent regimes, and reasonable conformance with previous experimental measurements of Newtonian transition in channel flows.

Iida & Nagano (1998) carried out a DNS investigation of turbulent channel flows. They decreased the Reynolds number to transitional values and studied relaminarization and turbulence statistics. They observed in the case of a decrease in

friction Reynolds number from  $Re_\tau = 80$  to 60, a quasi-laminar state appears in which the skin friction coefficient  $C_f$  is observed to be in between the laminar and turbulent values. This quasi-laminar state is characterized by a balance between Reynolds shear stresses and the collapse of the standard logarithmic law. The presence of the quasi-laminar state explains why  $C_f$  does not suddenly increase from the laminar to the turbulent values, but rather shows a gradual departure from laminar values and a gradual approach to turbulent values. Patel & Head (1969) and Jones (1976) observed the gradual deviation of the  $C_f$  value from the theoretical laminar values and its slow convergence towards the anticipated turbulent values. However, neither of these studies provided an explanation for this phenomenon.

The investigation by Yimprasert et al. (2021) delves into the transition from laminar to turbulent flow within a channel, with a particular emphasis on the evolution of the skin friction coefficient. Their experimental data adhered to the theoretical laminar line for low  $Re$ , but began to diverge at approximately  $Re = 1250$ , reaching a local maximum at  $Re = 1900$ . They further observed that the flow approached full turbulence for  $Re \geq 2600$ . Importantly, their skin friction values for  $Re > 2000$  were found to be in alignment with previous experimental and DNS results. However, they noted a discrepancy where their estimated skin friction deviated from the laminar line later than the skin friction measurements, suggesting that the non-turbulent region may not be purely laminar. Their attempts to model skin friction in the transitional region, based on intermittency and laminar and turbulent skin friction values, yielded lower values than those obtained experimentally. This suggests that regions of laminar

flow in close proximity to turbulent patches exhibit higher skin friction than those of undisturbed laminar flow.

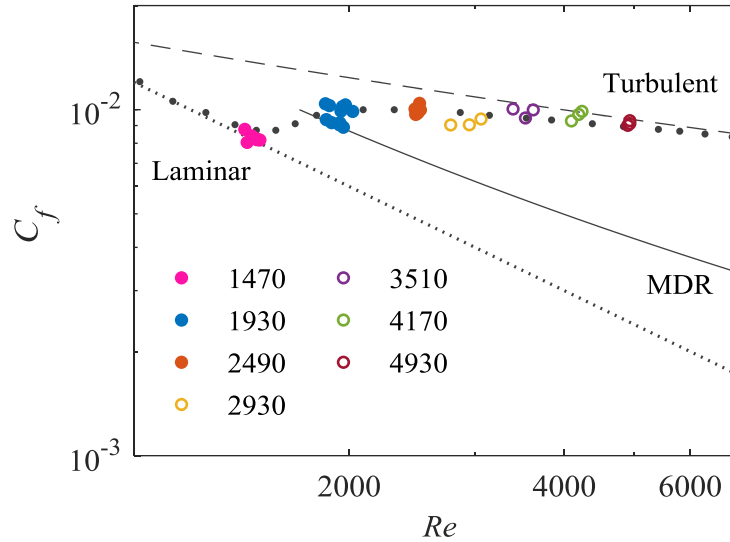


**Figure 4.1 Skin friction factor ( $C_f$ ) is plotted versus Reynolds number. The Patel & Head (1969) data is reproduced from their channel flow data. Filled symbols represent long-duration data measurements and hollow symbols show time-resolved measurements. The figure legend illustrates the nominal  $Re$  for each valve setting**

Figure 4.2 illustrates the percentage of turbulence,  $F_T$ , observed in the Newtonian flow of water. In accordance with the methodology outlined in section 3.5,  $F_T$  is determined as the proportion of time during which the flow is considered turbulent. At the nominal  $Re$  of 1470, measurements of six repeated tests show  $F_T$  values of zero implying the flow is laminar. Transitional flow features ( $F_T > 0$ ) are observed at measurements with  $Re = 1948, 1957$  and  $1913$ . At a slightly larger  $Re$  of 2200, the

flow becomes turbulent with  $F_T = 1$ . Beyond,  $Re$  of 2490 all flows are turbulent. The rapid transition process is evident based on the data points with the nominal  $Re$  of 1930 and a wide margin of  $F_T$  values between 0.41 and 0.84. These data points that fall between laminar and turbulent values of  $F_T$  in Figure 4.2 are scattered due to this rapid variation in the flow state and intermittency in the transitional flow. The abundance of turbulent patches and the amount of intermittency is not consistent among flows of the same nominal  $Re$  as they exhibit a wide range in  $F_T$  between 0 and 1. Assuming the transition  $Re$  band for water flow is 465 starting from  $Re = 1500$  up to  $Re = 1965$  and the critical  $Re$  of 1930 our observations agree with Patel & Head (1969) investigation that observed intermittency in the range of  $1380 \leq Re \leq 1800$ .

Sano & Tamai (2016) estimated a comparable parameter by quantifying the temporal fraction occupied by turbulent flow over an extended period of time. They conducted experiments at various downstream positions of a channel flow and observed that the transitional region commenced, i.e., the turbulence fraction increased from zero, at a  $Re$  of 1070. The authors derived the turbulence fraction using a flow visualization technique. However, their detection algorithm employed a simple binarization method with a minimal threshold, which may have potentially identified fluctuations unrelated to small-scale turbulence, leading to a lower  $Re$  for the onset of intermittency.

Another relevant parameter is the intermittency factor (Rotta 1956), which serves as a quantification of transitional flow fields encompassing both laminar and turbulent components. The intermittency factor is determined by calculating the ratio of the



total duration of turbulence to the overall duration. Rotta (1956) noted that in pipe flows, the occurrence of intermittency is observed within the range of Reynolds numbers approximately between 2200 and 2800. Seki & Matsubara (2012) devised a novel approach for determining the intermittency factor in channel flow, eliminating the requirement for a threshold value. Their investigation revealed that the lowest Reynolds number for fully developed turbulent flow is 2600, whereas the lower marginal  $Re$ , also referred to as the transition Reynolds number, is 1400. This finding aligns with our own observations of intermittency using the turbulent fraction. In general, our  $F_T$  data exhibits a consistent pattern of escalating turbulence fraction as the  $Re$  increases, corroborating earlier experimental studies.

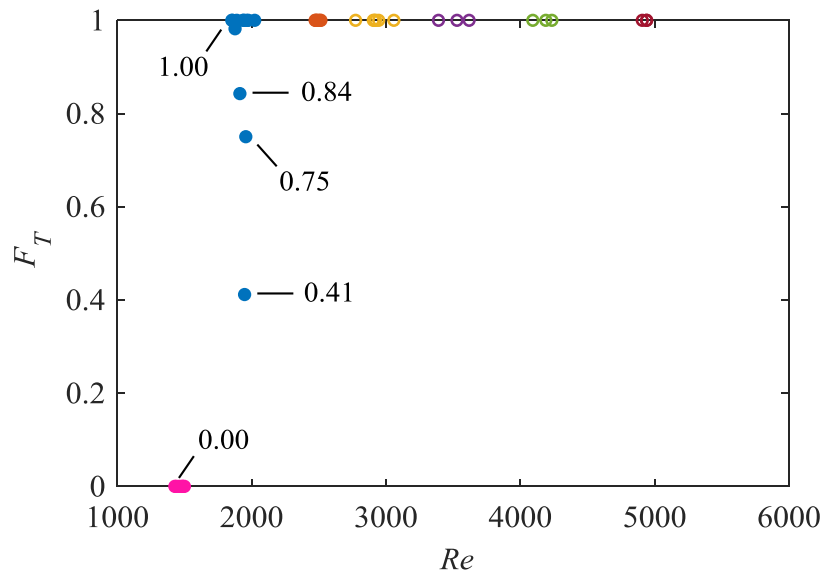


**Figure 4.2 The turbulent fraction ( $F_T$ ) for water is shown as a function of the Reynolds number. The annotation shows the  $F_T$  values for data points selected for further analysis in the subsequent figures.**

Sample measurements of  $U$  normalized by the mean centreline velocity  $\langle U_c \rangle$  along the streamwise-wall-normal plane are shown in Figure 4.3 for different channel flows of water at  $Re = 1400$  with  $F_T = 0$ ,  $Re = 1865$  with  $F_T = 0.68$  and  $Re = 1965$  with  $F_T = 1$ . The flow is moving from left to right here and the horizontal axis is the non-dimensionalized time  $t'$ . The vertical axis is the wall-normal position  $y$  normalized by channel half-height  $h$ .

For Figure 4.3(a) the turbulence intensity TI along the centreline of the flow is calculated to be as low as 1% based on equation (3.3). Figure 4.3(b) displays the transitional flow of the water experiment. The TI for the laminar section of this flow is calculated to be 1.2% and for the turbulent part, it is calculated to be 5.5%. Durst *et al.* (1998) conducted measurements of turbulence intensity in water channel flow during the laminar to turbulent transition. Their observations revealed that turbulence intensity remained below 2% up to  $Re$  of 2000. However, as  $Re$  increased to 4000, turbulence intensity surged and then reached a plateau at 4% for fully turbulent flows above  $Re = 8000$ . At small  $t'$ , the flow starts in a laminar state, then two turbulent spots emerge at  $t'$  of 130 and 220. The spots are confined by laminar regions and show abrupt changes in the velocity field. Moreover, the flow inside turbulent spots exhibits characteristics of fully turbulent flow with fluctuations that span the full channel height. These characteristics are consistent with the study of flow within turbulent spots previously investigated by Lemoult *et al.* (2014). Their study involved the generation of turbulent spots by introducing perturbations into a pressure-driven channel flow with an aspect ratio of 15 and  $Re$  of 1500. They investigated the spot

structure and flow around it. The shorter turbulent spots are followed by a turbulent region which lasts over 150 time units between  $t'$  of 300 to 430. After this turbulent region, the flow returns to a laminar state from  $t'$  of 430 to 500. Figure 4.3(c) displays the turbulent flow state in water at  $Re = 1965$ , where chaotic behaviour is observed and continuous variation in  $U$  can be noticed at all values of  $y/h$  and  $t'$ . The TI value for this flow is calculated to be 5.5%.

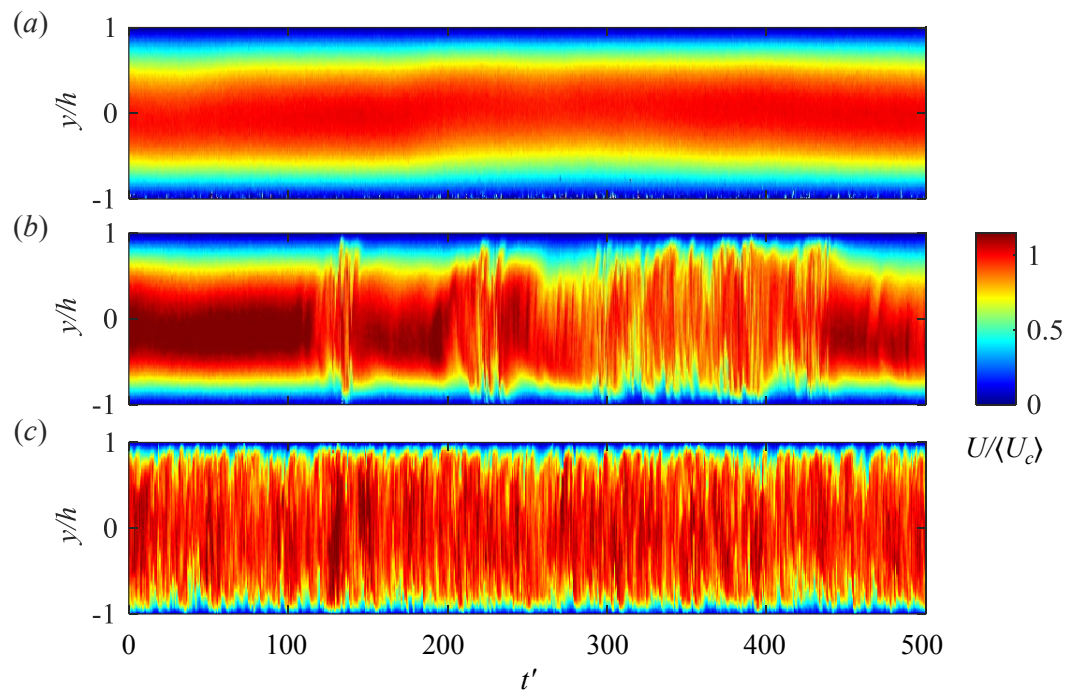


**Figure 4.3 Spatial contours of normalized streamwise velocity ( $U/U_c$ ) from streamwise-wall-normal measurements presenting (a) laminar, (b) transitional with  $F_T = 0.41$  and (c) turbulent flow fields for water. The Reynolds number is 1400, 1870 and 2550, respectively.**

The contours of  $U/\langle U_c \rangle$  along the streamwise-spanwise plane at  $y = 0$  for laminar, transitional and turbulent flows of water are shown in Figure 4.4. In order to keep consistency with streamwise-wall-normal results,  $\langle U_c \rangle$  is calculated along  $z = 0$  for streamwise-spanwise results. Similar to Figure 4.3, the horizontal axis is  $t'$ , however, the vertical axes now correspond to the spanwise position  $z$  normalized by  $h$ . In Figure 4.4(a) there is some evidence of low-frequency streamwise streaks. However, along  $z = 0$ , TI is low and approximately equal to 1.2%, which agrees well with the laminar TI from wall-normal results. Furthermore, Figure 4.4(a) does not show the chaotic mixing behaviour commonly seen in turbulent flows. Seki & Matsubara (2012) noted that the velocity fluctuation in the upstream flow of high Reynolds number laminar cases possessed sufficiently high and broad spectral components. These served as the upstream disturbance for their experiment. A particular point of interest was the identification of a low-frequency peak. According to the previous flow visualizations conducted by their research group (2011; 2006), this scale is larger than the turbulent disturbance scale, yet smaller than that of the turbulent patch passing. The low-frequency events observed in Figure 4.4(a) could potentially be attributed to the observations made by Seki & Matsubara (2012). Considering the  $\langle U_c \rangle = 0.134$  m/s for the flow field shown in Figure 4.4(a) and comparing it to a flow with a similar valve opening measured along the streamwise-wall-normal plane from Figure 4.3(a) with  $\langle U_c \rangle = 0.133$  m/s, it can be concluded that the  $Re$  for Figure 4.4(a) should be close to 1470. Figure 4.4(b) shows measurements of  $U/\langle U_c \rangle$  along the streamwise-spanwise plane for a transitional flow of water. Between  $t'$  of 0 and 100, a turbulent region

passes, followed by elongated low-speed streaks connected to its trailing edge. The instability starts again at the  $t'$  of 350, and a turbulent spot emerges at  $t'$  of approximately 450. The observed turbulent spot is connected to a low-speed streak in its leading point and has oblique fronts between the core turbulent region and surrounding laminar flow on its sides. The  $Re$  of a flow with a similar valve opening measured along the streamwise-wall-normal plane is approximately 1930. These observations agree well with flow visualizations conducted by Carlson *et al.* (1982), who demonstrated that the turbulent spots in channel flows have a distinct arrowhead shape. Moreover, in contrast to the hairpin-dominated spots observed in boundary layers (Schröder *et al.* 2008), channel spots are characterized by semiregular streamwise streaks accompanied by localized chaotic eddies (Wu 2023). Another noteworthy feature of channel spots is the presence of oblique wave packets emanating from the spanwise wingtips observed by Henningson & Kim (1991). Lemoult *et al.* (2014) also discovered the travelling-wave-like structures near the trailing edge of a turbulent spot. Similar structures are observed in Figure 4.4(b) from  $t' = 350$  up to  $t' = 450$ . Consequently, channel flow spots consist of three distinct regions: a central turbulent eddy region, a wingtip wave region, and a streamwise streak region. Figure 4.4(c) displays  $U/\langle U_c \rangle$  for a turbulent flow of water. As expected, the turbulent state demonstrates a fully chaotic behaviour that extends fully along the measured domain of  $z$ . A flow with a similar valve opening measured along the streamwise-wall-normal plane has  $Re = 2490$ .

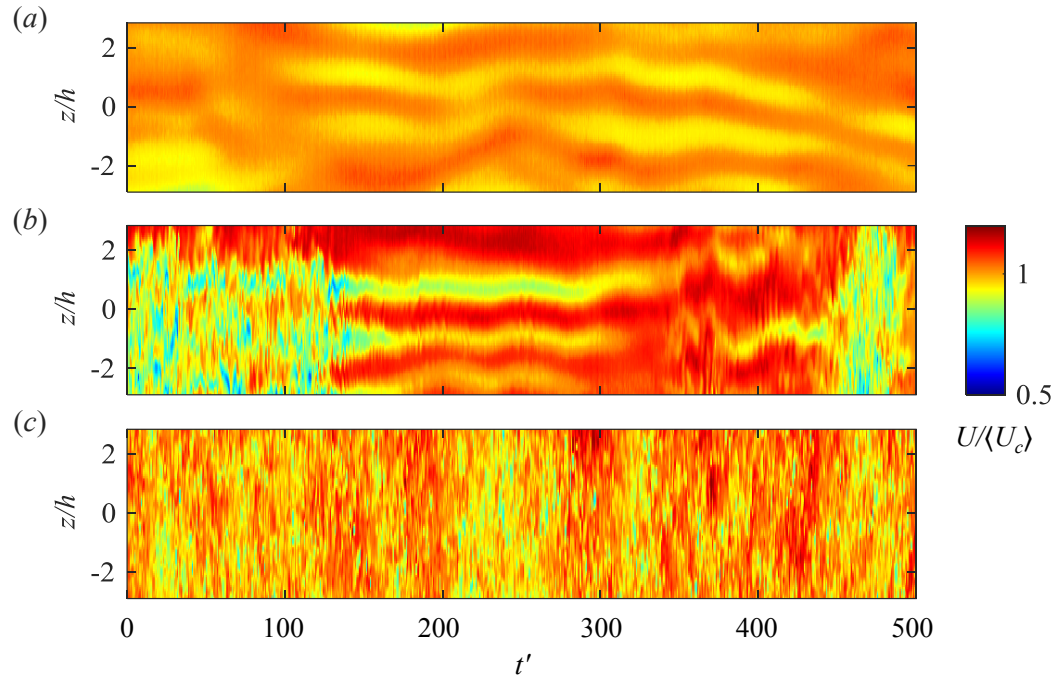


**Figure 4.4 Spatial contours of normalized streamwise velocity,  $U/\langle U_c \rangle$ , from streamwise-spanwise PIV measurements showing (a) laminar,  $Re \approx 1470$ , (b) transitional,  $Re \approx 1930$  and (c) turbulent,  $Re \approx 2490$  flow fields for water experiments.**

Figure 4.5(a) shows outer-scaled velocity profiles of water flows for five different values of  $F_T$ . This figure also shows the theoretical parabolic velocity profile for laminar flows and a mean velocity profile derived from direct numerical simulation (DNS) of Iwamoto *et al.* (2002) for a turbulent Newtonian channel flow at low  $Re_\tau = 110$ . Due to the intermittent nature of transitional flow fields, their velocity profiles exhibit asymmetry, and the maximum streamwise velocity value across the channel height may not occur at the channel centerline. Therefore, the mean streamwise velocity  $\langle U \rangle$  is normalized using the maximum velocity across the channel,  $U_0$ , instead

of centerline velocity  $U_c$ . The cases shown in Figure 4.5 correspond to the flow cases with  $F_T$  values specified in Figure 4.2. As seen in Figure 4.5(a), measurements of  $\langle U \rangle / U_0$  for the laminar flow of water with an  $F_T = 0$  and  $Re = 1460$ , agree well with the theoretical parabolic velocity profile. As  $F_T$  increases, the velocity profiles begin to deviate from the Poiseuille laminar trend, and have profiles of  $\langle U \rangle / U_0$  that fall between the laminar and turbulent profiles. The velocity profiles falling between the laminar and turbulent profiles can be explained by the intermittency of the flow, which shows periods of laminar and turbulent behaviour. Intermittency refers to the coexistence of laminar and turbulent domains in some range of flow conditions. Despite the long data acquisition time, the transitional velocity profiles are still prone to asymmetry. This suggests that turbulent spots within the transitional flows occur at low frequencies and longer acquisition times are still needed to obtain better statistical convergence in  $\langle U \rangle$  for the transitional flows. Finally, measurements of  $\langle U \rangle$  for the turbulent flow of water with  $Re = 1850$  (equivalent to  $Re_\tau = 90$ ) agree well with the DNS from (Iwamoto *et al.* 2002) at  $Re_\tau = 110$ . Overall, the measurements of  $\langle U \rangle / U_0$  shown in Figure 4.5(a) are consistent with expectations for a Newtonian channel flow undergoing laminar to turbulent transition.

In Figure 4.5(b), inner-normalized profiles of  $\langle U \rangle^+$  versus  $y^+$  for the same water flows detailed in Figure 4.5(a) are demonstrated. Dashed lines show  $\langle U \rangle^+ = y^+$  for the viscous sublayer and the logarithmic law of the wall,  $\langle U \rangle^+ = 2.44 \ln y^+ + 5.5$  for the logarithmic layer. In order to generate inner-normalized velocity profiles, the velocity profiles were subjected to averaging in the vicinity of the channel centerline ( $y = 0$ ).

This procedure ensures the attainment of symmetric velocity profiles, even in cases exhibiting asymmetry. Subsequently, the inner-scaled velocity profiles were derived by utilizing the aforementioned averaged velocity profiles. Figure 4.5(b) indicates that the laminar flow has the largest positive offset relative to the logarithmic law of the wall. As  $F_T$  increases,  $\langle U \rangle^+$  gets closer to the logarithmic law of the wall. This indicates that the turbulent flow is more closely aligned with the expected logarithmic profile near the wall. However, as seen in Iwamoto (2002), turbulent flow at a low  $Re_\tau$  of 110 is not expected to perfectly follow the logarithmic law of the wall. Our experiments also show this phenomenon for the case at  $Re = 1850$  with  $F_T=1$ , with the turbulent velocity profiles deviating from the logarithmic law of the wall at low Reynolds numbers.

The mean dynamics of channel flow in the transitional state were investigated by Elsnaab *et al.* (2011). They observed in the transitional regime, the mean velocity profiles gradually flatten with increasing Reynolds number. The shape of the profiles they acquired are similar to that reported by Orszag & Kells (1980) for laminar channel flow perturbed by finite amplitude two and three-dimensional Orr-Sommerfeld eigenfunctions. Furthermore, Elsnaab *et al.* (2011) observed when plotted on semi-logarithmic axes, all of the inner-normalized mean profile measurements converge onto a single curve for  $y^+ \lesssim 15$ . However, these profiles deviate slightly from the linear viscous sublayer. Moreover, at  $y^+ > 30$ , the higher Reynolds number profiles exhibit a logarithmic-like dependence.



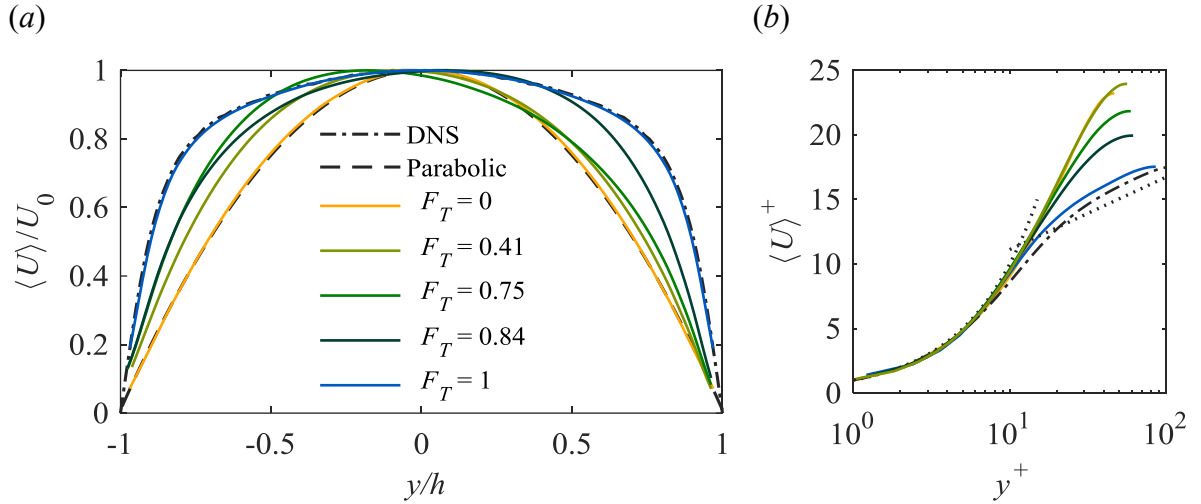


**Figure 4.5** The velocity profiles for various turbulent fractions of water flow are illustrated in (a) outer scaling and (b) inner scaling. Reynolds numbers in order of increasing  $F_T$  are: 1460, 1950, 1960, 1910, 1850. The DNS is from Iwamoto (2002), and the parabolic function is the theoretical velocity profile for laminar channel flows. The dotted lines show the viscous sublayer and logarithmic law of the wall.

## 4.2 Transition for low-concentration PAM solutions

Figure 4.6 and Figure 4.7 displays  $C_f$  versus  $Re$  for the 50 and 75 ppm solutions of PAM respectively. The maximum drag reduction (MDR) asymptote shown with solid line follows  $C_f^{1/2} = 19 \log_{10}(Re C_f^{1/2}) - 32.4$  (Virk et al. 1970).

For the 50 ppm PAM solution, time-resolved data acquisition was employed to collect data at two valve settings with low  $Re$  and three valve settings with higher  $Re$  values beyond the transitional range. Data at two valve settings within the transitional  $Re$  zone were gathered using the long-duration double-frame system. The lowest nominal  $Re$  of 1080 has  $C_f$  values that overlap with the theoretical laminar value  $C_f = 12/Re$ . With a further increase of nominal  $Re$  to 1590, it can be observed that values of  $C_f$  continue to follow the laminar trend and deviate from the Newtonian transition

seen from Patel & Head (1969). At the nominal  $Re$  of approximately 2070 measurements of  $C_f$  are scattered, indicating the presence of a transitional flow. The data points lie between the Newtonian laminar and turbulent trends, marking the start of drag reduction. The scatter in the data points continues also at  $Re = 2460$ . At nominal  $Re$  of 2780, the data attain values of  $C_f$  higher than MDR but lower than the Newtonian turbulent trend. With rising the nominal  $Re$  to values of 3310 and 3710, two clusters of data points show a decreasing trend in skin friction coefficient below Patel & Head (1969) values.

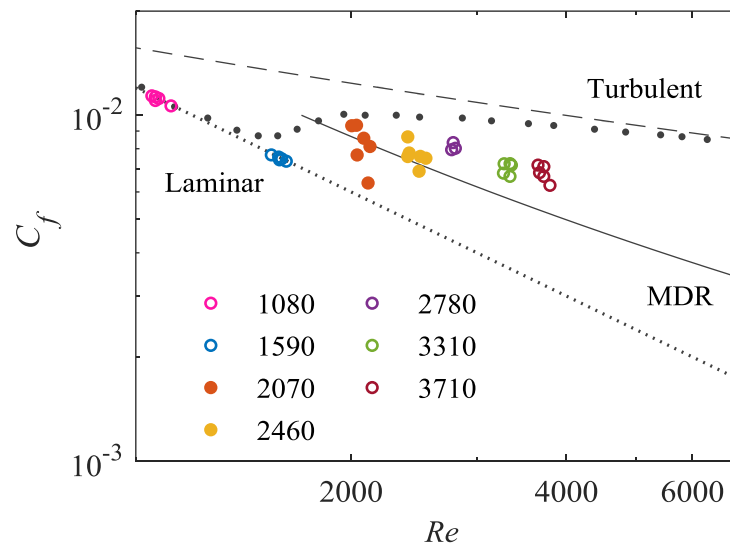


**Figure 4.6 Skin friction factor ( $C_f$ ) plotted as a function of the Reynolds number for 50 ppm solutions of PAM. Patel & Head (1969) data is shown as grey filled circles. Filled symbols represent long-duration data measurements and hollow symbols show time-resolved measurements.**

For PAM solutions with a  $c$  of 75 ppm, the measurements of  $C_f$  at the nominal  $Re$  of 1290 fall on the laminar trend, as shown in Figure 4.7. At the nominal  $Re$  of 1750, the data points start to deviate from the theoretical laminar trend and become slightly scattered. With an increase in the nominal  $Re$  to 2080, repeated measurements show a range of different  $C_f$  values that fall between the laminar and MDR lines, indicating a transitional state. Increasing the  $Re$  to 2800, the  $C_f$  grows to a value relatively close to Patel & Head (1969). Increasing nominal  $Re$  further to 3210 and 3570, the next two clusters of  $C_f$  measurements show a descending trend toward MDR asymptote and well below the experimental measurements of Patel & Head (1969). The data shows that the  $C_f$  exhibited a clear relationship with  $Re$  beyond a specific onset point of  $Re = 2780$  for 50 ppm and  $Re = 2740$  for 75 ppm. The slope in  $C_f$  reduction with increasing  $Re$  differs from the turbulent friction factor correlation proposed by Dean (1978) This finding aligns with the type A behaviour discussed in Virk & Wagger (1990). In type A drag reduction, a distinct onset point for drag reduction can be identified. Prior to this point, the  $C_f$  increases with  $Re$ ; however, once the drag reduction initiates, it demonstrates a proportional increase with  $Re$ . In other words,  $C_f$  values decrease at a higher rate with increasing  $Re$  compared to the  $C_f$ - $Re$  trend for water flow. Concerning the transition from laminar to turbulent flow, type A drag reduction exhibits a transition to turbulence, accompanied by an increase in  $C_f$ . Subsequently, after drag reduction onset, as  $Re$  values continue to rise,  $C_f$  will decrease and skin friction values will approach the MDR values from above.

Overall, measurements of  $C_f$  as a function of  $Re$  are different from the results of water, shown in Figure 4.1, and the previous experimental data for Newtonian channel flows reported by Patel & Head (1969). Our measurements show that at certain  $Re$ , the skin friction factor values fall between the laminar and turbulent trends, and there is a positive relationship between drag reduction and Reynolds number beyond the onset point.

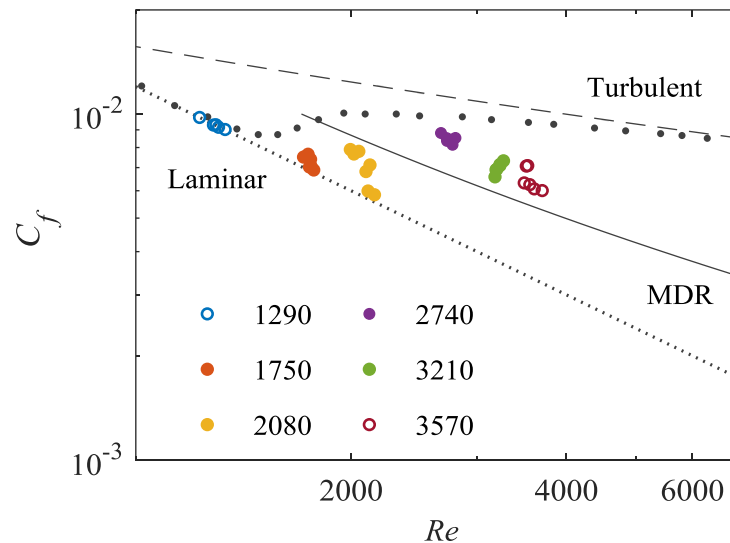


**Figure 4.7 Skin friction factor ( $C_f$ ) plotted as a function of the Reynolds number for 75 ppm solutions of PAM. Patel & Head (1969) data is shown as grey filled circles. Filled symbols represent long-duration data measurements and hollow symbols show time-resolved measurements.**

The turbulent fraction  $F_T$  with respect to  $Re$  is shown in Figure 4.8 for the 50 ppm PAM solution. Flows of the 50 ppm solutions at nominal  $Re$  of 1080 and 1590 have  $F_T$  values equal to zero and are therefore, laminar. At the nominal  $Re$  of 2070, six

repeats of measurements show a wide range of  $F_T$  values between 0.1 and 1.0. This wide range of  $F_T$  values at an approximately constant  $Re$  demonstrates how turbulence can arise suddenly in a narrow  $Re$  band for the 50 ppm PAM solution. Increasing the nominal  $Re$  further to values greater than or equal to 2460 produces chaotic flows that generally have an  $F_T$  of 1.0.

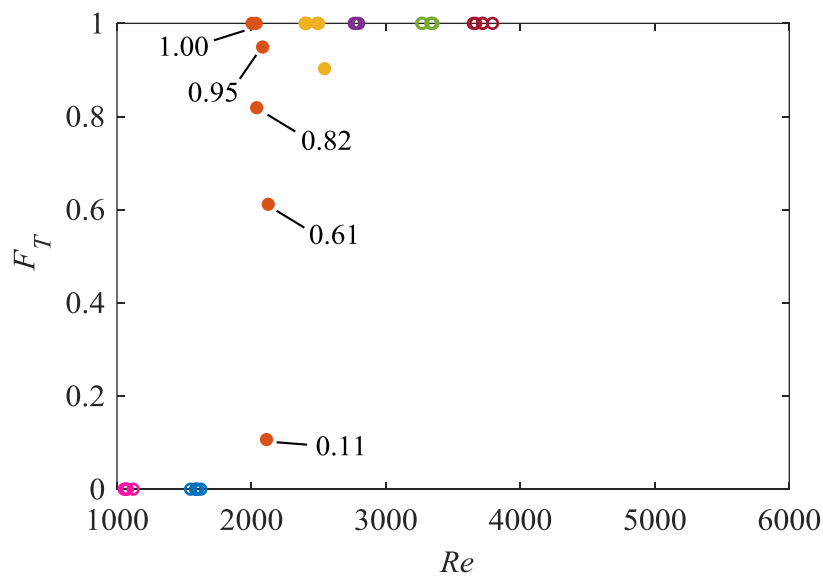


**Figure 4.8 The turbulent fraction ( $F_T$ ) for 50 ppm solutions of PAM is shown versus the Reynolds number. Colours show nominal  $Re$  same as Figure 4.6. Filled symbols represent long-duration data measurements and hollow symbols show time-resolved measurements. The velocity profiles for data points with annotated  $F_T$  will be illustrated.**

Figure 4.9 demonstrates values of  $F_T$  versus  $Re$  for the 75 ppm flows. At nominal  $Re$  of 1290, all measurements reflect laminar conditions with values of  $F_T$  equal to 0. Transition to an intermittent condition sets in at nominal  $Re$  of 1750 with variations

in  $F_T$  that range from 0 to 0.44. The laminar-turbulent intermittency continues at nominal  $Re$  of 2080 with measurements showing a wide range of  $F_T$  from 0 to 0.73. Finally, for all measurements above  $Re$  of 2740, the flow is chaotic with all measurements of  $F_T$  being equal to 1.

Together, Figure 4.8 and Figure 4.9 show that the onset of turbulence in the low-concentration polymer flows is delayed slightly to  $Re = 2070$  and  $Re = 2080$  for 50 ppm and 75 ppm solutions, respectively, compared to the Newtonian flows with transition  $Re$  of 1930 detailed in Figure 4.2. This is in line with the theory of Samanta *et al.* (2013) and other investigations (Draad *et al.* 1998; Escudier *et al.* 1998; Giles & Pettit 1967; Pinho & Whitelaw 1990), that flexible polymers suppress Newtonian turbulence and delay the transition. Furthermore, the transitional  $Re$  band (the difference between the highest  $Re$  with  $F_T = 0$  and lowest  $Re$  with  $F_T = 1$ ) covers a wider range of  $Re$  as the polymers are introduced to flow. Compared to the 465 transitional  $Re$  band for water, 50 ppm solution shows 1045 and 75 ppm shows 1005 transitional  $Re$  band.

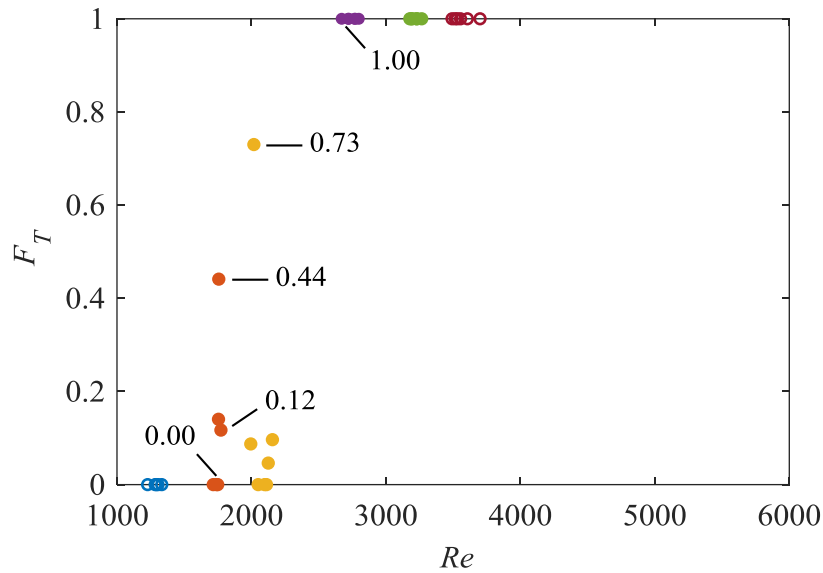


**Figure 4.9** The turbulent fraction ( $F_T$ ) for 75 ppm solutions of PAM is shown versus the Reynolds number. Colours show nominal  $Re$  same as Figure 4.7. Filled symbols represent long-duration data measurements and hollow symbols show time-resolved measurements. The velocity profiles for data points with annotated  $F_T$  will be illustrated.

Figure 4.10 demonstrates the contours of  $U/\langle U_c \rangle$  measured along the streamwise-wall-normal plane of the PAM solutions with different values of  $F_T$ . Figure 4.10(a) demonstrates the laminar flow of the 75 ppm solution, with an  $F_T = 0$  at  $Re = 1720$ . As expected, the flow is visually steady and does not show any significant variations of  $U/\langle U_c \rangle$  over  $t'$ . Turbulence intensity for this case is measured to be 1.1%. Figure 4.10(b) displays  $U/\langle U_c \rangle$  for the 50 ppm solution in a transitional state, with an  $F_T$  value of 0.61 and  $Re = 2125$ . This transitional flow exhibits several turbulent spots interspersed between laminar regions. The turbulence observed in low concentration solutions appears to be similar to the Newtonian turbulent spot shown in Figure 4.3(b).

Lastly, Figure 4.10(c) demonstrates  $U/\langle U_c \rangle$  for the 75 ppm PAM solution in a turbulent state and at  $Re = 2670$ . Despite having a lower  $C_f$  than Newtonian turbulence – demonstrated by Figure 4.6– the spatial patterns of  $U/\langle U_c \rangle$  are visually similar to water with an  $F_T$  of 1 seen in Figure 4.3(c). Specifically, both flows are disordered for all instances of  $t'$ , with no apparent regions of calm laminar flow seen previously in Figure 4.3(b) and Figure 4.10(b).

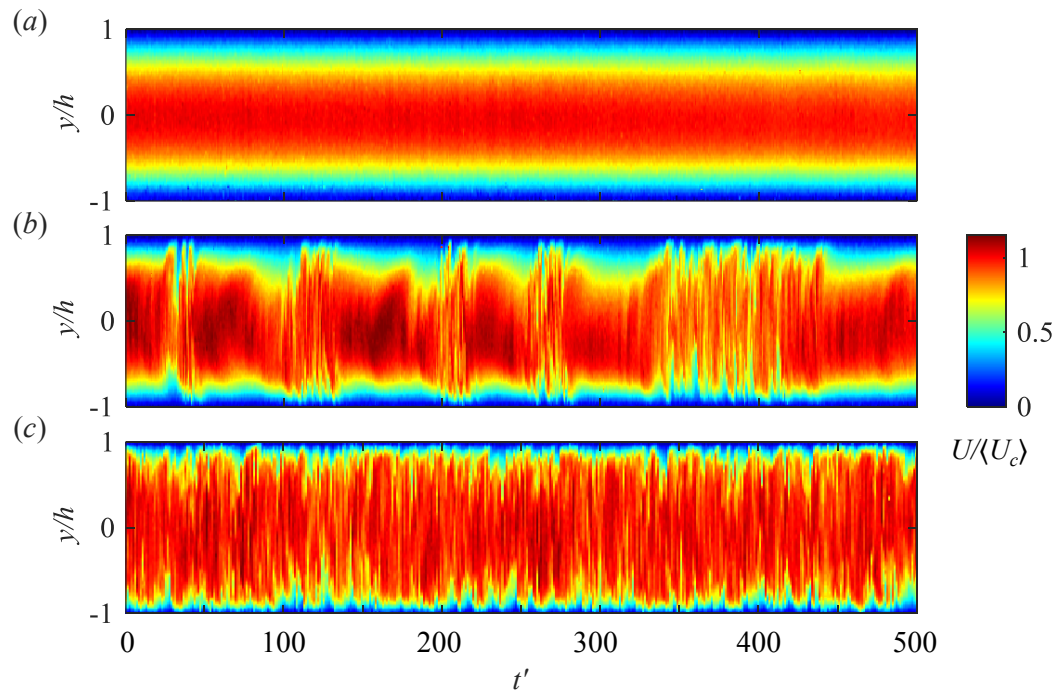


**Figure 4.10** Spatial contours of normalized streamwise velocity ( $U/\langle U_c \rangle$ ) from streamwise wall-normal measurements of three different flow states of low-concentration PAM solutions (a) 75 ppm laminar,  $Re = 1720$ , (b) 50 ppm,  $F_T = 0.61$ ,  $Re = 2125$ , (c) 75 ppm turbulent,  $Re = 2670$ .



In Figure 4.11, contours of  $U/\langle U_c \rangle$  along the streamwise-spanwise plane are shown for flows with different values of  $F_T$ . In Figure 4.11(a), the laminar flow with an  $F_T = 0$  at  $Re = 1750$  does not show any considerable variation in  $U/\langle U_c \rangle$ . The turbulence intensity of this case has been measured to be 1%. However, for the transitional case shown in Figure 4.11(b) with  $Re \approx 2080$ , variations in  $U/\langle U_c \rangle$  along  $z$  and  $t'$  are present. Elongated streaks of low  $U/\langle U_c \rangle$  are observed between  $t' = 0$  and 200. Beyond  $t' = 200$ , the streamwise streaks become increasingly chaotic and exhibit fluctuations in  $U/\langle U_c \rangle$  that span the complete measurements domain along  $z$ . The chaotic region is extended to  $t' = 450$ , after which the flow recovers to a relatively, calm and laminar state. The central turbulent eddy region within this chaotic structure bears a resemblance to turbulent spots observed in Newtonian flows (Wu 2023), albeit lacking the distinctive arrowhead shape. Instead, the leading edge of this chaotic structure is connected to streamwise streaks, and the instability persists into the turbulent eddy core. Lastly, Figure 4.11(c) shows the chaotic flow of PAM with  $c = 75$  ppm and  $F_T = 1$  at  $Re = 3210$ . Comparing Figure 4.11(c) to the streamwise-spanwise plane measurements of water in Figure 4.4(c) demonstrates that the drag-reduced chaotic state is not visually different from pure Newtonian turbulence.

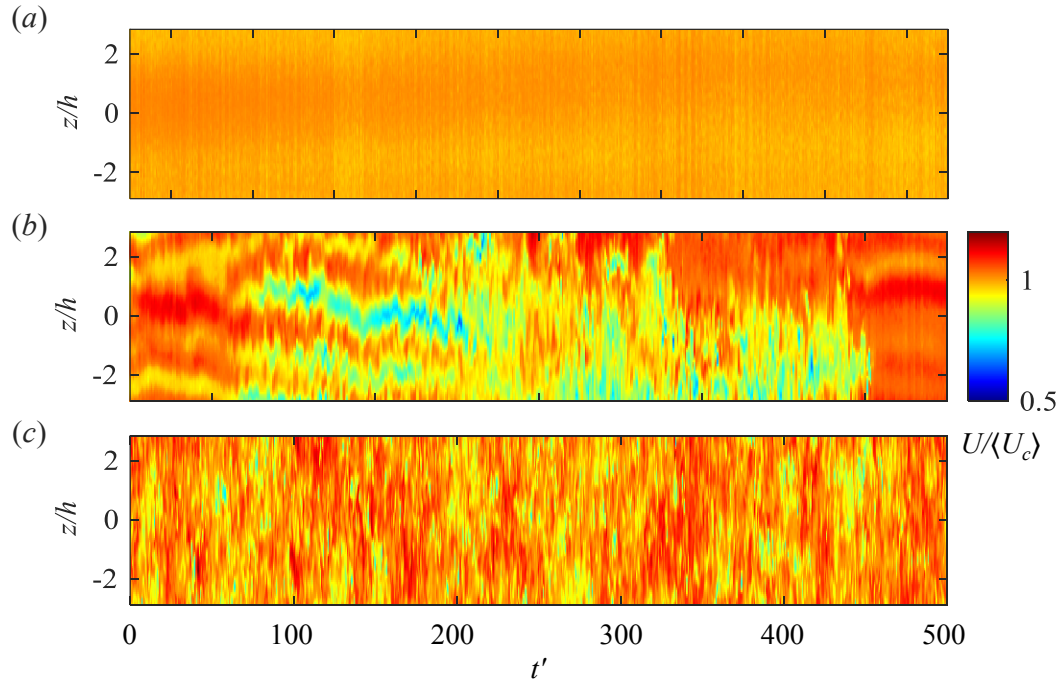


**Figure 4.11 Spatial contours of normalized streamwise velocity,  $U/\langle U_c \rangle$ , from streamwise spanwise measurements for (a) laminar  $Re \approx 1750$ , (b) transitional  $Re \approx 2080$  and (c) turbulent flows  $Re \approx 3210$  in 75ppm solution.**

In Figure 4.12(a) and (b), the mean streamwise velocity normalized by the average maximum velocity across the channel,  $\langle U \rangle / U_0$ , is plotted with respect to  $y/h$  for the 50 and 75 ppm PAM solutions. Similar to the Newtonian transitional flows shown in Figure 4.5(a), transitional flow conditions of low-concentration PAM flows with  $0 < F_T < 1$ , also have an asymmetric velocity profile about  $y = 0$ . On the other hand, laminar flows with  $F_T$  values equal to 0, and turbulent flows with  $F_T$  of 1, are symmetric about  $y = 0$ . Additionally, we see that the velocity profiles become blunt with increasing  $F_T$  values, similar to what was previously observed in the Newtonian case shown in Figure 4.5(a).

Figure 4.12(c) and (d) demonstrate the inner-scaled velocity profiles for low-concentration PAM solutions with  $c = 50$  and  $75$  ppm. The MDR velocity profile  $\langle U \rangle^+ = 11.7 \ln y^+ - 17.0$  is shown as a dashed line (Virk 1975). It can be seen that profiles with the lowest  $F_T$  values have the largest departure from the logarithmic law of the wall. As  $F_T$  increases, profiles of  $\langle U \rangle^+$  begin to approach the logarithmic law of the wall for Newtonian flows. For flows with an  $F_T = 1$ , the difference between the measured  $\langle U \rangle^+$  within the outer layer and the Newtonian log-law tends to increase as  $c$  increases from 50 to 75 ppm — compare the blue profiles in Figure 4.12(c) with Figure 4.12(d). This is consistent with previous studies that the upward shift in the outer layer of the inner scaled velocity profile is proportionate to the drag-reduction level (Virk 1971; White *et al.* 2012).

Low-concentration PAM solutions demonstrated a deviation from the expected skin friction values for Newtonian turbulent flows. This deviation, which can be attributed to the drag-reducing effect of polymers, was observed at various  $Re$  for 50 ppm and 75 ppm PAM solutions. Furthermore, low-concentration PAM solutions exhibited onset phenomena for drag reduction. This implies that the skin friction values increased with increasing Reynolds number until reaching the onset point, after which they decreased as drag reduction took effect with further increases in Reynolds number. Values of  $F_T$  also indicated a transition from laminar to turbulent flow at specific  $Re$  that was generally higher than the critical  $Re$  of the Newtonian flows. Overall, the results demonstrated that the channel flow of low-concentration PAM solutions have a delayed transition to turbulence and less skin friction at higher  $Re$

than Newtonian channel flows. Moreover, velocity profiles show that low-concentration PAM solutions exhibit asymmetry in transitional flow conditions, with profiles becoming blunter as  $F_T$  values increase, similar to Newtonian cases. Inner-scaled velocity profiles for low-concentration solutions reveal that profiles with lower  $F_T$  values deviate more from the logarithmic law of the wall, while profiles approach the law as  $F_T$  increases. Furthermore, when concentration increases from 50 ppm to 75 ppm for flows with  $F_T$  of 1, the difference between measured  $\langle U \rangle^+$  and the Newtonian log law grows, indicating an upward shift in the outer layer of the inner-scaled velocity profile proportional to the drag reduction level. The turbulent spots observed in low concentration solutions appear similar in morphology to Newtonian turbulent spots, albeit slightly more elongated streaks were present connecting to the leading edge.

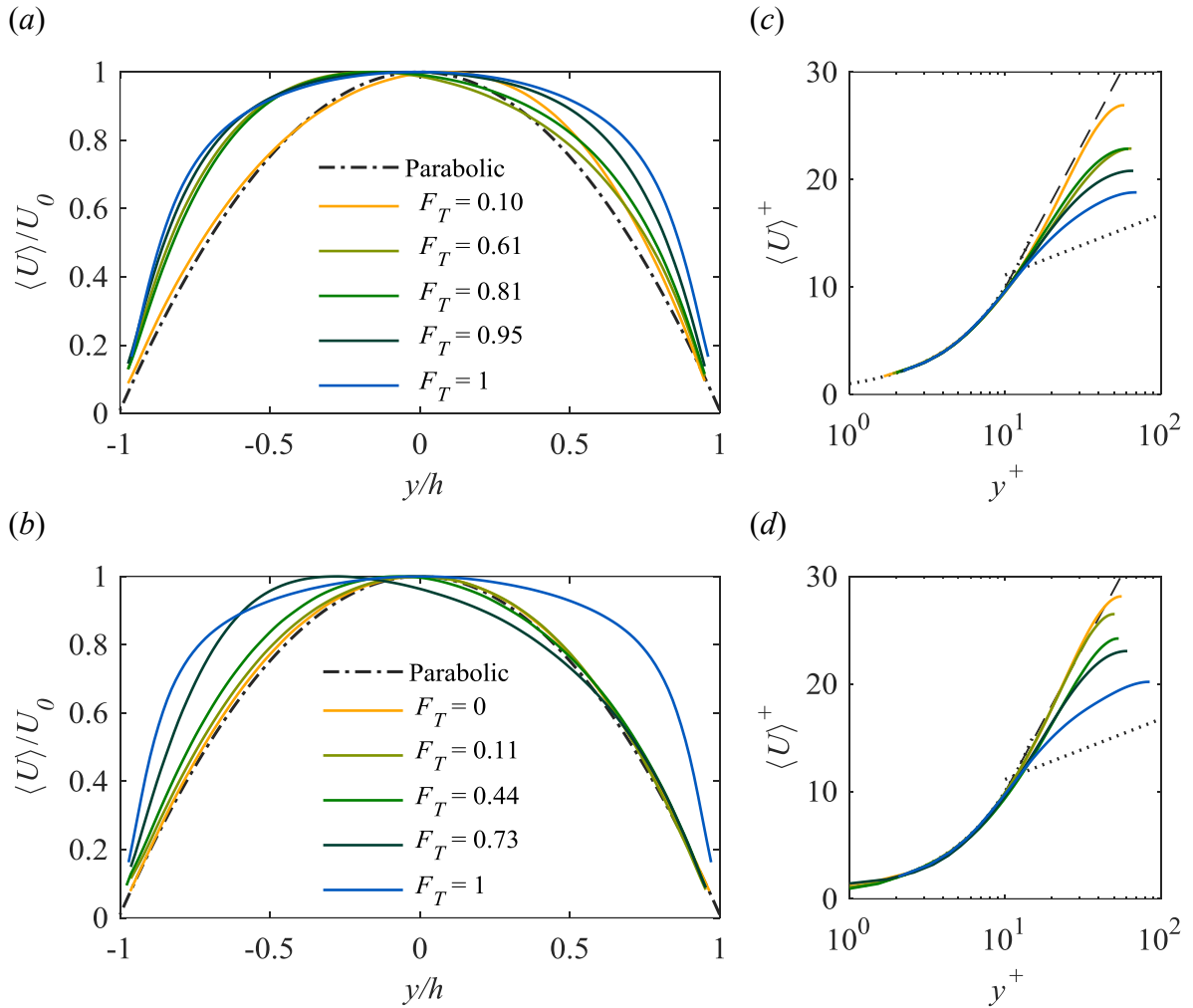


**Figure 4.12** The velocity profile for laminar, transitional and turbulent cases for low-concentration solutions are plotted for (a) 50 ppm outer scaling, and (c) 50 ppm inner scaling. Reynolds numbers in order of increasing  $F_T$ : 1460, 1950, 1960, 1910, 1850 (b) 75 ppm outer scaling, (d) 75 ppm inner scaling. Reynolds numbers in order of increasing  $F_T$ : 1750, 1775, 1760, 2020, 2670. Dotted lines show the viscous sublayer and logarithmic law of the wall; Virk's (1970) velocity profile is shown with a dash-dot line.

### 4.3 Transition for high-concentration PAM solutions

Larger concentration PAM solutions, with  $c$  of 100 and 150 ppm, demonstrated distinct behaviours compared to both Newtonian and lower concentration PAM flows. In this section, the results of the 100 and 150 ppm solution experiments are presented. Measurements of  $C_f$  for the 100 ppm PAM solution, are shown in Figure 4.13. Time-resolved data collection was used to acquire data for a valve setting with low  $Re$ . Then three valve settings with  $Re$  in the transitional range were tested using long-duration double-frame data collection. Consequently, the data for the valve setting with the highest  $Re$  was collected using the time-resolved high-speed system. The first cluster of  $C_f$  measurements at nominal  $Re$  values of 1530 overlap with the expected  $C_f$  values for laminar flow. The next measurements at  $Re = 2280$  start to deviate from the laminar trend. Measurements of  $C_f$  at nominal  $Re$  of 3310 continue to depart from the laminar trend with repeated data points showing a wide range of values between the laminar and MDR trends in  $C_f$  versus  $Re$ . At nominal  $Re$  of 4570, the scatter of repeated measurements gets smaller. Measurements of  $C_f$  for nominal  $Re = 5350$  overlap with each other and lie on the MDR asymptote.

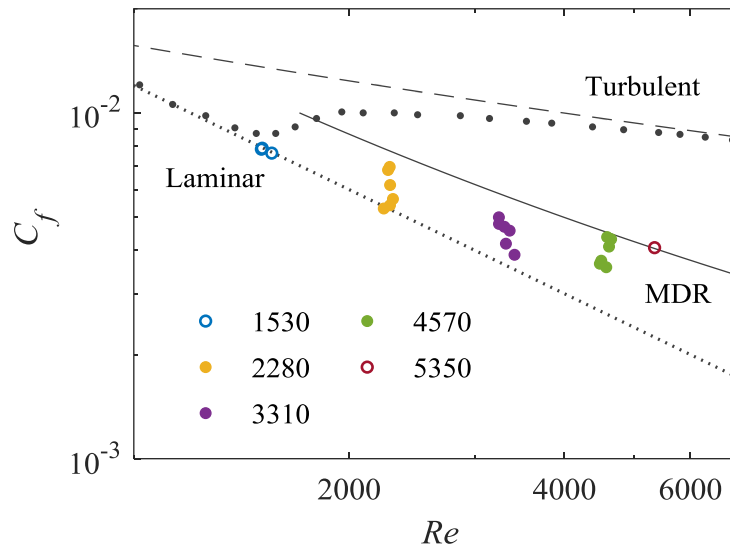


**Figure 4.13 Skin friction factor ( $C_f$ ) plotted as a function of the Reynolds number for 100 ppm solutions of PAM. Patel & Head (1969) data is shown as grey filled circles. Filled symbols represent long-duration data measurements and hollow symbols show time-resolved measurements.**

Figure 4.14 demonstrates the measurements of  $C_f$  for the 150 ppm PAM flows as a function of  $Re$ . Below the nominal  $Re$  of 2810, all measurements of  $C_f$  follow the laminar trend closely. It is not until the nominal  $Re$  of 3670 that values of  $C_f$  begin to deviate from the laminar trend. The deviation between measurements of  $C_f$  for the 150 ppm PAM flow and the laminar  $C_f$  versus  $Re$  trend increases as  $Re$  grows from 3670 to 4640. Eventually, at the nominal  $Re$  of 5370, measurements of  $C_f$  reach the MDR asymptote. Overall, we observed that the skin friction factor values for high-concentration PAM solutions exhibit type B drag reduction characteristics. This is evidenced by the absence of an increase in the skin friction coefficient with increasing Reynolds number prior to the onset of drag reduction, indicating that no onset

phenomena were detected. Furthermore, the flow does not transition to Newtonian turbulence. Instead, by increasing  $Re$ , the skin friction factor departs from laminar values, entering a state of drag-reduced turbulence. As the Reynolds number increases further,  $C_f$  data approaches the MDR values from below.

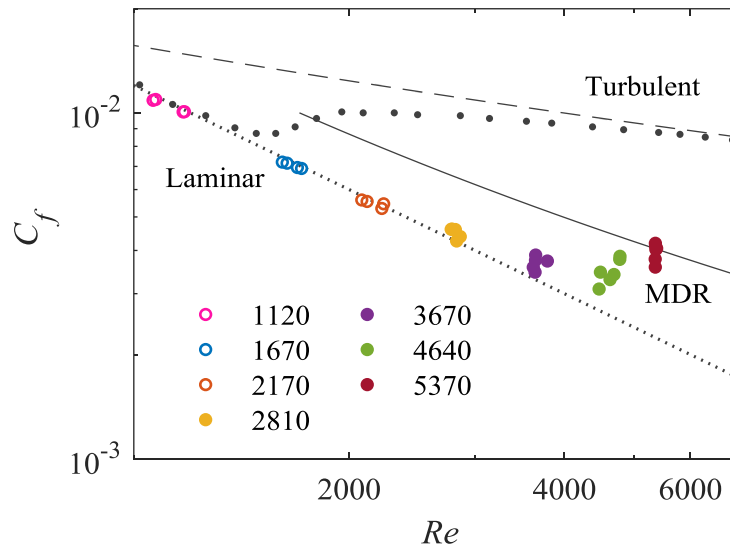


**Figure 4.14 Skin friction factor ( $C_f$ ) plotted as a function of the Reynolds number for 150 ppm solutions of PAM. Patel & Head (1969) data is shown as grey filled circles. Filled symbols represent long-duration data measurements and hollow symbols show time-resolved measurements.**

Figure 12(c) shows measurements of  $F_T$  versus  $Re$  for the 100 ppm PAM flows. Below the nominal  $Re$  of 2280, all flows are laminar with an  $F_T$  value of 0. For the nominal  $Re$  of 2280, the flows reflect laminar/turbulent intermittency with six repeated measurements having  $F_T$  values spanning from 0.10 to 0.85. At the nominal  $Re$  of 3310, the flows remain highly intermittent, with values of  $F_T$  between 0.26 to



0.92. Increasing nominal  $Re$  to 4570, the 100ppm PAM flows reflect less intermittency with  $F_T$  between 0.60 and 1.0, and a bias towards being more turbulent. Overall, the 100 ppm PAM solutions exhibit transitional flow patterns from  $Re$  of 2280 to 4570. Compared to Newtonian and low-concentration PAM solutions, the 100 ppm PAM solution transitions to turbulence at a much larger  $Re$  and demonstrates intermittency over a wider  $Re$  range.

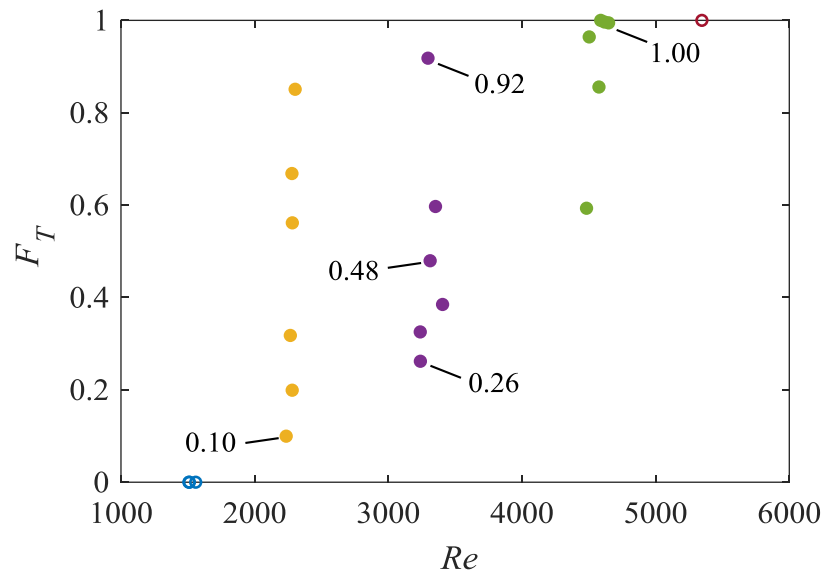


**Figure 4.15 The turbulent fraction ( $F_T$ ) for 100 ppm solutions of PAM is shown versus the Reynolds number. Colours show nominal  $Re$  same as Figure 4.13. Filled symbols represent long-duration data measurements and hollow symbols show time-resolved measurements. The velocity profiles for data points with annotated  $F_T$  will be illustrated.**

Values of  $F_T$  versus  $Re$  are shown in Figure 4.16 for the 150 ppm PAM flows. Below the nominal  $Re$  of 2810, all flows have  $F_T$  of zero and are laminar. At the

nominal  $Re$  of 3670 the flow field becomes intermittent with six repeated measurements having  $F_T$  values ranging from 0.15 to 0.67. Increasing the  $Re$  to 4640, values of  $F_T$  still show significant laminar-turbulent intermittency with values of  $F_T$  that range from 0.11 to 0.86. Finally, at the highest  $Re$  of 5370 the flow field becomes fully chaotic and the  $F_T$  is 1.0. Results of the 100 ppm and 150 ppm PAM flows demonstrate that the critical  $Re$  is larger for high-concentration PAM solutions compared to Newtonian fluids and low-concentration PAM solutions. Also, the range of  $Re$  that exhibit intermittency extends as the PAM concentration is increased. The transitional  $Re$  band (the difference between highest  $Re$  with  $F_T = 0$  and lowest  $Re$  with  $F_T = 1$ ) for 100 ppm solution is observed to be 2465 and for 150 ppm is 2500.

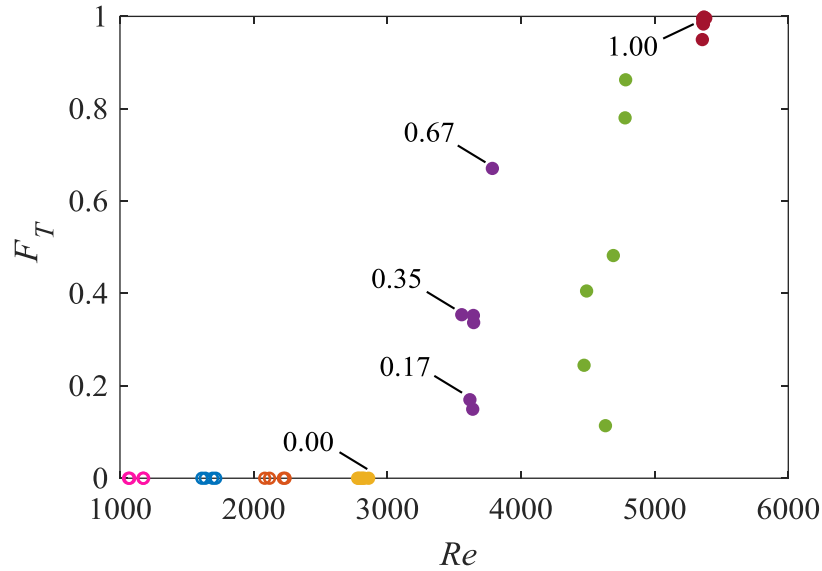


**Figure 4.16** The turbulent fraction ( $F_T$ ) for 150 ppm solutions of PAM is shown versus the Reynolds number. Colours show nominal  $Re$  same as Figure 4.14. Filled symbols represent long-duration data measurements and hollow symbols show time-resolved measurements. The velocity profiles for data points with annotated  $F_T$  will be illustrated.

Figure 4.17 shows  $U/\langle U_c \rangle$  with respect to  $t'$  along the streamwise-wall-normal plane for the high-concentration PAM flows. Figure 4.17(a) demonstrates  $U/\langle U_c \rangle$  for the laminar flow of PAM with  $c = 150$  ppm and  $Re = 2800$ . The flow is visually steady with no apparent chaos. By employing equation (3), the turbulence intensity TI along  $y = 0$  in the flow depicted in Figure 4.17(a) is calculated to be 2.5%. This value is comparable to the measurements of TI for channel flow just prior to transition conducted by Durst *et al.* (1998). Figure 4.17(b) shows  $U/\langle U_c \rangle$  for PAM with  $c = 150$  ppm,  $Re = 3650$  and  $F_T = 0.27$ . Instabilities can be seen in the flow close to the wall

region. These instabilities did not successfully reach the channel centerline, except during the instance when  $t'$  was between 200 and 250. Shekar *et al.* (2020, 2021) conducted direct numerical simulations of 2D channel flow and observed the relationship between the Tollmien-Schlichting (TS) attractor and elasto-inertial turbulence (EIT) in a dilute polymer solution. They found that the transition between the two states is directly tied to the strength of the TS critical layer fluctuations and can be attributed to a coil-stretch transition. These near-wall TS-like instabilities are not observed in pipe or plane Couette flow and have just been observed in 2D channel flow. The near-wall instabilities observed in figure Figure 4.17(b) might be attributed to these TS-like instability sheets.

In Figure 4.17(c) with  $F_T = 0.54$  and  $Re = 3800$ , the near wall instabilities penetrate to the channel centerline at several  $t'$  values of approximately 40, 180, 250 and 280. Figure 4.17(d) demonstrates the contours of  $U/\langle U_c \rangle$  for the 150 ppm PAM flow with  $Re = 4800$  and an  $F_T$  of 0.74. Multiple chaotic turbulent patches are visible between  $t'$  of 40-100, 150-175, 200-375 and 450-485. Lastly, Figure 4.17(e) shows the 150 ppm PAM flow with a  $Re$  of 5360 and a  $F_T$  of 1. The flow is visually chaotic along all values of  $y$  and  $t'$ . Figure 4.17 demonstrates the transition process in high-concentration PAM.

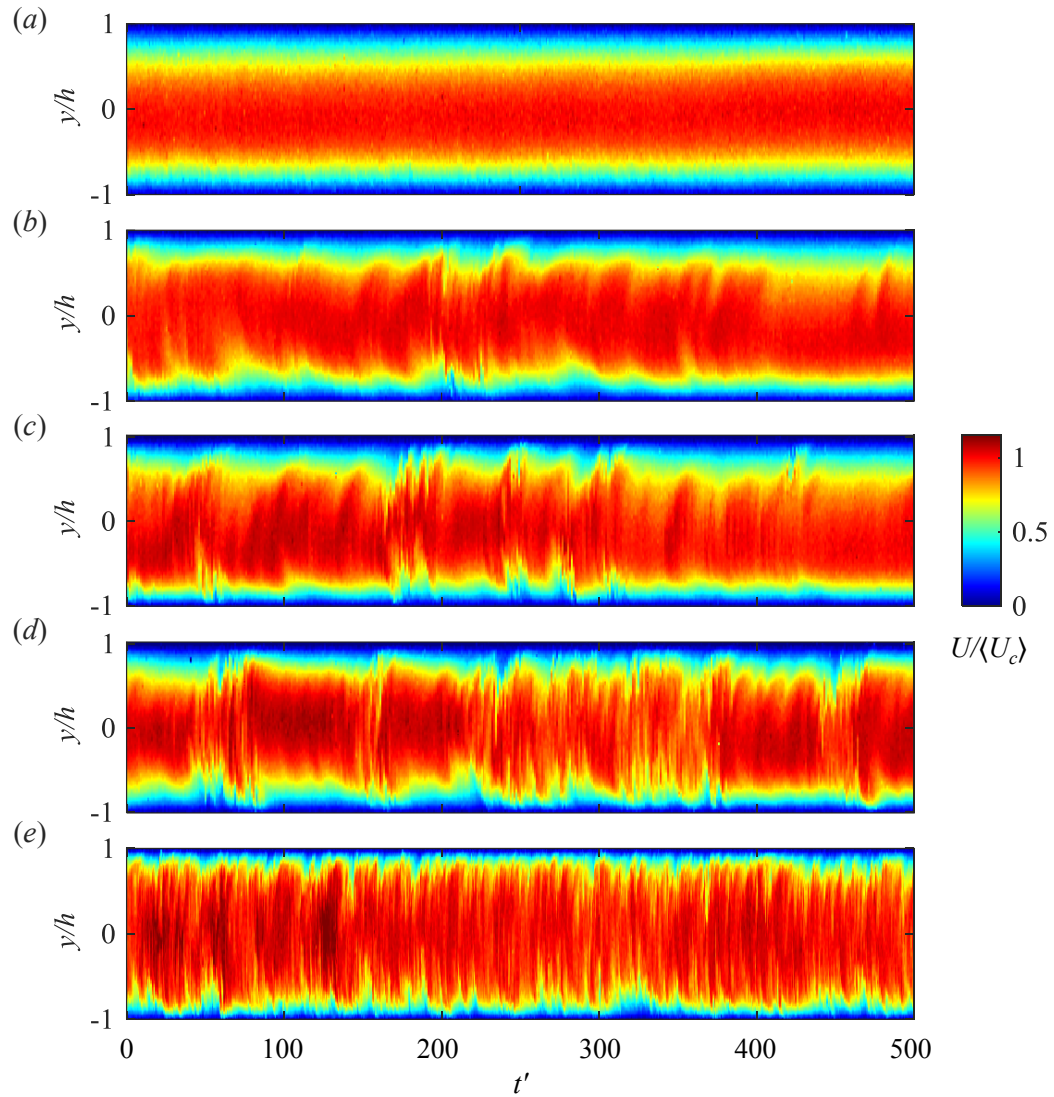


**Figure 4.17 Spatial contours of normalized streamwise velocity ( $U/U_c$ ) from streamwise wall-normal measurements showing various flow states for 150 ppm PAM solution. (a) Laminar  $F_T = 0$ ,  $Re = 2800$ , (b) transitional  $F_T = 0.27$ ,  $Re = 3650$ , (c) transitional  $F_T = 0.54$ ,  $Re = 3800$ , (d) transitional  $F_T = 0.74$ ,  $Re = 4800$  (e) turbulent  $F_T = 1$ ,  $Re = 5360$ .**

Figure 4.18 shows the measurements of  $U/\langle U_c \rangle$  along the streamwise-spanwise plan with respect to  $t'$  for the high-concentration PAM solution with  $c = 150$  ppm. Figure 4.18(a) corresponds to the lowest valve setting with a nominal  $Re$  of 2810 and demonstrates a laminar flow with very small fluctuations. Figure 4.18(b) to (d) displays  $U/\langle U_c \rangle$  for a transitional flow of the high-concentration PAM solution at nominal  $Re \approx 3670$ . Figure 4.18(b) illustrates a long low-speed streak at  $z/h$  of approximately 1. However, in contrast to Newtonian and low-concentration flows, the low-speed streak is not attached to any turbulent spot. Figure 4.18(c) depicts two low-speed streaks at approximate  $z/h$  of 0 and 2. It could be clearly seen that these streaks are not attached to any turbulent spots. Figure 4.18(d) shows a long low-speed streak at  $z/h$  of approximately 0 and extended along the entire domain of  $t'$ . At the transitional  $Re$ , no recognizable turbulent spots are observed, unlike the water and lower concentration PAM flows. Instead, only low-speed streaks, confined to a limited spanwise distance, can be seen in the transitional regime. Previously, Xi & Graham (2012) noted in their numerical simulations of channel flow that the transitional state existing between laminar and turbulent flow exhibited minimal three-dimensional qualities. This lack of three-dimensionality was also evident in the lower-branch exact coherent states near the laminar-turbulent boundary identified by Wang *et al.* (2007). However, prior to our study, no experimental flow visualizations had captured these streamwise transitional streaks.

Figure 4.18(e) illustrates the chaotic state of the flow for the high-concentration PAM solution at  $Re$  of 4640. The chaos and mixing in the  $z$ -axis direction are observed

to be less dominant compared to water and low-concentration solutions, seen in Figure 4.4 and Figure 4.11. The flow fields illustrated in Figure 4.18(b) and (c) have smaller velocity fluctuations in the streamwise-spanwise plane relative to Newtonian and low-concentration PAM conditions. Turbulent spots, which were present in the water and low-concentration cases, were absent in the high-concentration experiments in a similar form.

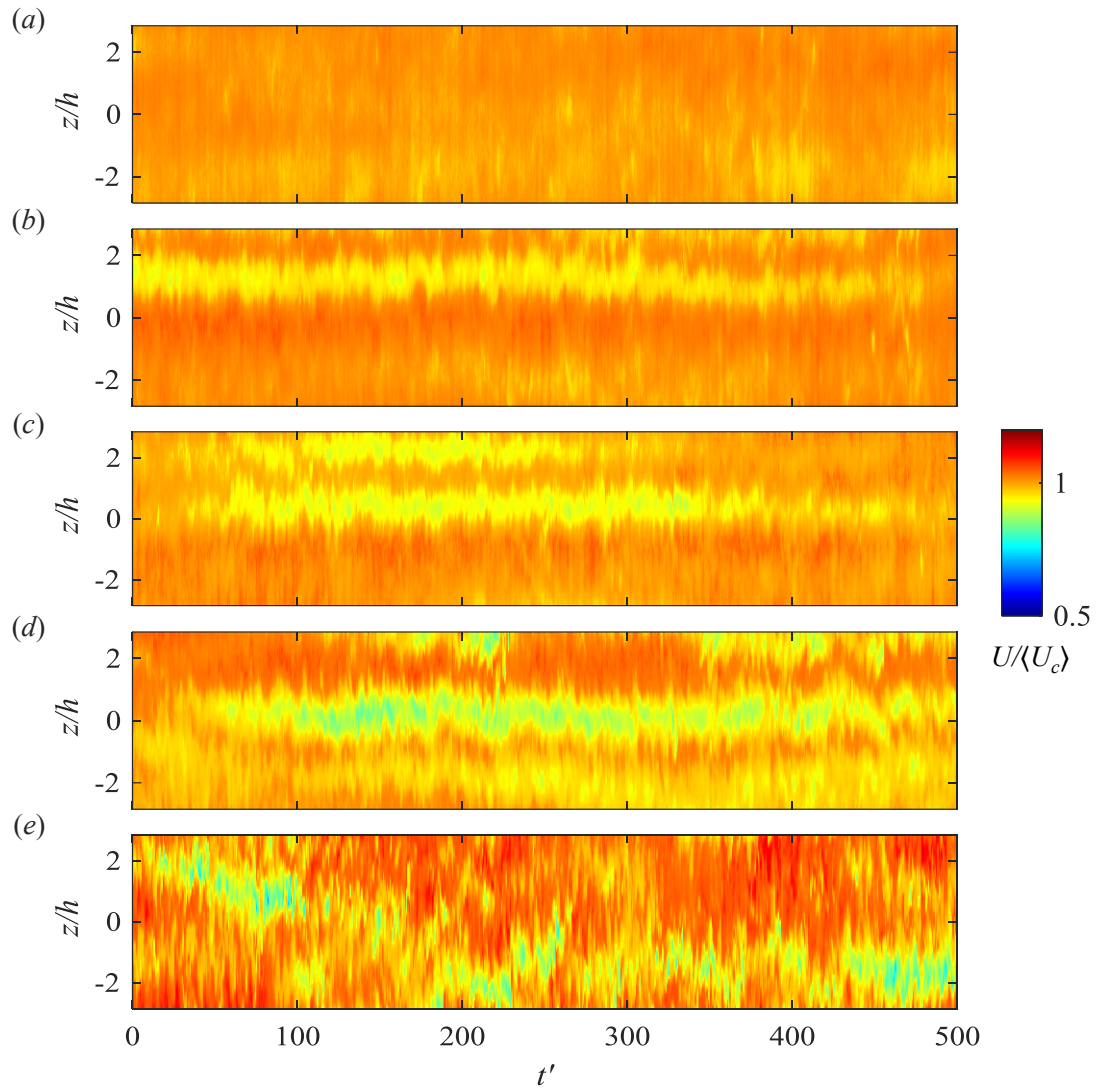


**Figure 4.18 Spatial contours of normalized streamwise velocity ( $U/\langle U_c \rangle$ ) from streamwise spanwise measurements showing (a) laminar  $Re \approx 2810$ , (b) to (d) three transitional cases  $Re \approx 3670$  and (e) turbulent  $Re \approx 4640$  flow fields in 150 ppm solution.**

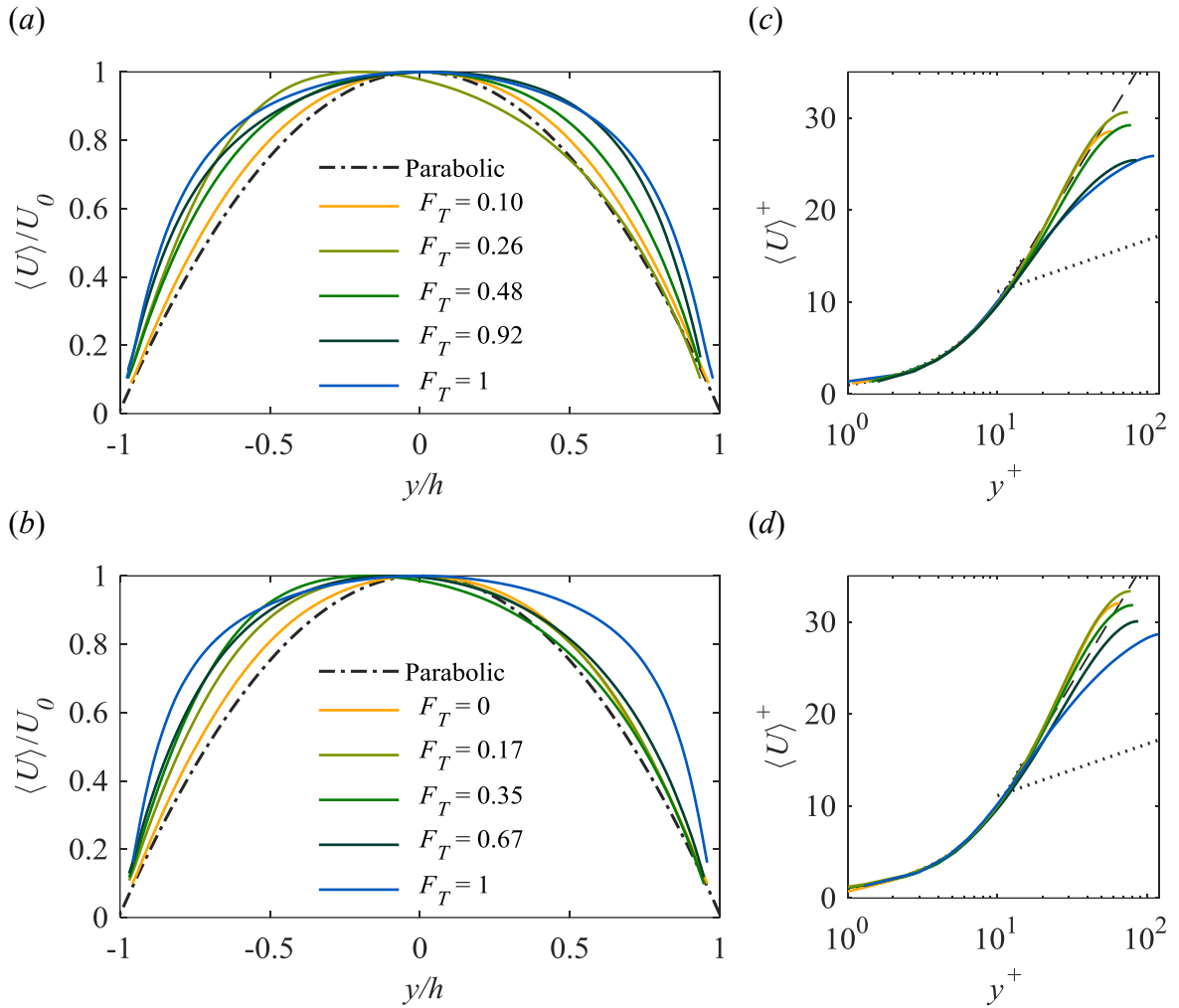


Figure 4.19 shows the velocity profiles acquired for the high-concentration solutions in outer- and inner-scaling. Comparing Figure 4.19(a), (c) to Figure 4.5(a) reveals that the laminar velocity profile deviated from the expected parabolic trend. The deviation is present in low-concentration solutions as well, however, it increases by increasing  $c$ . This deviation can be attributed to shear-thinning behaviour in the fluid, causing reduced viscous forces near the channel wall, and as a result a flattened velocity profile (Bird *et al.* 2006). Furthermore, the asymmetry in transitional velocity profiles are also observed in the data for high-concentration fluids, as it is shown in figures 15(a) and (b).

When examining the deviation from the Newtonian logarithmic law of the wall, it was found that the largest deviation occurred in the high-concentration cases, as seen in Figure 4.5(c) and (d). One can notice that for  $F_T$  less than 0.5 in high-concentration solutions, an occasional surpassing of Virk's (1970) velocity profile is observed. This surpassing was previously observed in several investigations (Dubief *et al.* 2005; Escudier *et al.* 2009; Li *et al.* 2006; Ptasinski *et al.* 2001). Possible justifications include shear-thinning and polymer aggregation in experimental studies, as well as the use of different artificial stress diffusion schemes in computational studies. Additionally, the validity of Virk's (1970) velocity profile may be incomplete. However, almost all observations fall within the 95% confidence range of the original linear fit of the polymer data to a Prandtl-von Kármán law (Graham 2014). Moreover, Xi & Graham (2012) and Pereira *et al.* (2019) observed surpassing of Virk's (1970)

velocity profile during instances of marginalized weak turbulence in their flow fields, which could explain the surpassing observed in Figure 4.5(c) and (d).

Comparing Figure 4.5(c) and (d), the deviation from the log-law is higher in the 150 ppm concentration than in the 100 ppm case. Even though the deviation from the log law does decrease with an increase in  $F_T$ , even in the flow's fully chaotic state, the inner-scaled velocity profile is significantly different compared to the logarithmic law of the wall. Previously Virk (1971) suggested that the behaviour of the mean velocity distribution depends on the achieved drag reduction and is dynamically different from the Newtonian flow.



**Figure 4.19** The velocity profiles for laminar, transitional and turbulent cases for high-concentration PAM solution. (a) 100 ppm outer scaling, (b) 100 ppm inner scaling. Reynolds numbers in order of increasing  $F_T$ : 2240, 3240, 3315, 3300, 4590. (c) 150 ppm outer scaling and (d) 150 ppm inner scaling. Reynolds numbers in order of increasing  $F_T$ : 2860, 3620, 3560, 3790, 5360. Dotted lines show the viscous sublayer and logarithmic law of the wall; Virk's (1970) velocity profile is shown in a dashed line.

## 5. Discussion

This study investigated the effect of polymers on laminar-turbulent transition in channel flows. The  $C_f$  for low-concentration solutions of PAM with  $c$  of 50 ppm and 75 ppm, increased with growing  $Re$  until the onset of drag reduction. After which,  $C_f$  begins to reduce with increasing  $Re$ . At higher  $Re$ , values of  $C_f$  are reduced to values close to the MDR asymptote. Since drag reduction shows an onset point, the low-concentration experiments showed a type A drag reduction behaviour. The  $C_f$  data obtained from high-concentration solutions (100 ppm and 150 ppm) exhibit a laminar trend up to a higher Reynolds number, after which they deviate and approach the MDR asymptote, indicative of type B drag reduction. Previous research by Mohsenipour *et al.* (2013) reported a similar shift in the drag reduction behaviour with an increase in concentration in their pipe experiments.

Comparing the measurements of the turbulent fraction  $F_T$  for water and the PAM flows showed that the transition to turbulence was delayed to larger  $Re$  in the polymeric flows, with the delay increasing as the polymer concentration increased.

These results are in line with previous literature that has shown that flexible polymers can suppress Newtonian turbulence and delay the laminar-turbulent transition. Early work by Giles & Pettit (1967) observed that increasing polymer concentration monotonically increased the critical Reynolds number required for transition. Compared to a value of 2240 for pure water, their highest polymer concentration solution delayed transition until a Reynolds number of 26,000. Further research quantified the underlying mechanisms for this transition delay. Pinho & Whitelaw (1990) attributed the effect to shear-thinning and suppression of turbulent fluctuations in normal stress components. Draad *et al.* (1998) found polymers stabilize the flow with respect to forced disturbances, increasing the critical disturbance velocity compared to water. However, they noted this delay occurred only for fresh, extended polymer chains. While not evident from friction factor plots, Escudier *et al.* (1998) used axial velocity fluctuation intensity to clearly identify delayed transition with increasing polymer elasticity and extensional viscosity. Finally, Samantha *et al.* (2013) systematically increased polymer concentration, finding puff survival rates shifted to progressively higher Reynolds numbers. The concentration dependence indicated polymers postpone turbulence onset in faster than a linear trend, quantifying the transition delay effect. However, it should be noted that all of the mentioned investigations were carried out in pipe flows. Hence, given our observation of transition delay, one can conclude that the underlying turbulence-suppressing mechanisms are present in channel flows as well.

In addition, the transition band – the range in  $Re$  where flows exhibited regions of laminar-turbulent intermittency and an  $F_T$  between 0 and 1 – also became wider as the polymer concentration increased. For high-concentration PAM flows within the transitional range of  $Re$ , the flows exhibit stronger instabilities in the zones between the turbulent spots, as observed in velocity measurements along the streamwise-wall-normal plane. This behaviour is in contrast to the behaviour of water and lower concentration PAM flows, where pronounced turbulent spots are observed with calm laminar regions in between them. Furthermore, the time variation of the centreline velocity observed in the streamwise-wall-normal plane were more gradual, consistent with the findings of Samanta *et al.* (2013), who reported that turbulent puffs could not be detected for polymer concentrations greater than 200 ppm. They reported that a different form of disordered motion sets in at a lower  $Re$ . However, it should be noted that Samanta *et al.* (2013) conducted their experiments in a pipe flow facility, and according to the comprehensive review by Castillo Sánchez *et al.* (2022), the instabilities and pathway to turbulence and MDR could differ in channel and pipe flows. In the streamwise-spanwise measurements of high-concentration solutions, long low-speed streamwise streaks are observed within the transitional Reynolds number range. Since no turbulent spots were observed in the streamwise-spanwise measurements of high-concentration solutions, these low-speed streaks may be alternative intermittent flow structures on the path from laminar to turbulent flow. Moreover, Lemoult *et al.* (2014) illustrated that the turbulent spots of channel flow evolve from a streaky structure. Connecting our observations with theirs suggests that

high polymer concentrations may interfere more noticeably with the process of turbulent spot growth in the spanwise direction.

Figure 5.1 displays the turbulence intensity TI percentage calculated along the centerline of the channel for all experiments. For intermittent cases where  $0.2 \leq Fr \leq 0.8$ , TI is calculated separately for the laminar and turbulent sections that are established using the detection method from section 2.2. The TI of the laminar portions is represented using hollow symbols, while the TI of the turbulent portion of the signal is shown using filled symbols in Figure 5.1. It is noteworthy that as  $Re$  increases in high-concentration cases, the two branches of laminar and turbulent intensity appear to converge. The reduction in the higher TI branch as  $Re$  increases can be attributed to two factors: First, an increase in the average centerline velocity due to an increase in flow rate. To assess the effect and importance of this factor, one can compare polymeric cases to higher  $Re$  Newtonian cases, as shown in Figure 5.1 with gray markers (both circles and stars). Although Newtonian flows exhibit a reduction in the higher branch of TI, the drop in TI values is more pronounced in polymeric solutions. The second reason for the decrease in the higher TI branch as a function of  $Re$  for polymeric cases is the reduced centerline velocity fluctuations associated with increasing solution concentration as observed in spatio-temporal contours. For the upper TI branch and at a constant  $Re$  range of 3000 to 3500, the TI values for 100 ppm solutions are generally lower than those for 75 ppm solutions. A similar trend is observed in the  $Re$  range of 4500 to 5000 for 100 ppm and 150 ppm cases.

In addition to the decrease in the upper branch of TI, an increase is also observed in the lower branch in Figure 5.1. The TI values increase from 0.75% for the water cases at  $Re = 1500$  to 1.17% for the 100 ppm cases at  $Re = 3650$  and 1.77% for the 150 ppm experiments at  $Re = 5365$ . This trend could represent the centerline instability underlying the high-concentration polymer cases. This instability is present in the laminar flow regions between turbulent spots, similar to the observation in Figure 4.17, which would result in larger centerline velocity fluctuations and consequently higher TI for these regions.

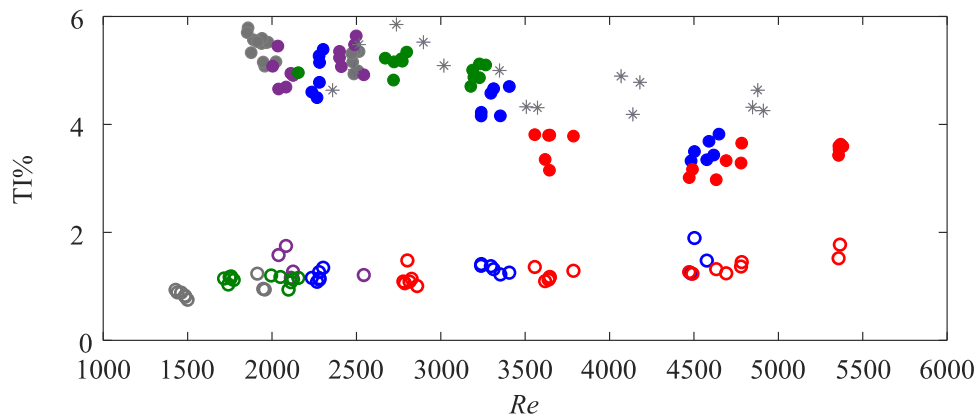


**Figure 5.1 Turbulence intensity (TI) calculated along the centerline of the channel. Hollow symbols represent laminar segments of flow and solid-filled symbols show turbulent parts. The symbol colours are similar to Figure 3.4 representing the polymer concentration. Gray markers represent water data, star symbols show time-resolved PIV measurements.**



Figure 5.2 presents data for all five solutions in Weissenberg number,  $Wi = \dot{\gamma} t_e$ , and  $Re$  space. Each data point is coloured according to the fraction of turbulence, which is indicated by the colour bar in the figure. The figure is divided into four zones, namely laminar, transitional, turbulent, and MDR based on  $F_T$  and  $C_f$  values. The MDR zone comprises all data points that are within 15% of the drag reduction of the MDR line in the  $C_f$ - $Re$  plots. It is important to note that the boundaries delineated in the figure are approximate, and there are uncertainties associated with the limited number of data points and rheology measurements. Similar but qualitative  $Wi$ - $Re$  phase diagrams have been presented in previous studies, such as Graham (2014), Xi (2019) and Castillo Sánchez *et al.* (2022). Also,  $Re$  versus polymer concentration maps have been shown in Choueiri *et al.* (2018) and Chandra *et al.* (2020) for pipe and microtube flows, respectively. A horizontal path on the  $Wi = 0$  line indicates the Newtonian laminar to turbulent transition. When polymers are introduced to the flow ( $Wi > 0$ ), the transitional region expands, and the expansion increases with increasing  $Wi$ . The transition to the  $F_T = 1$  region also occurs at a higher Reynolds number. Moreover, moving vertically with increasing  $Wi$  at a narrow range of  $Re$  reveals the reverse transition behaviour through the intermittent flow field. This is consistent with the observations made by Lopez *et al.* (2019) for pipe flow. Additionally, type B drag reduction behaviour and previous observations (Choueiri *et al.* 2018; Lopez *et al.* 2019; Samanta *et al.* 2013) suggests that for sufficiently high  $Wi$ , a fluid can transition directly from a laminar state to the MDR state with little to no intermittency forming the laminar-MDR zones boundary.

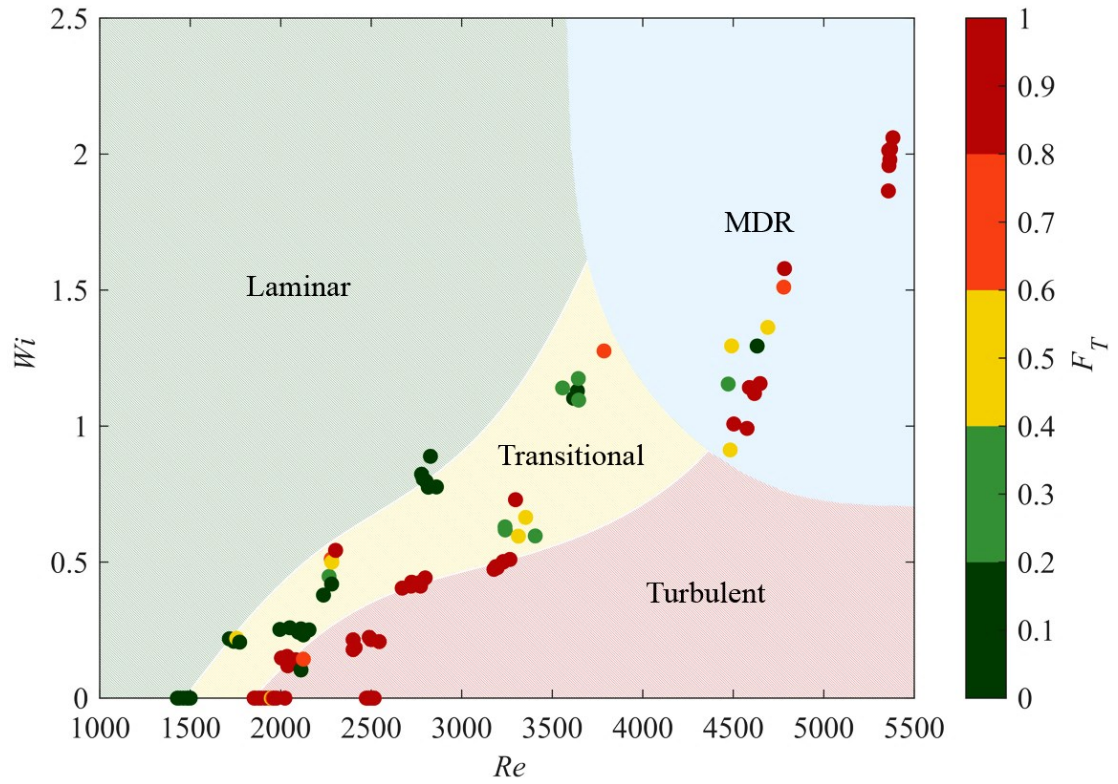


**Figure 5.2 Data for all five solutions in Weissenberg number and Reynolds number space, coloured by the fraction of turbulence as shown by the colour bar. Indicated “Laminar”, “Transitional”, “Turbulent”, and MDR zones have approximate boundaries.**

## 6. Conclusions

In this study, the flow characteristics of water, low (50 and 75 ppm) and high-concentration (100 and 150 ppm) solutions of polyacrylamide (PAM) in a rectangular channel flow facility were systematically investigated utilizing particle image velocimetry in streamwise-wall-normal and streamwise-spanwise planes. The skin friction coefficient ( $C_f$ ) and the fraction of turbulence ( $F_T$ ) were measured across a range of Reynolds numbers through extensive experimental campaigns. For transitional flows, measurements were repeated at least six times at each flow rate to ensure sufficient repeatability and reliability in quantifying the intermittent laminar-turbulent transitions. Velocity field measurements were conducted to characterize the Newtonian and polymeric flows in laminar, transitional, and fully turbulent regimes. This experimental study provides new insights into how dilute polymer additives influence the laminar-turbulent transition.

This experimental study provides new insights into how polymer additives influence the laminar-turbulent transition in rectangular channel flows. For the

baseline Newtonian fluid, the evolution of turbulence statistics and critical Reynolds number range of 1900-2200 aligned closely with previous literature, validating the experimental methods.

With the introduction of lower polymer concentrations, the transitional regime expanded substantially, with intermittency occurring from  $Re = 2000-3000$  compared to 1900-2200 in the Newtonian case. The onset of sustained turbulence was delayed to  $Re \geq 3000$ , compared to 2200 for the Newtonian fluid. The solutions exhibited a drag reduction onset point, following a type A pattern with rising skin friction during the laminar-turbulent transition, then clearly dropping friction above a threshold Reynolds number. Transitional flows displayed recognizable turbulent spots and asymmetric mean velocity profiles, analogous to Newtonian transition.

In contrast, higher polymer concentrations demonstrated significant differences. Most notably, they showed a departure from the laminar skin friction trend toward the maximum drag reduction asymptote, consistent with type B drag reduction behaviour. The polymers strongly hindered the emergence and spreading of turbulent spots during the transition. Instead, elongated streamwise streaks dominated the transitional flows at higher concentrations for  $Re$  from 3000-5000.

Polymer flows at all concentrations exhibited enhanced centerline velocity fluctuations with turbulence intensity increasing from 0.75% to 1.77% in laminar zones between turbulent events. However, velocity fluctuations decreased significantly in fully turbulent regions, dropping from 5% in Newtonian flows to 3% in high-concentration polymer solutions.

## 6.1 Future Work

While this thesis provides new insights into the laminar-turbulent transition and turbulence modulation induced by dilute polymer solutions, opportunities remain to further expand the understanding of viscoelastic turbulence dynamics.

Advanced optical measurements and computational fluid dynamics simulations would enable more in-depth investigations of the polymer-modified coherent structures and instability mechanisms governing the transition from laminar to turbulent flow. For example, techniques such as tomographic particle image velocimetry could capture detailed velocity statistics and turbulence quantities within the transitional flow structures. Direct numerical simulations, if properly formulated and validated, may shed light on the polymer stretching dynamics and internal stress balances underlying the formation transitional flow structures.

Exploring the impacts of complex geometries and flow configurations beyond canonical flows merits study as well. The transitional statistics and coherence structures could differ substantially in non-rectangular ducts, flows over curved surfaces, or flows with swirl and rotation.

The range of fluid elasticity and extensibility could be expanded by testing solutions of flexible polymer species beyond polyacrylamide. Varying polymer molecular weight and chain branching may induce further alterations to the transition process and sustainment of chaotic motions. Ultimately, the goal is to develop comprehensive predictive capabilities - to quantitatively determine critical stability

parameters and define transition criteria encompassing an extensive range of viscoelastic fluid properties.

Overall, the foundations established in this thesis will motivate and inform extensive future work unraveling the intricacies of instabilities in non-Newtonian flows. This will provide deeper insights into polymer-turbulent interactions, which may reveal more about the mechanisms underlying drag reduction.

## Bibliography

- Alavyoon, F., Henningson, D. S., & Alfredsson, P. H. (1986). Turbulent spots in plane Poiseuille flow—flow visualization. *Physics of Fluids*, **29**(4), 1328.
- Avila, K., Moxey, D., De Lozar, A., Avila, M., Barkley, D., & Hof, B. (2011). The onset of turbulence in pipe flow. *Science*, **333**(6039), 192–196.
- Bark, F. H., & Tinoco, H. (1978). Stability of plane Poiseuille flow of a dilute suspension of slender fibres. *Journal of Fluid Mechanics*, **87**(2), 321–333.
- Barkley, D., Song, B., Mukund, V., Lemoult, G., Avila, M., & Hof, B. (2015). The rise of fully turbulent flow. *Nature*, **526**(7574), 550–553.
- Bird, R. B., Stewart, W. E., & Lightfoot, E. N. (2006). *Transport Phenomena*, Wiley.
- Carlson, D. R., Widnall, S. E., & Peeters, M. F. (1982). A flow-visualization study of transition in plane Poiseuille flow. *Journal of Fluid Mechanics*, **121**(1), 487.
- Castillo Sánchez, H. A., Jovanović, M. R., Kumar, S., ... Wilson, H. J. (2022). Understanding viscoelastic flow instabilities: Oldroyd-B and beyond. *Journal of Non-Newtonian Fluid Mechanics*, **302**, 104742.
- Castro, W., & Squire, W. (1968). The effect of polymer additives on transition in pipe flow. *Applied Scientific Research*, **18**(1), 81–96.
- Chandra, B., Shankar, V., & Das, D. (2018). Onset of transition in the flow of polymer solutions through microtubes. *Journal of Fluid Mechanics*, **844**, 1052–1083.
- Chandra, B., Shankar, V., & Das, D. (2020). Early transition, relaminarization and drag reduction in the flow of polymer solutions through microtubes. *Journal of Fluid Mechanics*, **885**, A47.
- Choueiri, G. H., Lopez, J. M., & Hof, B. (2018). Exceeding the asymptotic limit of polymer

- drag reduction. *Physical Review Letters*, **120**(12), 124501.
- Corrsin, S. (1943). *Investigation of flow in an axially symmetrical heated jet of air*, Pasadena.
- Dean, R. B. (1978). Reynolds number dependence of skin friction and other bulk flow variables in two-dimensional rectangular duct flow. *Journal of Fluids Engineering*, **100**(2), 215–223.
- Delshad, M., Kim, D. H., Magbagbeola, O. A., Huh, C., Pope, G. A., & Tarahhom, F. (2008). Mechanistic interpretation and utilization of viscoelastic behavior of polymer solutions for improved polymer-flood efficiency. In *All Days*, SPE. doi:10.2118/113620-MS
- Draad, A. A., Kuiken, G. D. C., & Nieuwstadt, F. T. M. (1998). Laminar-turbulent transition in pipe flow for Newtonian and non-Newtonian fluids. *Journal of Fluid Mechanics*, **377**, 267–312.
- Dubief, Y., Terrapon, V. E., & Soria, J. (2013). On the mechanism of elasto-inertial turbulence. *Physics of Fluids*, **25**(11). doi:10.1063/1.4820142
- Dubief, Y., Terrapon, V. E., White, C. M., Shaqfeh, E. S. G., Moin, P., & Lele, S. K. (2005). New answers on the interaction between polymers and vortices in turbulent flows. *Flow, Turbulence and Combustion Formerly: Applied Scientific Research*, **74**(4), 311–329.
- Durst, F., Fischer, M., Jovanovic', J., & Kikura, H. (1998). Methods to set up and investigate low Reynolds number, fully developed turbulent plane channel flows. *Journal of Fluids Engineering*, **120**(3), 496–503.
- Eckhardt, B., Marzinzik, K., & Schmiegel, A. (1998). Transition to turbulence in shear flows. In *A Perspective Look at Nonlinear Media*, Berlin, Heidelberg: Springer Berlin Heidelberg, pp. 327–338.
- Elsnab, J., Klewicki, J., Maynes, D., & Ameel, T. (2011). Mean dynamics of transitional channel flow. *Journal of Fluid Mechanics*, **678**, 451–481.



- Emmons, H. W. (1951). The laminar-turbulent transition in a boundary layer-part I. *Journal of the Aeronautical Sciences*, **18**(7), 490–498.
- Escudier, M. P., Nickson, A. K., & Poole, R. J. (2009). Turbulent flow of viscoelastic shear-thinning liquids through a rectangular duct: Quantification of turbulence anisotropy. *Journal of Non-Newtonian Fluid Mechanics*, **160**(1), 2–10.
- Escudier, M. P., Presti, F., & Smith, S. (1998). Drag reduction in the turbulent pipe flow of polymers. *Journal of Non-Newtonian Fluid Mechanics*, **81**(3). doi:10.1016/S0377-0257(98)00098-6
- Forame, P. C., Hansen, R. J., & Little, R. C. (1972). Observations of early turbulence in the pipe flow of drag reducing polymer solutions. *AIChE Journal*, **18**(1), 213–217.
- Giles, W. B., & Pettit, W. T. (1967, November 1). Stability of dilute viscoelastic flows. *Nature*, pp. 470–472.
- Graham, M. D. (2014). Drag reduction and the dynamics of turbulence in simple and complex fluids. *Physics of Fluids*, **26**(10), 101301.
- Hansen, R. J., & Little, R. C. (1974). Early turbulence and drag reduction phenomena in larger pipes. *Nature*, **252**(5485). doi:10.1038/252690a0
- Hansen, R. J., Little, R. C., Reischman, M. M., & Kelleher, M. D. (1974). Stability and the laminar-to-turbulent transition in pipe flows of drag reducing polymer solutions, ((September 4-6, 1974)).
- Henningson, D. S., & Kim, J. (1991). On turbulent spots in plane Poiseuille flow. *Journal of Fluid Mechanics Digital Archive*, **228**, 183.
- Hoyt, J. W. (1977). Laminar-turbulent transition in polymer solutions. *Nature*, **270**(5637), 508–509.
- Iida, O., & Nagano, Y. (1998). The relaminarization mechanisms of turbulent channel flow

- at low Reynolds numbers. *Flow, Turbulence and Combustion*, **60**(2), 193–213.
- Iwamoto, K., Suzuki, Y., & Kasagi, N. (2002). Reynolds number effect on wall turbulence: toward effective feedback control. *International Journal of Heat and Fluid Flow*, **23**(5), 678–689.
- Jones, O. C. (1976). An improvement in the calculation of turbulent friction in rectangular ducts. *Journal of Fluids Engineering*, **98**(2), 173–180.
- Krishnan Thota Radhakrishnan, A., Poelma, C., van Lier, J., & Clemens, F. (2021). Laminar-turbulent transition of a non-Newtonian fluid flow. *Journal of Hydraulic Research*, **59**(2), 235–249.
- Lemoult, G., Gumowski, K., Aider, J.-L., & Wesfreid, J. E. (2014). Turbulent spots in channel flow: An experimental study. *The European Physical Journal E*, **37**(4), 25.
- Li, C. F., Gupta, V. K., Sureshkumar, R., & Khomami, B. (2006). Turbulent channel flow of dilute polymeric solutions: Drag reduction scaling and an eddy viscosity model. *Journal of Non-Newtonian Fluid Mechanics*, **139**(3), 177–189.
- Lindgren, E. R. (1957). The transition process and other phenomena in viscous flow. *Arkiv Fysik*, **12**.
- Lopez, J. M., Choueiri, G. H., & Hof, B. (2019). Dynamics of viscoelastic pipe flow at low Reynolds numbers in the maximum drag reduction limit. *Journal of Fluid Mechanics*, **874**, 699–719.
- Manneville, P. (2016). Transition to turbulence in wall-bounded flows: Where do we stand? *Mechanical Engineering Reviews*, **3**(2), 15-00684-15-00684.
- Marshall, R. J., & Metzner, A. B. (1967). Flow of viscoelastic fluids through porous media. *Industrial & Engineering Chemistry Fundamentals*, **6**(3), 393–400.
- Mohsenipour, A. A., Pal, R., & Prajapati, K. (2013). Effect of cationic surfactant addition on

- the drag reduction behaviour of anionic polymer solutions. *The Canadian Journal of Chemical Engineering*, **91**(1), 181–189.
- Narayanan, M. A. B., & Narayana, T. (1967). Some studies on transition from laminar to turbulent flow in a two-dimensional channel. *Zeitschrift Für Angewandte Mathematik Und Physik ZAMP*, **18**(5), 642–650.
- Natori, T., Watanabe, K., Aoki, D., Seki, D., & Matsubara, M. (2011). Flow visualization in a relaminarizing channel flow. In *Proceedings of the 2011 Annual Meeting*, Shinetsu: Japan Society of FluidMechanics, pp. 75–76.
- Okumura, T., & Matsubara, M. (2006). Experimental study on minimal Reynolds number with LDV measurement and visualization. In *Proceedings of the 2006 Annual Meeting*, Japan Society of Fluid Mechanics, p. 42.
- Orszag, S. A. (1971). Accurate solution of the Orr–Sommerfeld stability equation. *Journal of Fluid Mechanics*, **50**(4), 689–703.
- Orszag, S. A., & Kells, L. C. (1980). Transition to turbulence in plane Poiseuille and plane Couette flow. *Journal of Fluid Mechanics*, **96**(01), 159.
- Pan, L., Morozov, A., Wagner, C., & Arratia, P. E. (2013). Nonlinear elastic instability in channel flows at low reynolds numbers. *Physical Review Letters*, **110**(17), 1–5.
- Patel, V. C., & Head, M. R. (1969). Some observations on skin friction and velocity profiles in fully developed pipe and channel flows. *Journal of Fluid Mechanics*, **38**(1), 181–201.
- Pereira, A. S., Thompson, R. L., & Mompean, G. (2019). Common features between the Newtonian laminar–turbulent transition and the viscoelastic drag-reducing turbulence. *Journal of Fluid Mechanics*, **877**, 405–428.
- Pinho, F. T., & Whitelaw, J. H. (1990). Flow of non-newtonian fluids in a pipe. *Journal of Non-Newtonian Fluid Mechanics*, **34**(2), 129–144.

- Poole, R. J. (2016). Elastic instabilities in parallel shear flows of a viscoelastic shear-thinning liquid. *Physical Review Fluids*, **1**(4). doi:10.1103/PhysRevFluids.1.041301
- Porteous, K. C., & Denn, M. M. (1972a). Linear stability of plane Poiseuille flow of viscoelastic liquids. *Transactions of the Society of Rheology*, **16**(2), 295–308.
- Porteous, K. C., & Denn, M. M. (1972b). Nonlinear stability of plane Poiseuille flow of viscoelastic liquids. *Transactions of the Society of Rheology*, **16**(2), 309–319.
- Ptasinski, P. K., Nieuwstadt, F. T. M., Van Den Brule, B. H. A. A., & Hulsen, M. A. (2001). Experiments in turbulent pipe flow with polymer additives at maximum drag reduction. *Flow, Turbulence and Combustion*, **66**(2), 159–182.
- Qin, B., & Arratia, P. E. (2017). Characterizing elastic turbulence in channel flows at low Reynolds number. *Physical Review Fluids*, **2**(8), 1–9.
- Raffel, M., Willert, C. E., Scarano, F., Kähler, C. J., Wereley, S. T., & Kompenhans, J. (2018). Particle image velocimetry: A practical guide. In *Particle Image Velocimetry: A Practical Guide*, pp. 1–32.
- Ram, A., & Tamir, A. (1964). Structural turbulence in polymer solutions. *Journal of Applied Polymer Science*, **8**(6), 2751–2762.
- Reynolds, O. (1883). XXIX. An experimental investigation of the circumstances which determine whether the motion of water shall be direct or sinuous, and of the law of resistance in parallel channels. *Philosophical Transactions of the Royal Society of London*, **174**, 935–982.
- Rotta, J. (1956). Experimenteller beitrag zur entstehung turbulenter strömung im rohr. *Ingenieur-Archiv*, **24**(4), 258–281.
- Samanta, D., Dubief, Y., Holzner, M., ... Hof, B. (2013). Elasto-inertial turbulence. *Proceedings of the National Academy of Sciences*, **110**(26), 10557–10562.

- Sano, M., & Tamai, K. (2016). A universal transition to turbulence in channel flow. *Nature Physics*, **12**(3), 249–253.
- Schröder, A., Geisler, R., Elsinga, G. E., Scarano, F., & Dierksheide, U. (2008). Investigation of a turbulent spot and a tripped turbulent boundary layer flow using time-resolved tomographic PIV. *Experiments in Fluids*, **44**(2), 305–316.
- Sciacchitano, A. (2019). Uncertainty quantification in particle image velocimetry. *Measurement Science and Technology*, **30**(9), 092001.
- Seki, D., & Matsubara, M. (2012). Experimental investigation of relaminarizing and transitional channel flows. *Physics of Fluids*, **24**(12), 124102.
- Shekar, A. (2021). *Structures and mechanisms in elastoinertial turbulence*, University of Wisconsin-Madison.
- Shekar, A., McMullen, R. M., McKeon, B. J., & Graham, M. D. (2020). Self-sustained elastoinertial Tollmien-Schlichting waves. *Journal of Fluid Mechanics*, **897**. doi:10.1017/jfm.2020.372
- Shekar, A., McMullen, R. M., McKeon, B. J., & Graham, M. D. (2021). Tollmien-Schlichting route to elastoinertial turbulence in channel flow. *Physical Review Fluids*, **6**(9), 093301.
- Sid, S., Terrapon, V. E., & Dubief, Y. (2018). Two-dimensional dynamics of elasto-inertial turbulence and its role in polymer drag reduction. *Physical Review Fluids*, **3**(1). doi:10.1103/PhysRevFluids.3.011301
- Srinivas, S. S., & Kumaran, V. (2017). Effect of viscoelasticity on the soft-wall transition and turbulence in a microchannel. *Journal of Fluid Mechanics*, **812**, 1076–1118.
- Terrapon, V. E., Dubief, Y., & Soria, J. (2015). On the role of pressure in elasto-inertial turbulence. *Journal of Turbulence*, **16**(1). doi:10.1080/14685248.2014.952430
- Toms, B. A. (1948). Some observations on the flow of linear polymer solutions through

- straight tubes at large Reynolds numbers. *Proceedings of the 1st International Congress on Rheology*, **2**, 135–141.
- Toms, B. A. (1977). On the early experiments on drag reduction by polymers. *Physics of Fluids*. doi:10.1063/1.861757
- Virk, P. S. (1971). An elastic sublayer model for drag reduction by dilute solutions of linear macromolecules. *Journal of Fluid Mechanics*, **45**(3), 417–440.
- Virk, P. S. (1975). Drag reduction fundamentals. *AIChE Journal*, **21**(4), 625–656.
- Virk, P. S., Mickley, H. S., & Smith, K. A. (1970). The ultimate asymptote and mean flow structure in Toms' phenomenon. *Journal of Applied Mechanics*, **37**(2), 488–493.
- Virk, P. S., Sherman, D. C., & Wagger, D. L. (1997). Additive equivalence during turbulent drag reduction. *AIChE Journal*, **43**(12), 3257–3259.
- Virk, P. S., & Wagger, D. L. (1990). Aspects of mechanisms in type B drag reduction. In *Structure of Turbulence and Drag Reduction*, Berlin, Heidelberg: Springer Berlin Heidelberg, pp. 201–213.
- Wang, J., Gibson, J., & Waleffe, F. (2007). Lower branch coherent states in shear flows: transition and control. *Physical Review Letters*, **98**(20), 204501.
- Wang, S. N., Shekar, A., & Graham, M. D. (2017). Spatiotemporal dynamics of viscoelastic turbulence in transitional channel flow. *Journal of Non-Newtonian Fluid Mechanics*, **244**, 104–122.
- White, C. M., Dubief, Y., & Klewicki, J. (2012). Re-examining the logarithmic dependence of the mean velocity distribution in polymer drag reduced wall-bounded flow. *Physics of Fluids*, **24**(2), 021701.
- White, C. M., & Mungal, M. G. (2008). Mechanics and prediction of turbulent drag reduction with polymer additives. *Annual Review of Fluid Mechanics*, **40**(1), 235–256.

- White, W. D., & McEligot, D. M. (1970). Transition of mixtures of polymers in a dilute aqueous solution. *Journal of Basic Engineering*, **92**(3), 411–418.
- Wu, X. (2023). New insights into turbulent spots. *Annual Review of Fluid Mechanics*, **55**(1), 45–75.
- Wynanski, I. J., & Champagne, F. H. (1973). On transition in a pipe. Part 1. The origin of puffs and slugs and the flow in a turbulent slug. *Journal of Fluid Mechanics*, **59**(2), 281–335.
- Wynanski, I., Sokolov, M., & Friedman, D. (1975). On transition in a pipe. Part 2. The equilibrium puff. *Journal of Fluid Mechanics*, **69**(2), 283–304.
- Xi, L. (2019). Turbulent drag reduction by polymer additives: Fundamentals and recent advances. *Physics of Fluids*, **31**(12), 121302.
- Xi, L., & Graham, M. D. (2010). Active and hibernating turbulence in minimal channel flow of newtonian and polymeric fluids. *Physical Review Letters*, **104**(21), 15–18.
- Xi, L., & Graham, M. D. (2012). Dynamics on the laminar-turbulent boundary and the origin of the maximum drag reduction asymptote. *Physical Review Letters*, **108**(2), 028301.
- Yimprasert, S., Kvik, M., Alfredsson, P. H., & Matsubara, M. (2021). Flow visualization and skin friction determination in transitional channel flow. *Experiments in Fluids*, **62**(2), 31.
- Zakin, J. L., Ni, C. C., Hansen, R. J., & Reischman, M. M. (1977). Laser Doppler velocimetry studies of early turbulence. *Physics of Fluids*, **20**(10), S85.

# Appendices

## A MATLAB Code for Laminar/Turbulent Detection

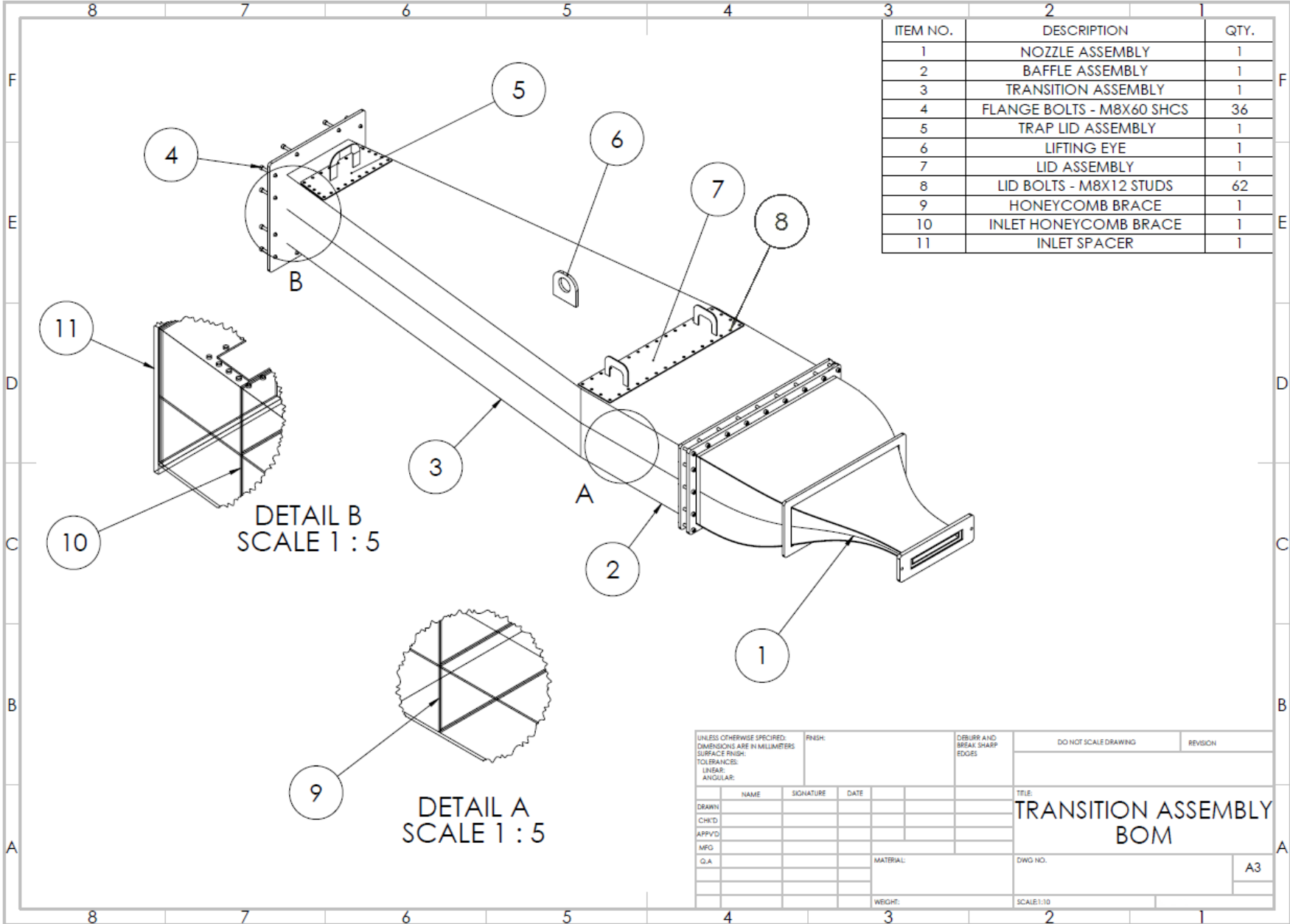
```
1 %% Laminar/turbulent detection algorithm
2 % Load velocity data
3 % U_signal = loaded velocity data
4
5 %% Measurement parameters
6 f = 60; % Acquisition frequency (Hz)
7
8 t = 1/f.*[1:length(U_signal)]; % Time vector (s)
9 H = 0.016; % Channel full height (m)
10
11 %% Calculated parameters
12 U_mean = mean(U_signal); % Mean velocity (m/s)
13 u = U_signal - U_mean; % Velocity fluctuations (m/s)
14 t_norm = t.*U_mean/H; % Normalized time (-)
15
16 %% Apply high-pass filter
17 f_pass_norm = 0.05; % Normalized filter frequency (-)
18 f_pass = f_pass_norm*U_mean/H; % Cutoff frequency (Hz)
19 u_filtered = highpass(u,f_pass,f); % Filtered signal
20
21 %% Moving average and standard deviation
22 Filter_length_norm = 10; % Normalized filter length (-)
23 filter_length_datapoint = round(Filter_length_norm*fH/U_mean); % Length in
24 data points (-)
25 x =
26 movstd(u_filtered,filter_length_datapoint)./movmean(U_signal,filter_length
27 _datapoint); % Detection parameter (-)
28
29 %% Laminar/turbulent threshold
30 TR = 0.03; % Laminar/turbulent threshold (-)
31
32 %% Minimum segment length
33 Minimum_segment_length_norm = 25; % Normalized minimum length (-)
34 Minimum_segment_length_datapoint =
35 round(Minimum_segment_length_norm*fH/U_mean); % Length in data points (-)
36
37 %% Identify turbulent zones
38 Identify_turb_segments = bwareafilt(x>TR,
39 [Minimum_segment_length_datapoint, inf]);
40
41 %% Extract turbulent velocity
```



```
42
43 U_turb_segments = U_signal.*Identify_turb_segments;
44 U_turb_segments(U_turb_segments==0) = NaN;
45 U_turb_stitched = U_signal(Identify_turb_segments);
46
47 %% Identify laminar zones
48 Identify_lam_segments = bwareafilt(x<TR,
49 [Minimum_segment_length_datapoint, inf]);
50
51 %% Extract laminar velocity
52 U_lam_segments = U_signal.*Identify_lam_segments;
53 U_lam_segments(U_lam_segments==0) = NaN;
54 U_lam_stitched = U_signal(Identify_lam_segments);
55
56 %% Calculate turbulence intensities
57 TI_turb = std(U_turb_stitched)/mean(U_turb_stitched);
58 TI_lam = std(U_lam_stitched)/mean(U_lam_stitched);
```

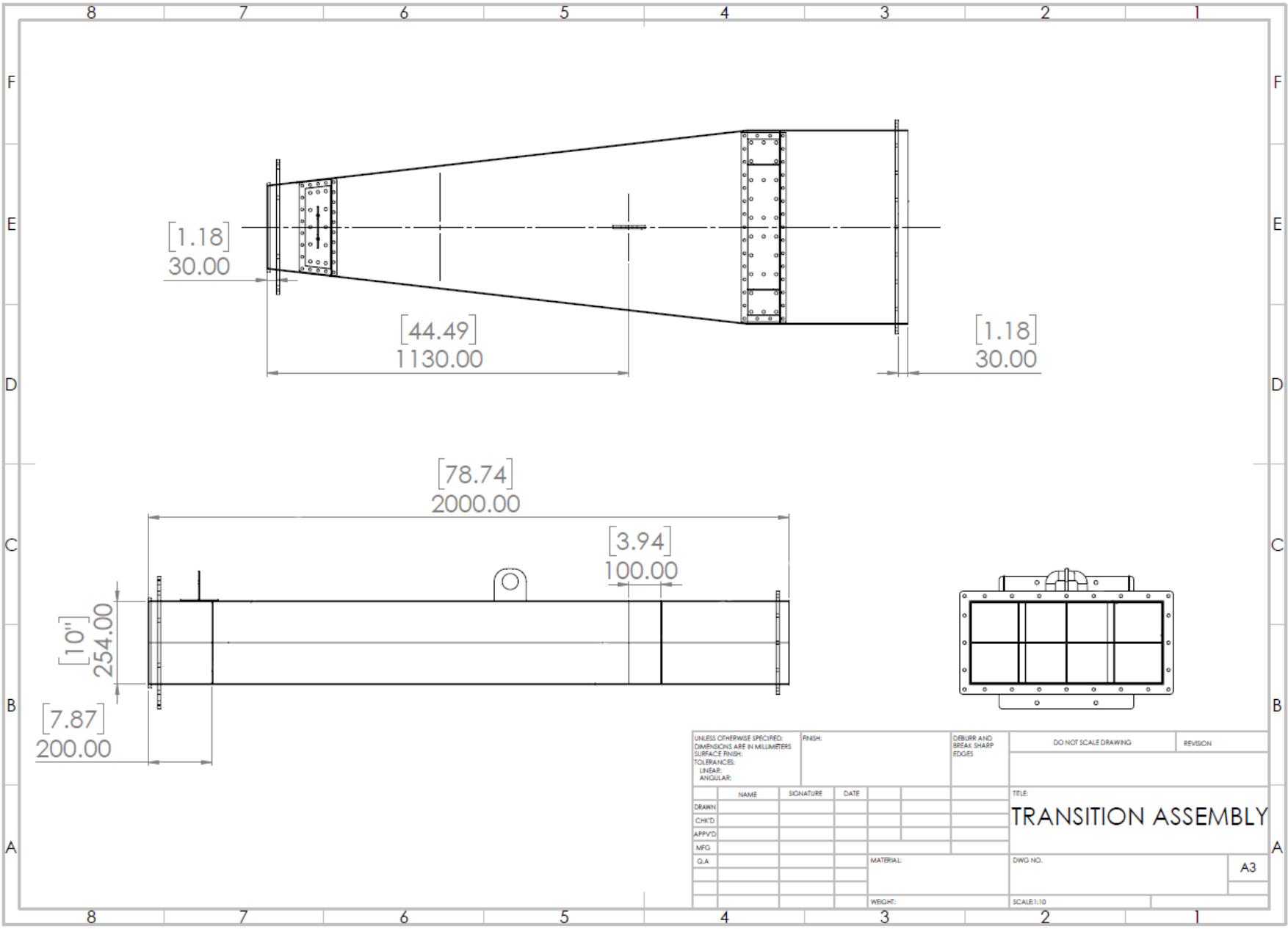
## **B Technical Drawings of the Flow Facility**

The flow facility used in this study was designed under the supervision of Dr. Sina Ghaemi, and technical drawings were prepared by Dave Tataryn. The facility was commissioned by the writer. SolidWorks 3D CAD software was utilized for designing the flow facility components. The following pages provide detailed technical drawings of the settling chamber, contraction section, acrylic test section, and diffuser.

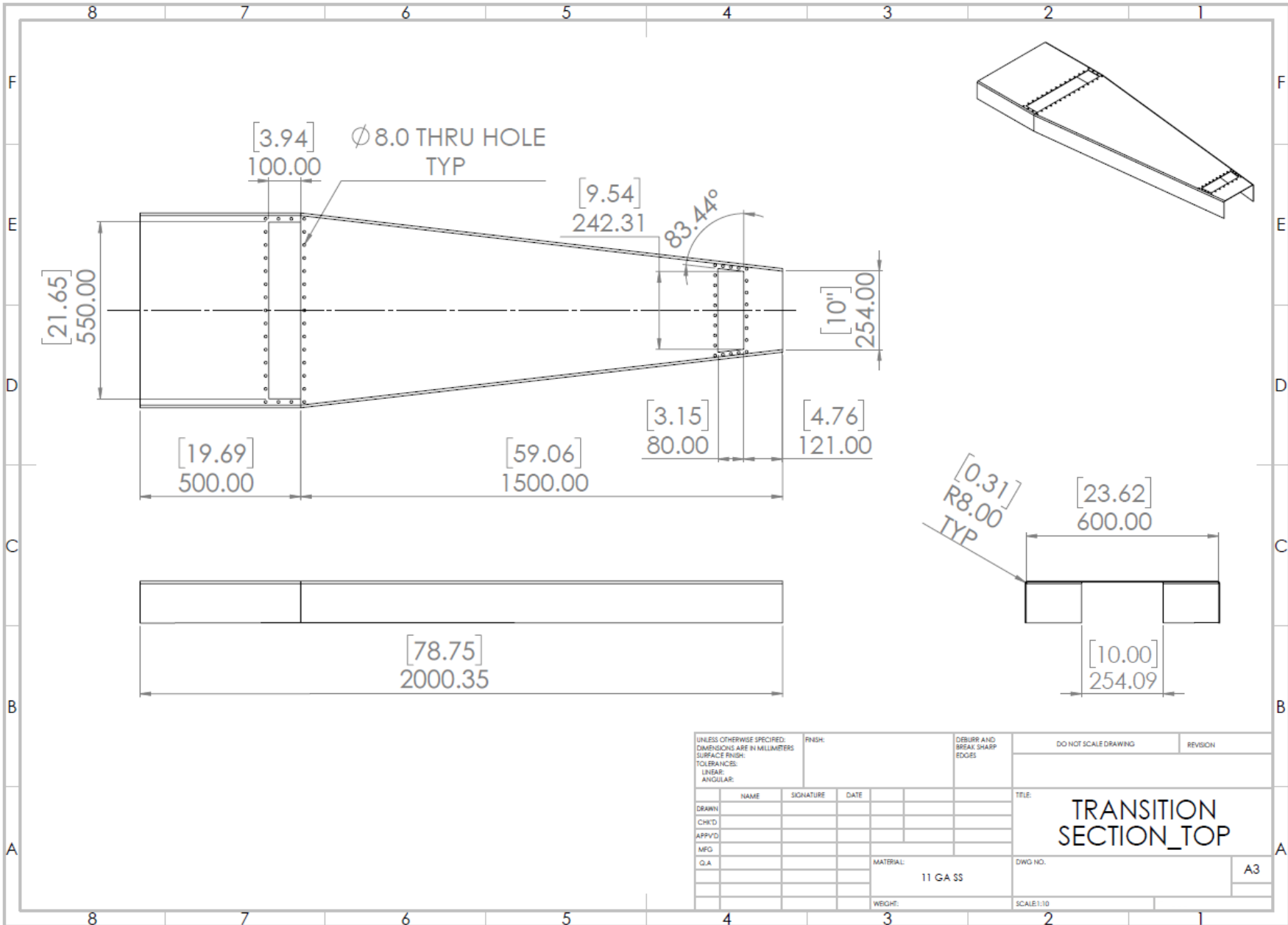


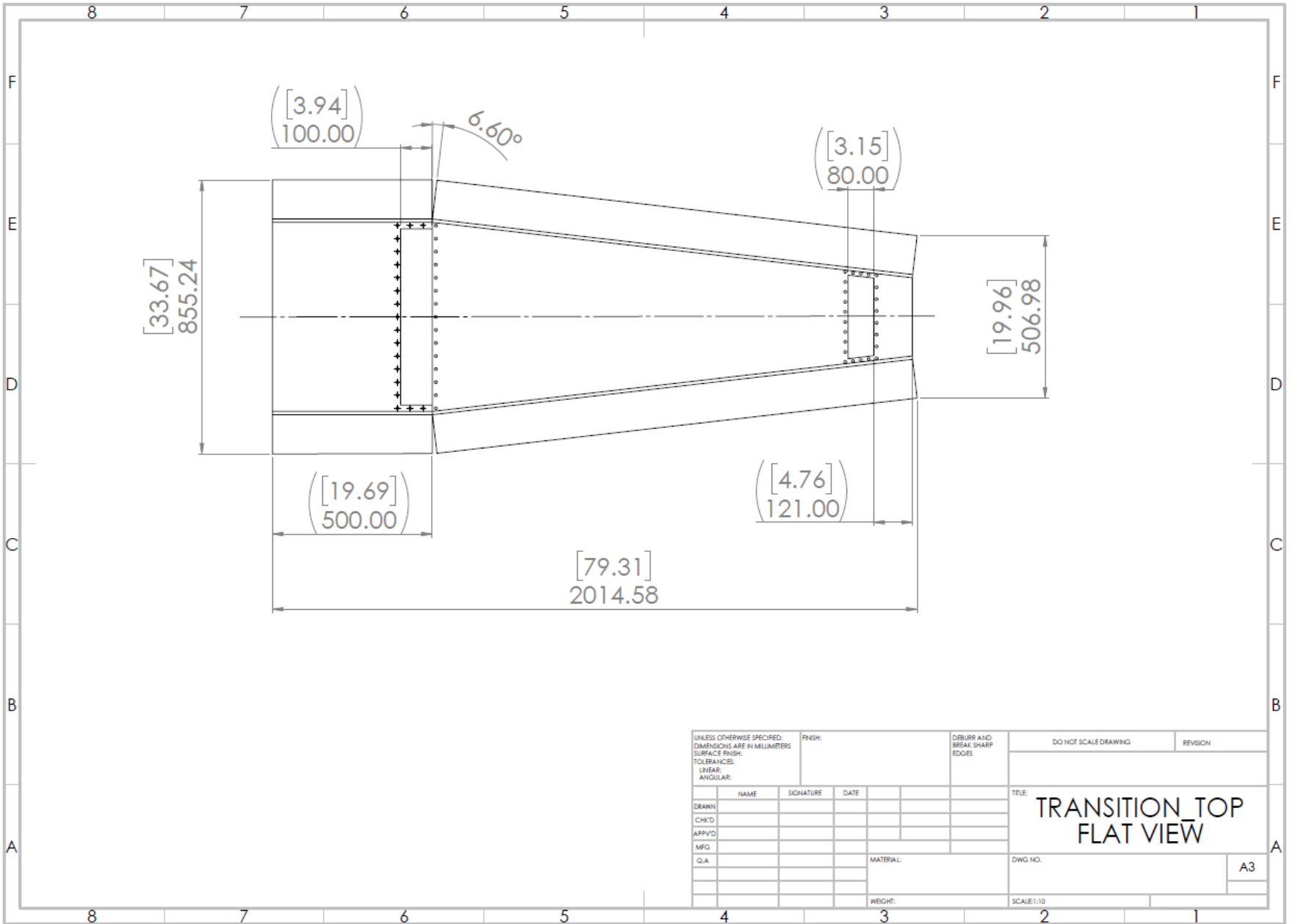
ITEM NO.	DESCRIPTION	QTY.
1	NOZZLE ASSEMBLY	1
2	BAFFLE ASSEMBLY	1
3	TRANSITION ASSEMBLY	1
4	FLANGE BOLTS - M8X60 SHCS	36
5	TRAP LID ASSEMBLY	1
6	LIFTING EYE	1
7	LID ASSEMBLY	1
8	LID BOLTS - M8X12 STUDS	62
9	HONEYCOMB BRACE	1
10	INLET HONEYCOMB BRACE	1
11	INLET SPACER	1

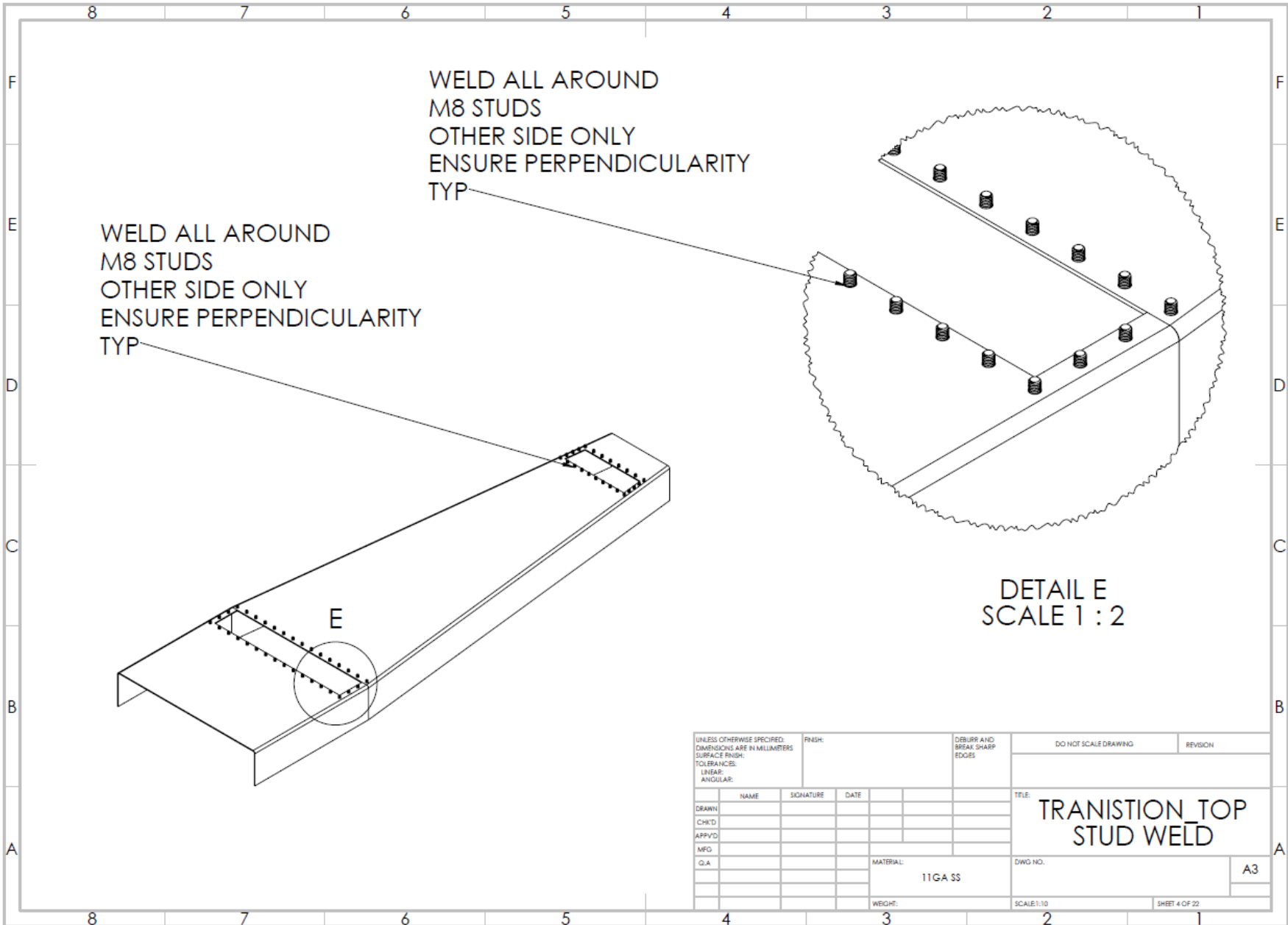
UNLESS OTHERWISE SPECIFIED: DIMENSIONS ARE IN MILLIMETERS				FINISH:		D/BURR AND BREAK SHARP EDGES		DO NOT SCALE DRAWING		REVISION	
SURFACE FINISH:											
TOLERANCES:											
LINEAR:											
ANGULAR:											
DRAWN		NAME		SIGNATURE		DATE		TITLE:		TRANSITION ASSEMBLY BOM	
CH'D											
APP'VD											
MFG											
Q.A								MATERIAL:		DWG NO.	
										A3	
								WEIGHT:		SCALE:1:10	



UNLESS OTHERWISE SPECIFIED: DIMENSIONS ARE IN MILLIMETERS SURFACE FINISH: TOLERANCES: LINEAR: ANGULAR:			FINISH:	DEBURR AND BREAK SHARP EDGES	DO NOT SCALE DRAWING	REVISION
NAME	SIGNATURE	DATE			TITLE: <b>TRANSITION ASSEMBLY</b>	
DRAWN					DWG NO.	A3
CHK'D					SCALE: 1:10	
APP'VD						
MFG				MATERIAL:		
Q.A				WEIGHT:		





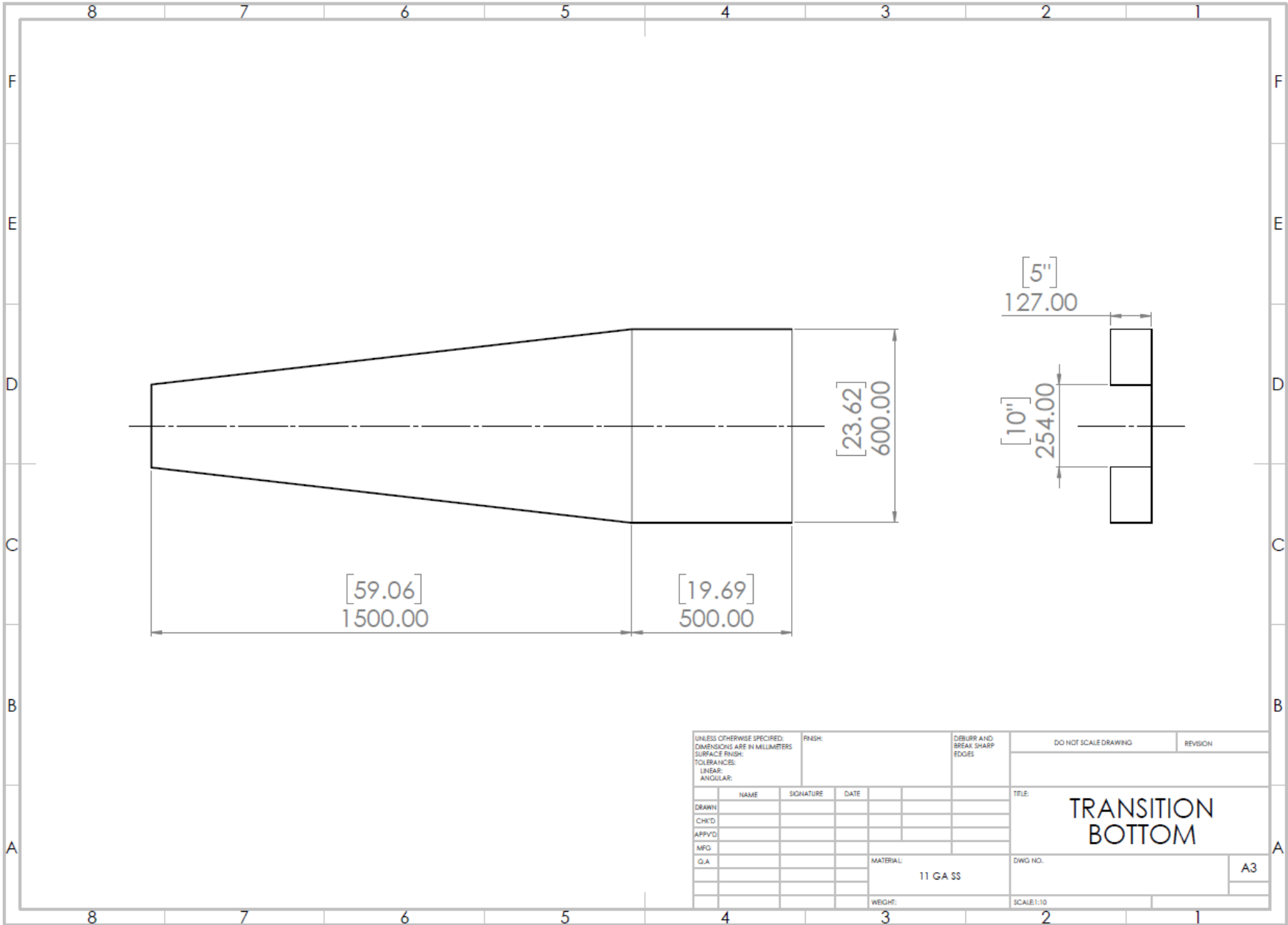


WELD ALL AROUND  
M8 STUDS  
OTHER SIDE ONLY  
ENSURE PERPENDICULARITY  
TYP

WELD ALL AROUND  
M8 STUDS  
OTHER SIDE ONLY  
ENSURE PERPENDICULARITY  
TYP

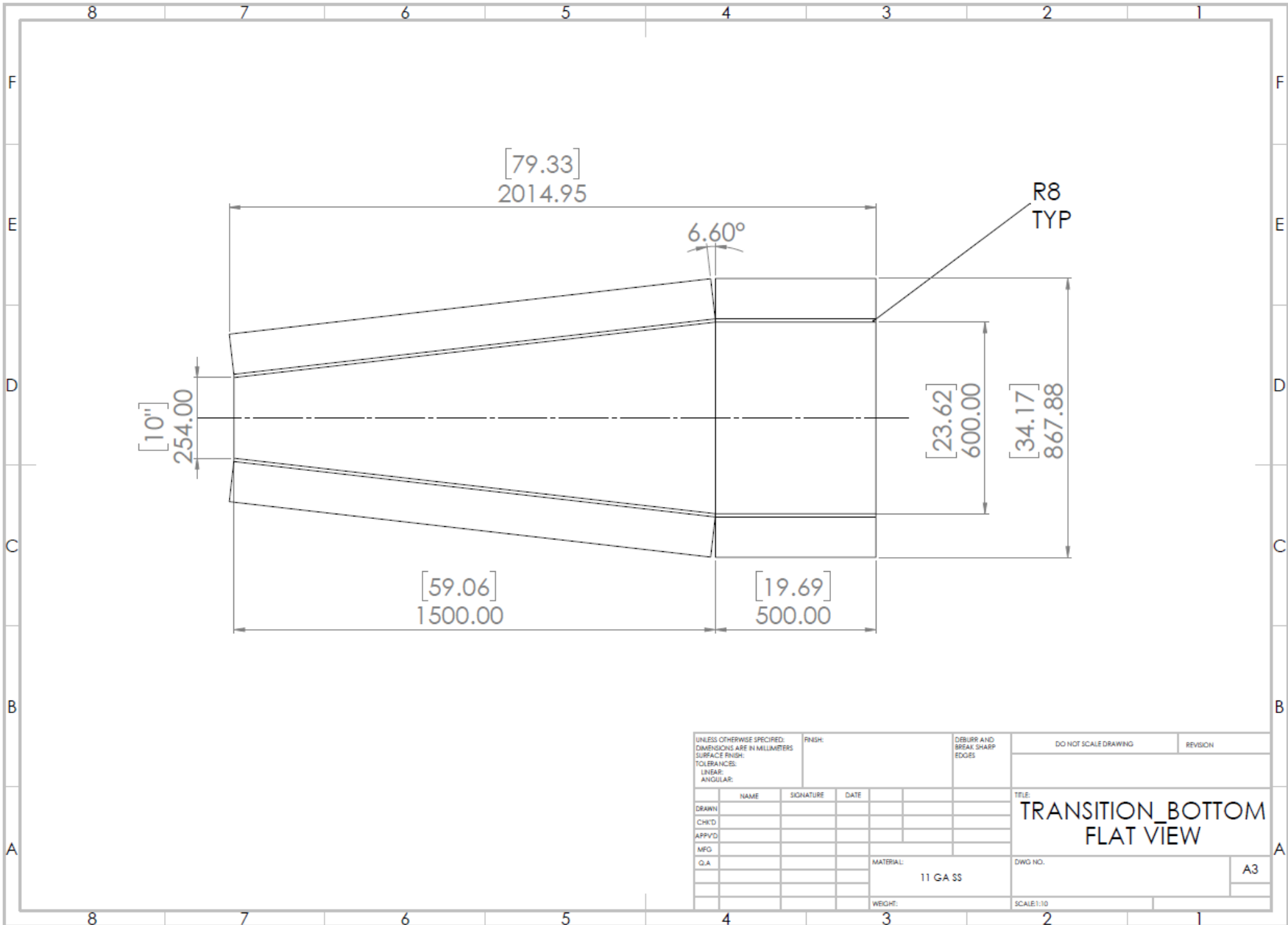
DETAIL E  
SCALE 1 : 2

UNLESS OTHERWISE SPECIFIED: DIMENSIONS ARE IN MILLIMETERS SURFACE FINISH: TOLERANCES: LINEAR: ANGULAR:				FINISH:	DEBURR AND BREAK SHARP EDGES	DO NOT SCALE DRAWING	REVISION
DRAWN	NAME	SIGNATURE	DATE			TITLE: <b>TRANSITION TOP STUD WELD</b>	
CHK'D						DWG NO.	A3
APP'VD							
MFG					MATERIAL: 11GA SS		
Q.A					WEIGHT:	SCALE: 1:10	SHEET 4 OF 22

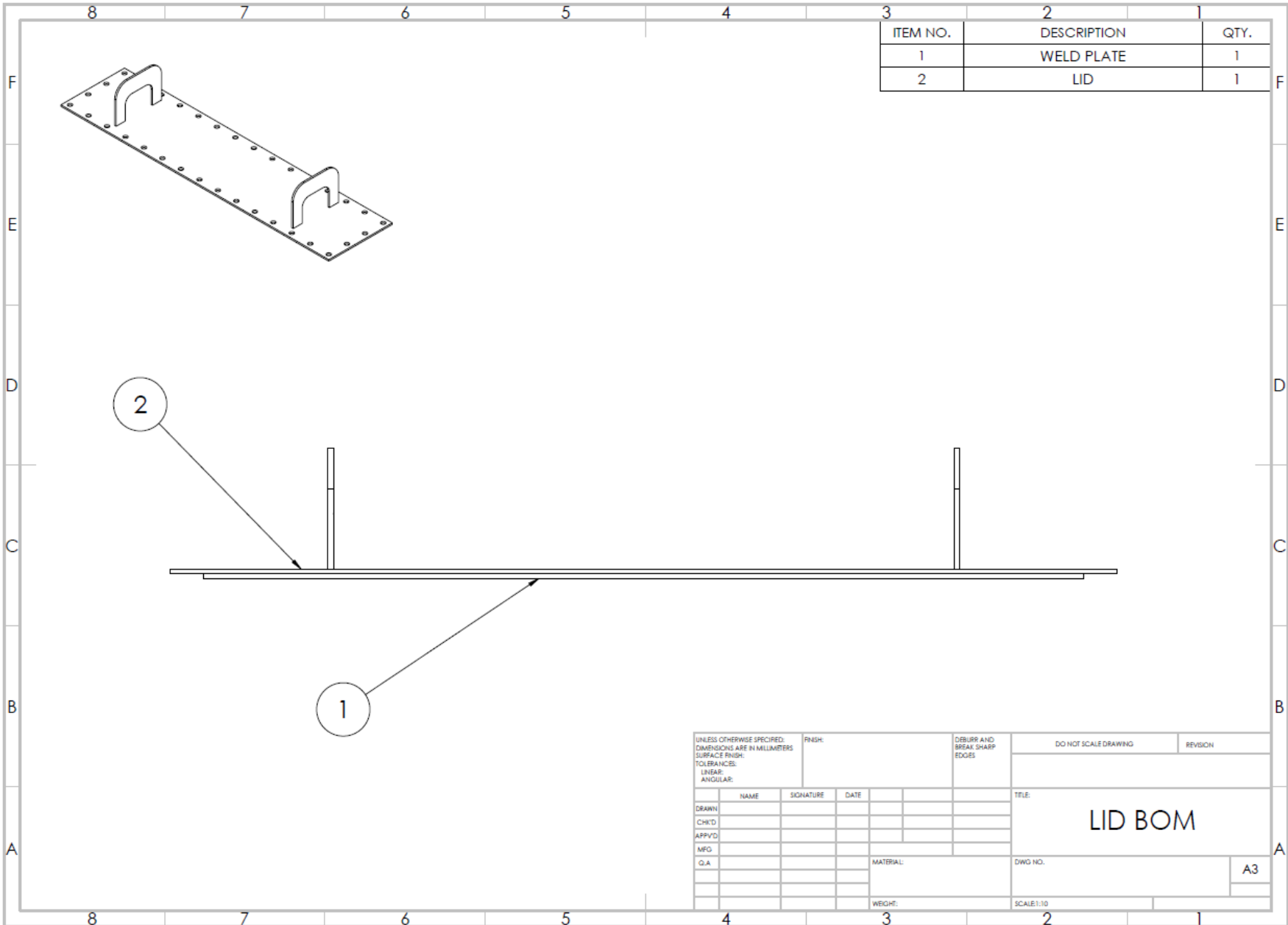


UNLESS OTHERWISE SPECIFIED: DIMENSIONS ARE IN MILLIMETERS				FINISH:		DEBURR AND BREAK SHARP EDGES		DO NOT SCALE DRAWING		REVISION	
SURFACE FINISH:				TOLERANCES:		LINEAR:		ANGULAR:		TITLE:	
DRAWN				NAME		SIGNATURE		DATE		11 GA SS	
CHK'D										TITLE: TRANSITION BOTTOM	
APP'VD										DWG NO.	
MFG										A3	
Q.A										SCALE: 1:10	



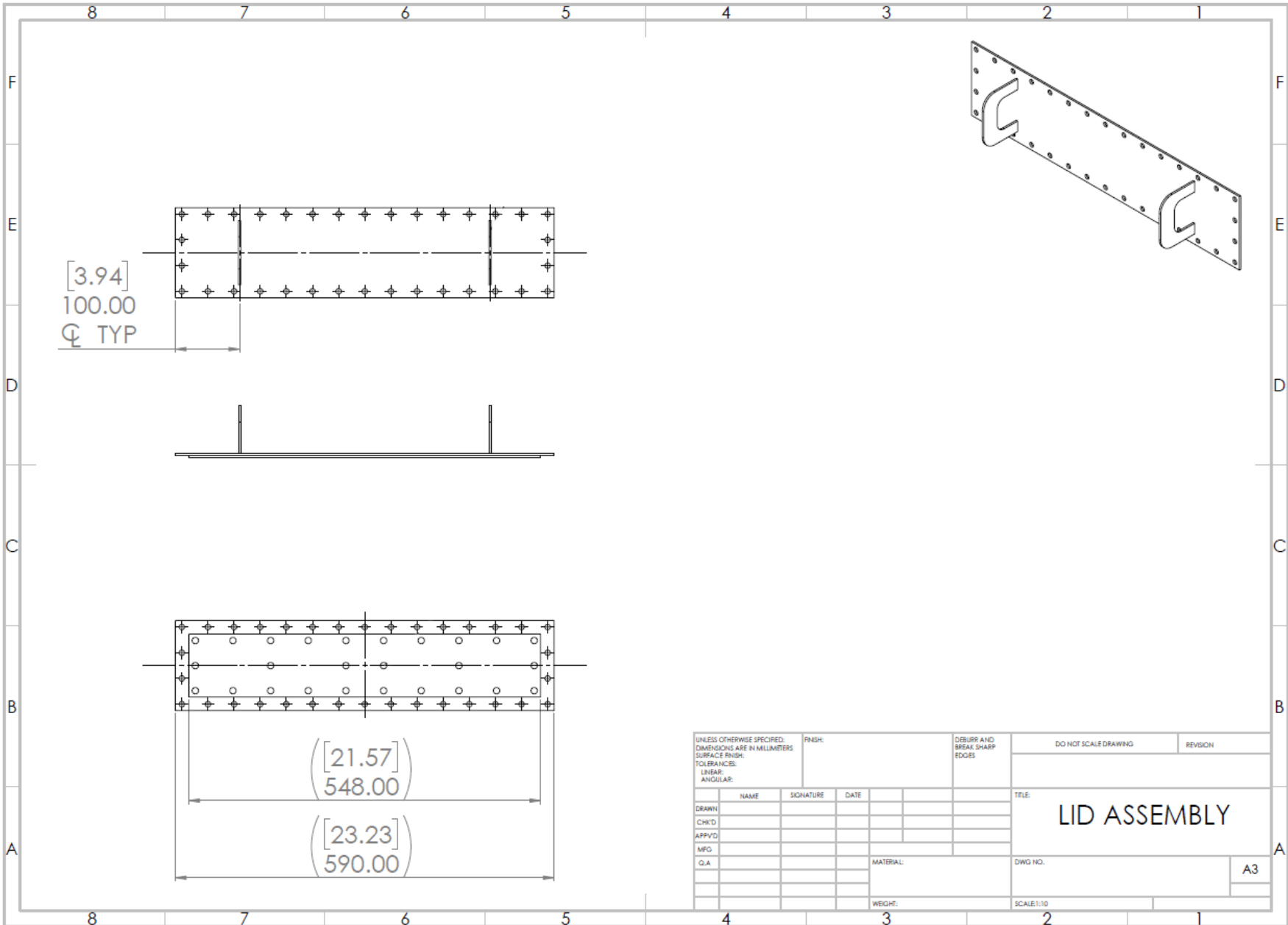


UNLESS OTHERWISE SPECIFIED: DIMENSIONS ARE IN MILLIMETERS				FINISH:		DEBURR AND BREAK SHARP EDGES		DO NOT SCALE DRAWING		REVISION	
SURFACE FINISH:				DATE						TITLE: TRANSITION_BOTTOM FLAT VIEW	
TOLERANCES: LINEAR: ANGULAR:				SIGNATURE						DWG NO.	
DRAWN				MATERIAL: 11 GA SS						A3	
CHK'D				WEIGHT:						SCALE:1:10	
APP'VD											
MFG											
Q.A											

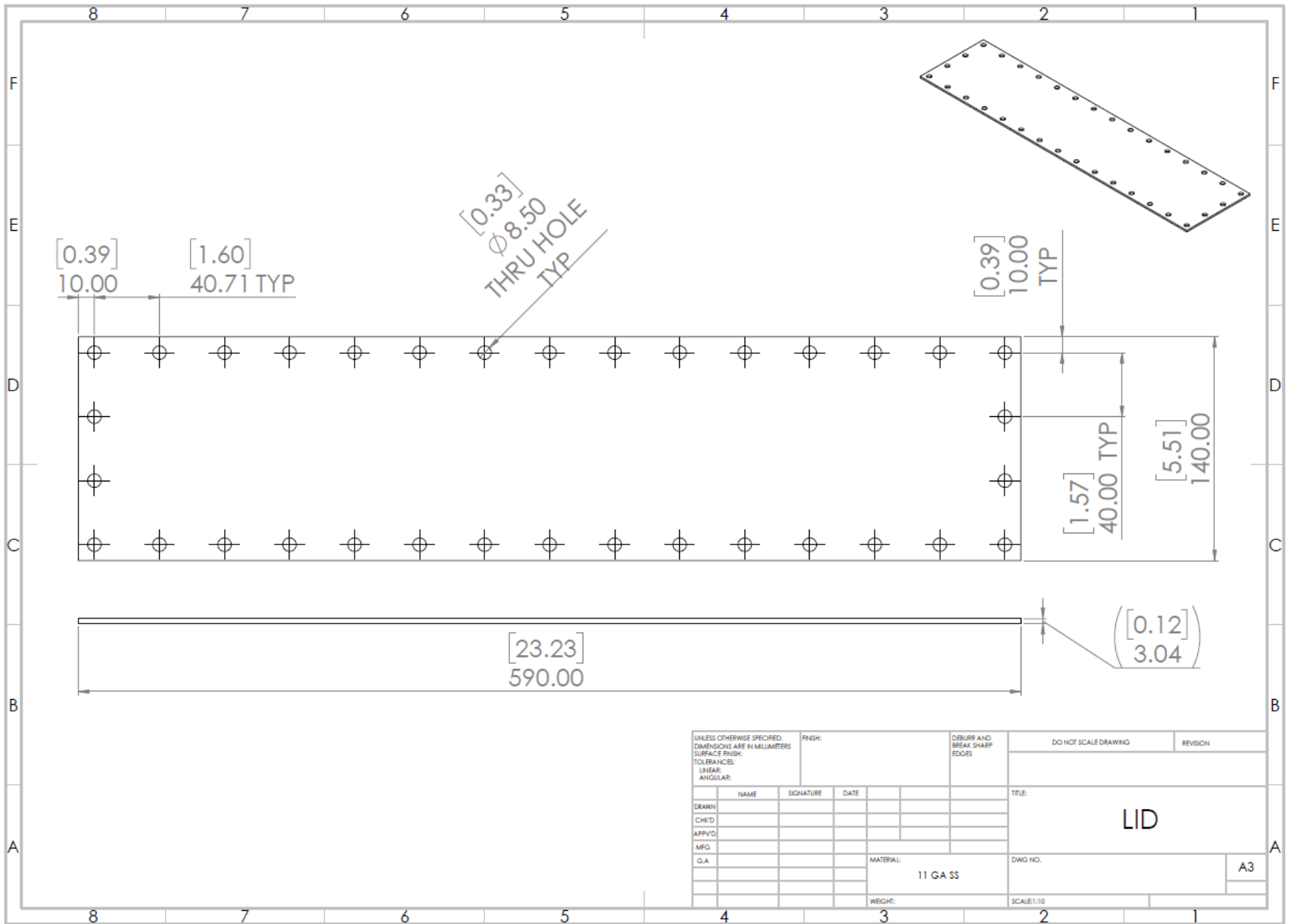


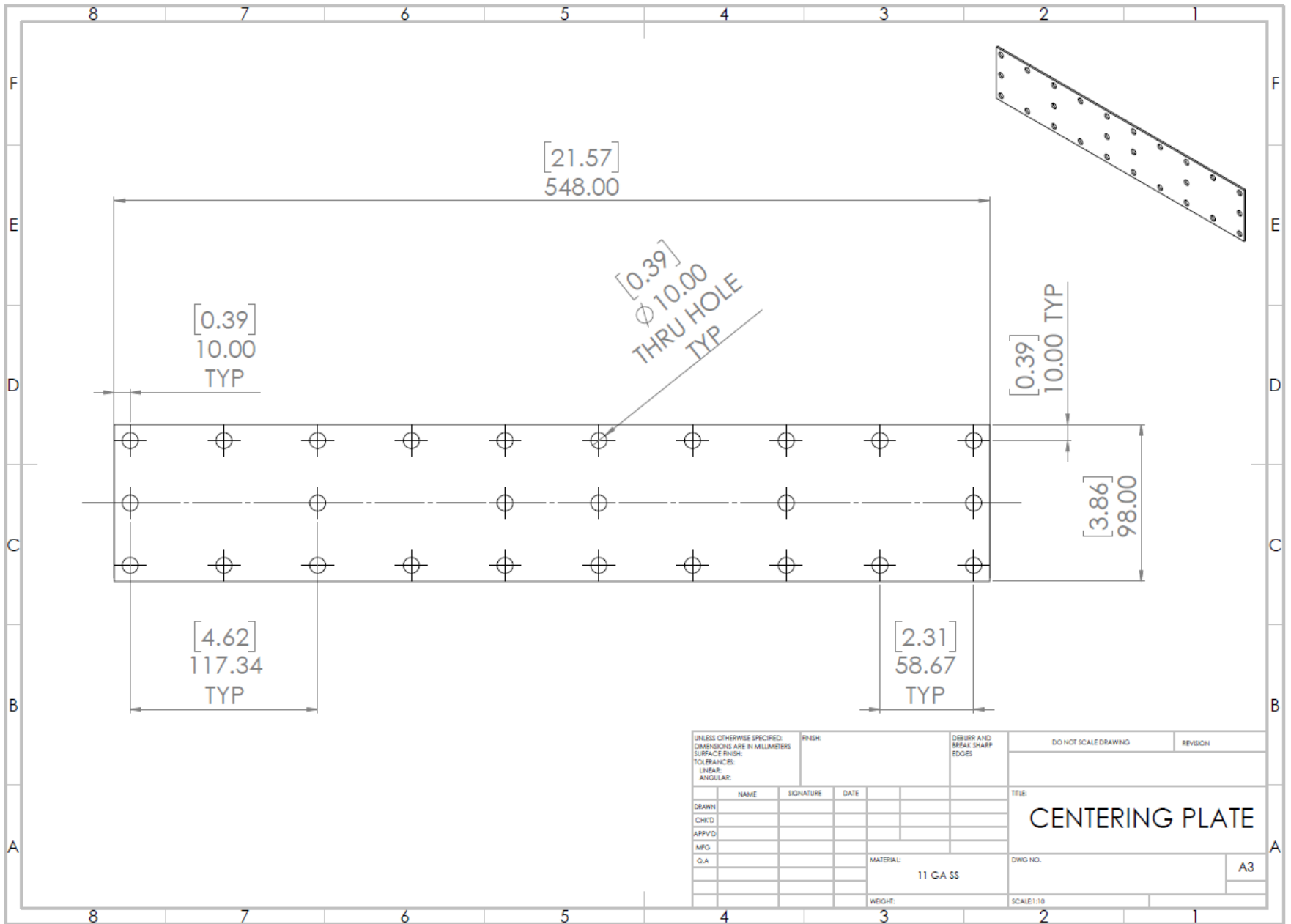
ITEM NO.	DESCRIPTION	QTY.
1	WELD PLATE	1
2	LID	1

UNLESS OTHERWISE SPECIFIED: DIMENSIONS ARE IN MILLIMETERS				FINISH:		DEBURR AND BREAK SHARP EDGES		DO NOT SCALE DRAWING		REVISION	
SURFACE FINISH:											
TOLERANCES:											
LINEAR:											
ANGULAR:											
DRAWN		NAME		SIGNATURE		DATE		TITLE:		LID BOM	
CHK'D											
APP'VD											
MFG											
Q.A								MATERIAL:		DWG NO.	
										A3	
								WEIGHT:		SCALE:1:10	

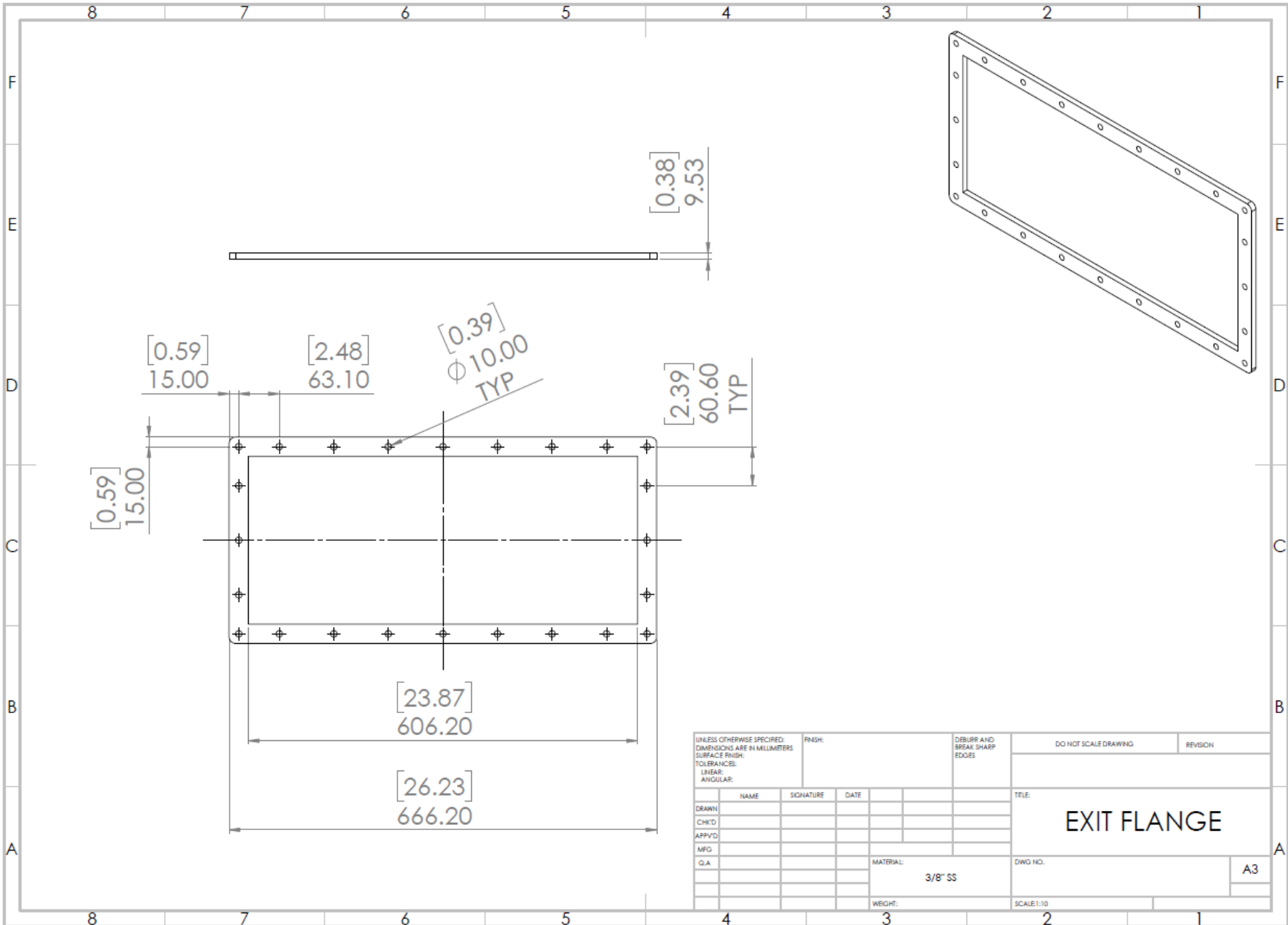


UNLESS OTHERWISE SPECIFIED: DIMENSIONS ARE IN MILLIMETERS				FINISH:		DEBURR AND BREAK SHARP EDGES		DO NOT SCALE DRAWING		REVISION	
SURFACE FINISH:											
TOLERANCES:											
LINEAR:											
ANGULAR:											
DRAWN		NAME		SIGNATURE		DATE		TITLE:		LID ASSEMBLY	
CHK'D											
APP'VD											
MFG											
Q.A								MATERIAL:		DWG NO.	
										A3	
								WEIGHT:		SCALE: 1:10	

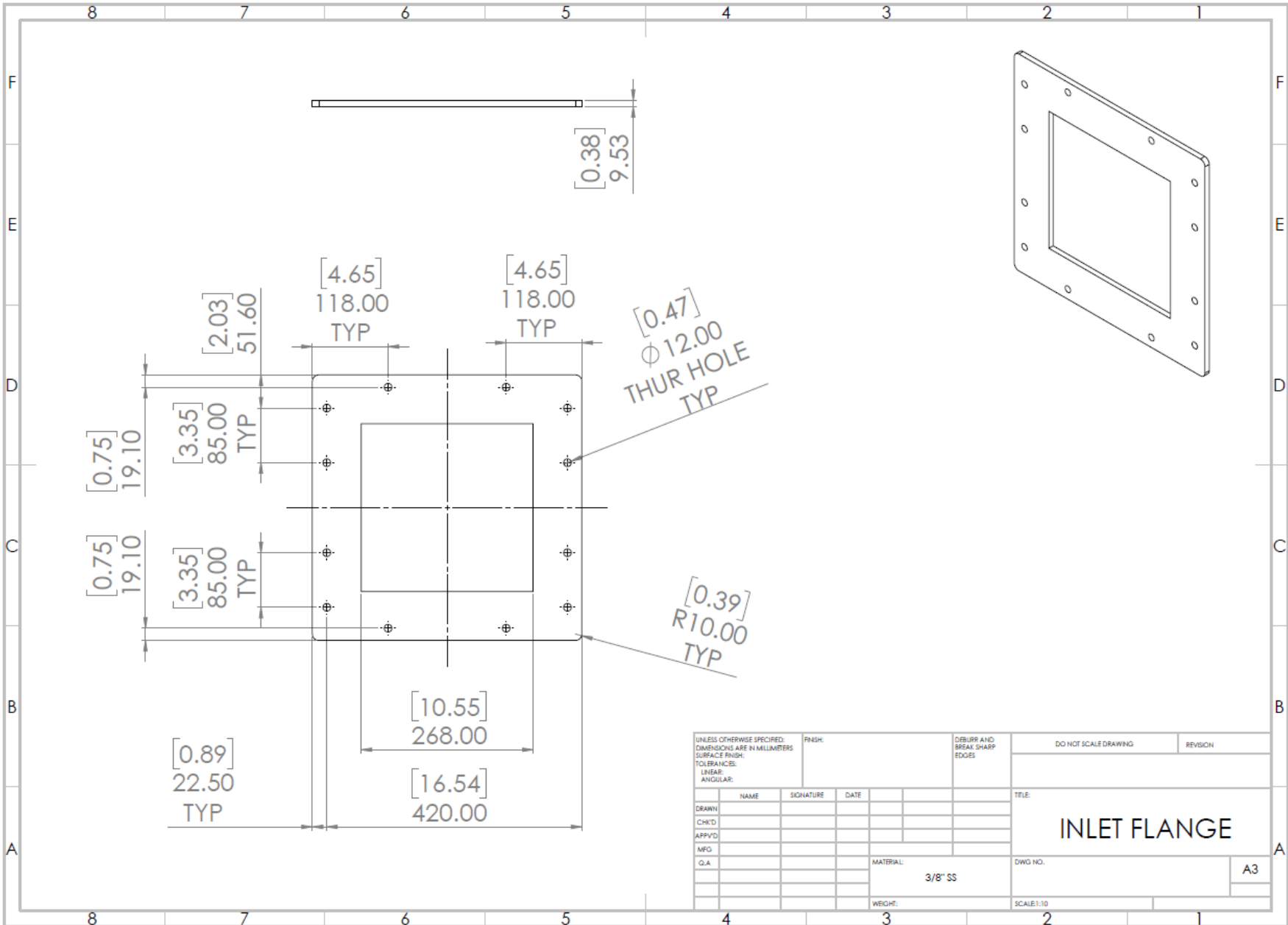




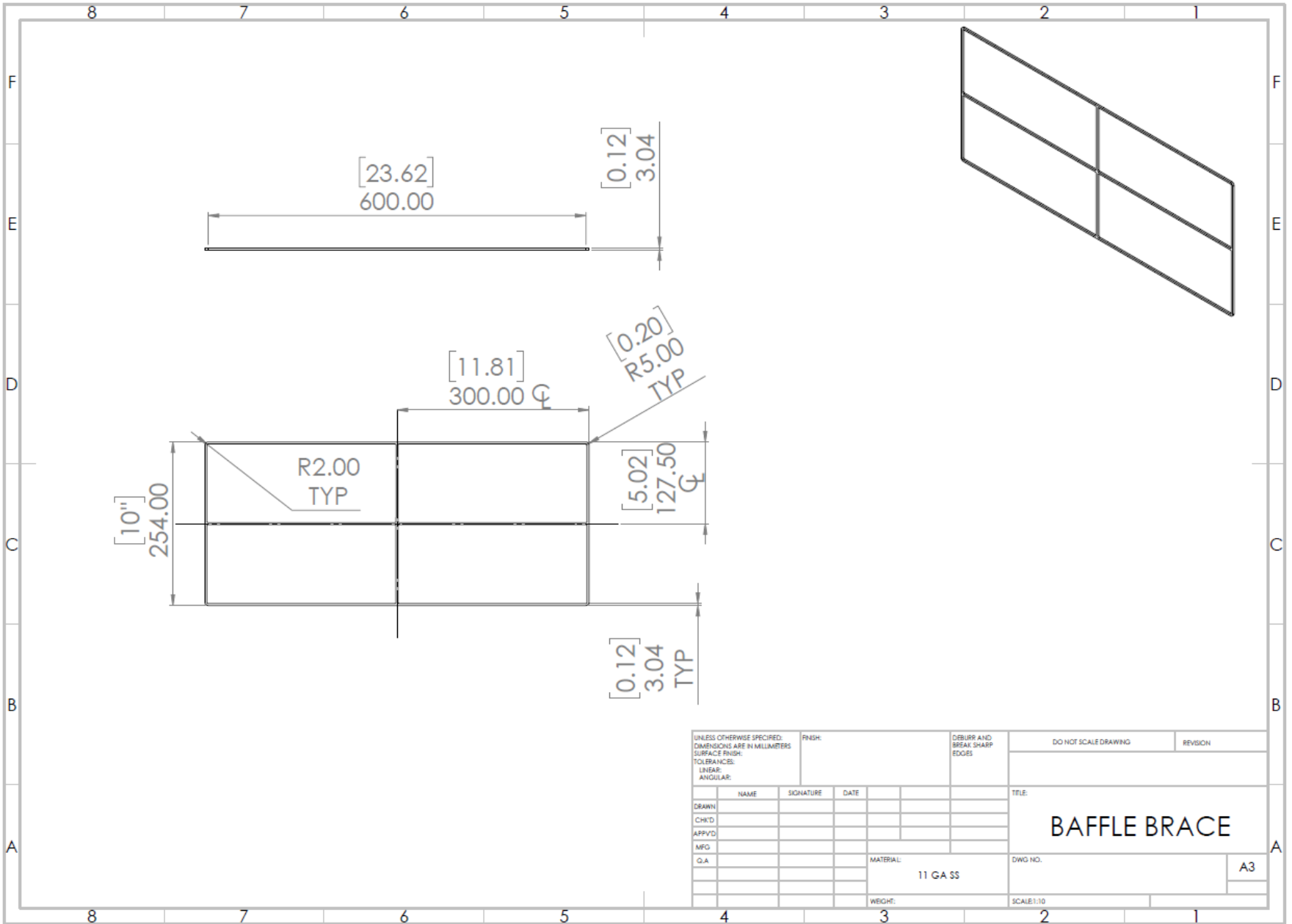
UNLESS OTHERWISE SPECIFIED: DIMENSIONS ARE IN MILLIMETERS SURFACE FINISH: TOLERANCES: LINEAR: ANGULAR:				FINISH:		DEBURR AND BREAK SHARP EDGES		DO NOT SCALE DRAWING		REVISION	
DRAWN				NAME		SIGNATURE		DATE		TITLE:	
CHK'D										CENTERING PLATE	
APP'VD										DWG NO.	
MFG										A3	
Q.A										SCALE: 1:10	
										MATERIAL: 11 GA SS	
										WEIGHT:	



UNLESS OTHERWISE SPECIFIED: DIMENSIONS ARE IN MILLIMETERS SURFACE FINISH: TOLERANCES: LINEAR: ANGULAR:				FINISH:		DEBURR AND BREAK SHARP EDGES		DO NOT SCALE DRAWING		REVISION	
DRAWN	NAME	SIGNATURE	DATE			TITLE: <b>EXIT FLANGE</b>					
CHK'D											
APP'VD											
MFG											
Q.A						MATERIAL: 3/8" SS		DWG NO.		A3	
						WEIGHT:		SCALE: 1:10			

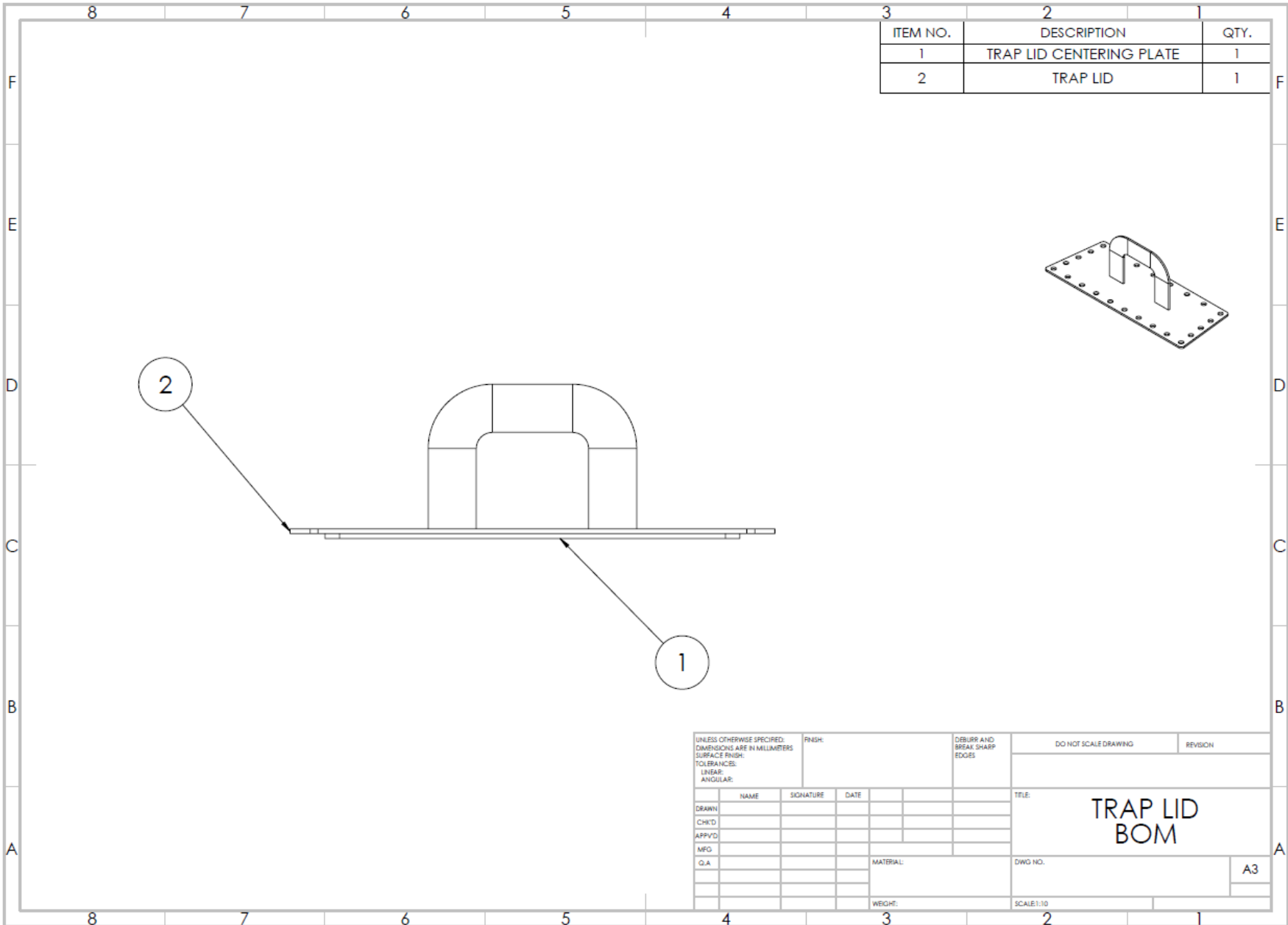


UNLESS OTHERWISE SPECIFIED: DIMENSIONS ARE IN MILLIMETERS				FINISH:		DEBURR AND BREAK SHARP EDGES		DO NOT SCALE DRAWING		REVISION	
TOLERANCES: LINEAR: ANGULAR:											
DRAWN		SIGNATURE		DATE						TITLE:	
CHK'D										INLET FLANGE	
APP'VD											
MFG											
Q.A						MATERIAL: 3/8" SS		DWG NO.		A3	
						WEIGHT:		SCALE: 1:10			



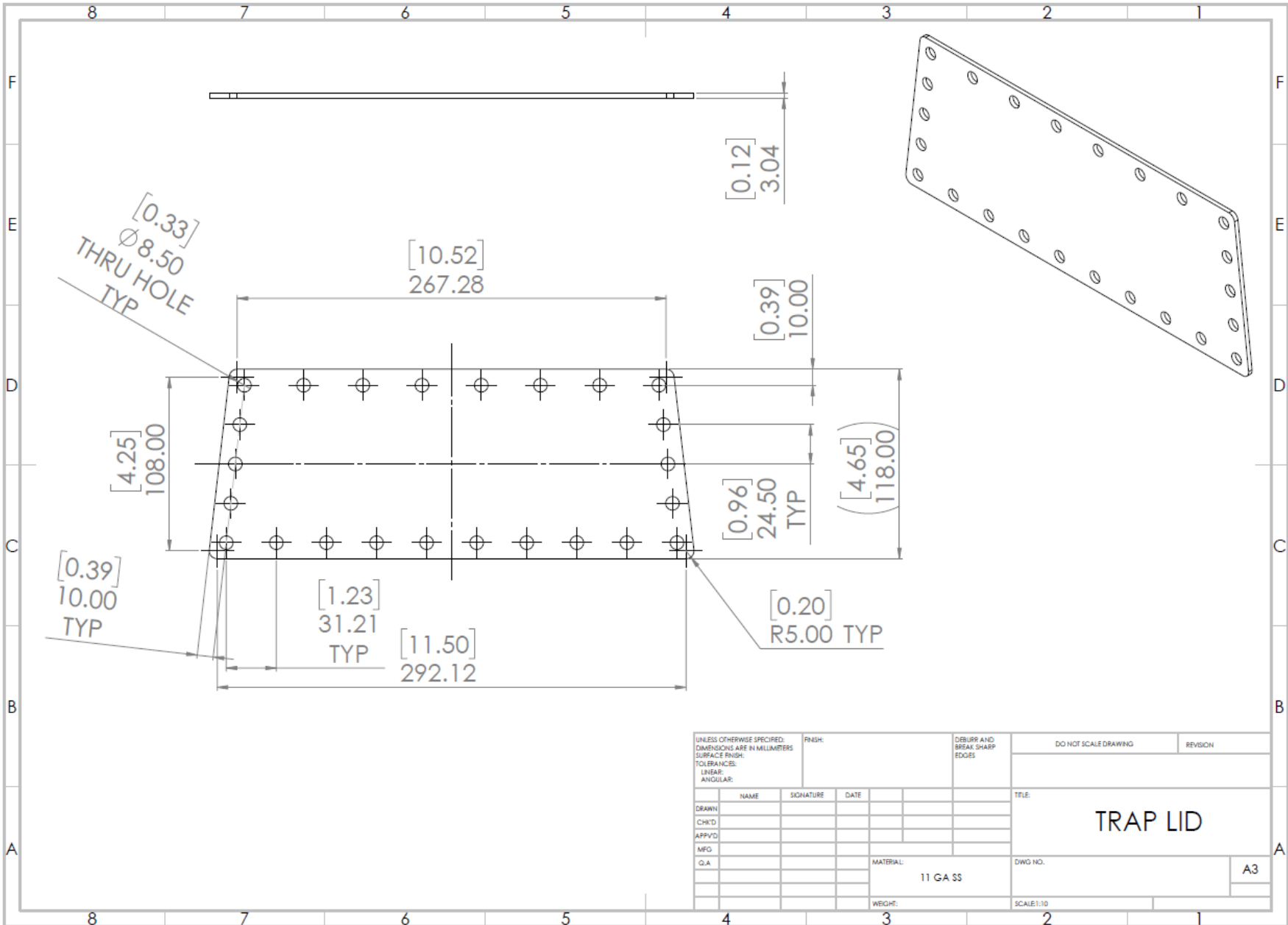
UNLESS OTHERWISE SPECIFIED: DIMENSIONS ARE IN MILLIMETERS SURFACE FINISH: TOLERANCES: LINEAR: ANGULAR:				FINISH:		DEBURR AND BREAK SHARP EDGES		DO NOT SCALE DRAWING		REVISION	
DRAWN				SIGNATURE		DATE		TITLE:			
CHK'D								<b>BAFFLE BRACE</b> DWG NO. <span style="float: right;">A3</span>			
APP'VD											
MFG											
Q.A											
				MATERIAL:		11 GA SS		SCALE: 1:10			
				WEIGHT:							



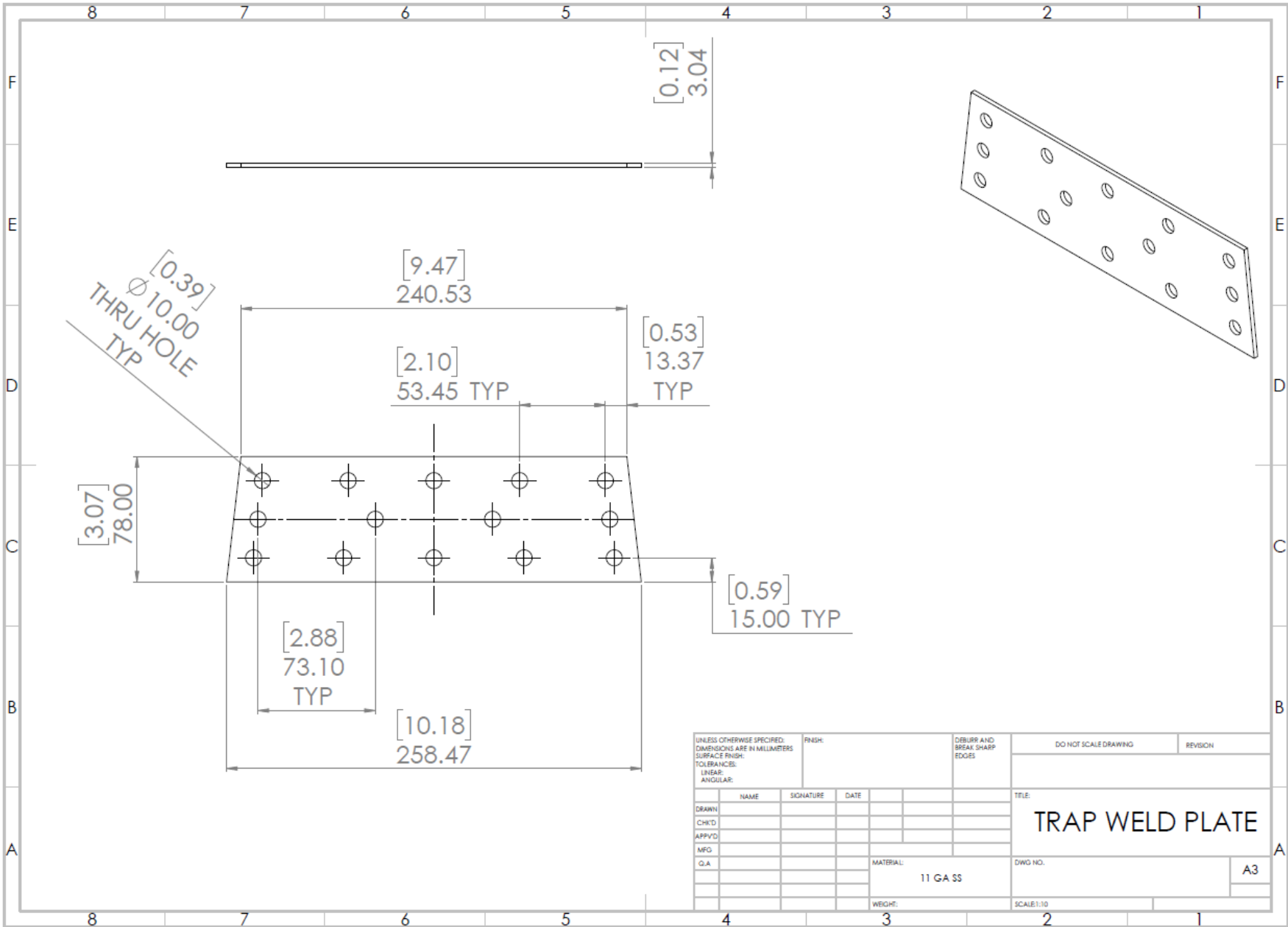


ITEM NO.	DESCRIPTION	QTY.
1	TRAP LID CENTERING PLATE	1
2	TRAP LID	1

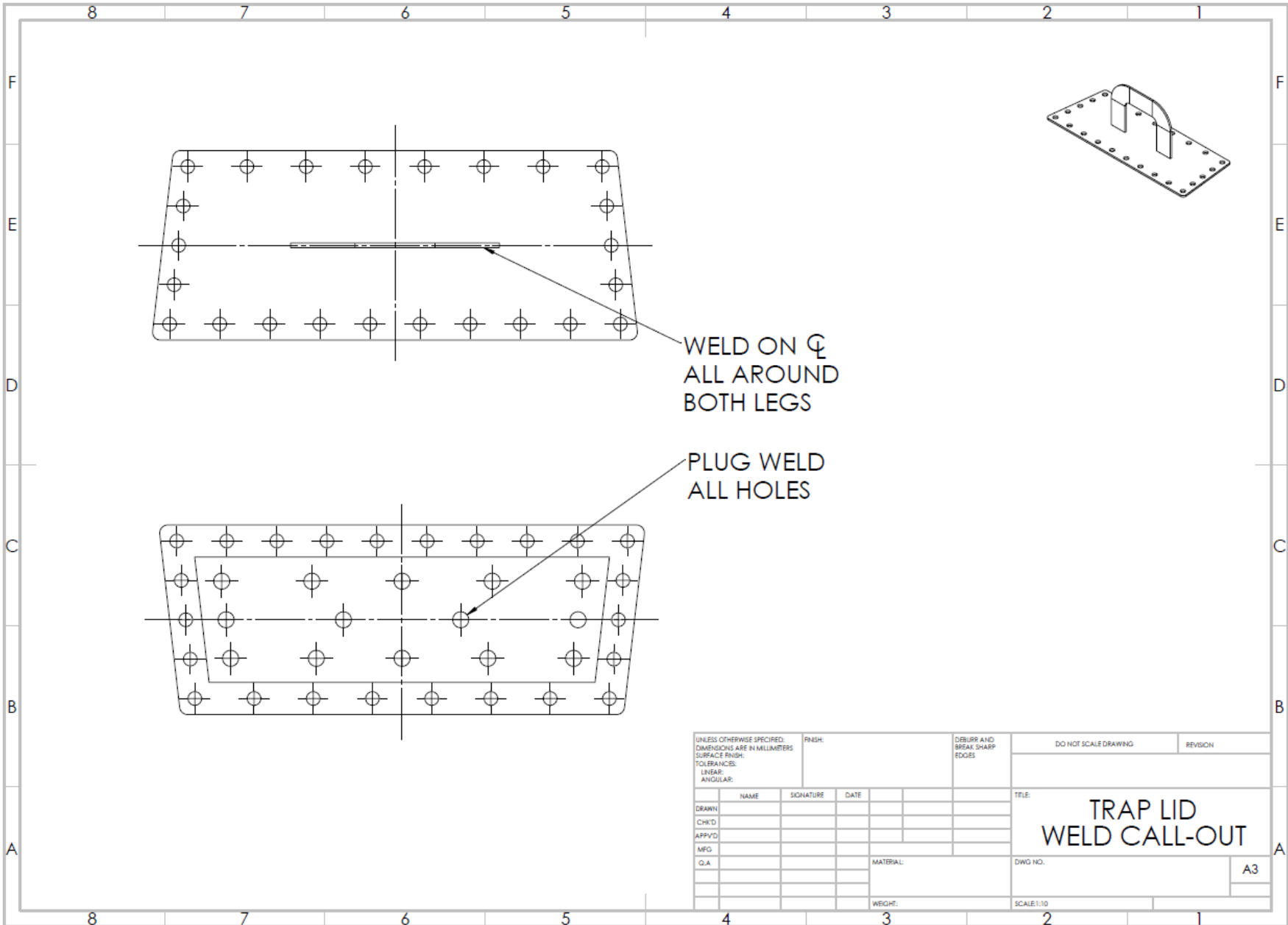
UNLESS OTHERWISE SPECIFIED: DIMENSIONS ARE IN MILLIMETERS				FINISH:		DEBURR AND BREAK SHARP EDGES		DO NOT SCALE DRAWING		REVISION	
SURFACE FINISH:				TOLERANCES:		LINEAR:		ANGULAR:		TITLE:	
DRAWN				NAME		SIGNATURE		DATE		TRAP LID BOM	
CHK'D										DWG NO.	
APP'VD										SCALE: 1:10	
MFG										A3	
Q.A										WEIGHT:	



UNLESS OTHERWISE SPECIFIED: DIMENSIONS ARE IN MILLIMETERS SURFACE FINISH: TOLERANCES: LINEAR: ANGULAR:				FINISH:		DEBURR AND BREAK SHARP EDGES		DO NOT SCALE DRAWING		REVISION	
DRAWN				SIGNATURE		DATE		TITLE:		TRAP LID	
CHK'D											
APP'VD											
MFG											
Q.A								MATERIAL:		DWG NO.	
								11 GA SS		A3	
								WEIGHT:		SCALE: 1:10	



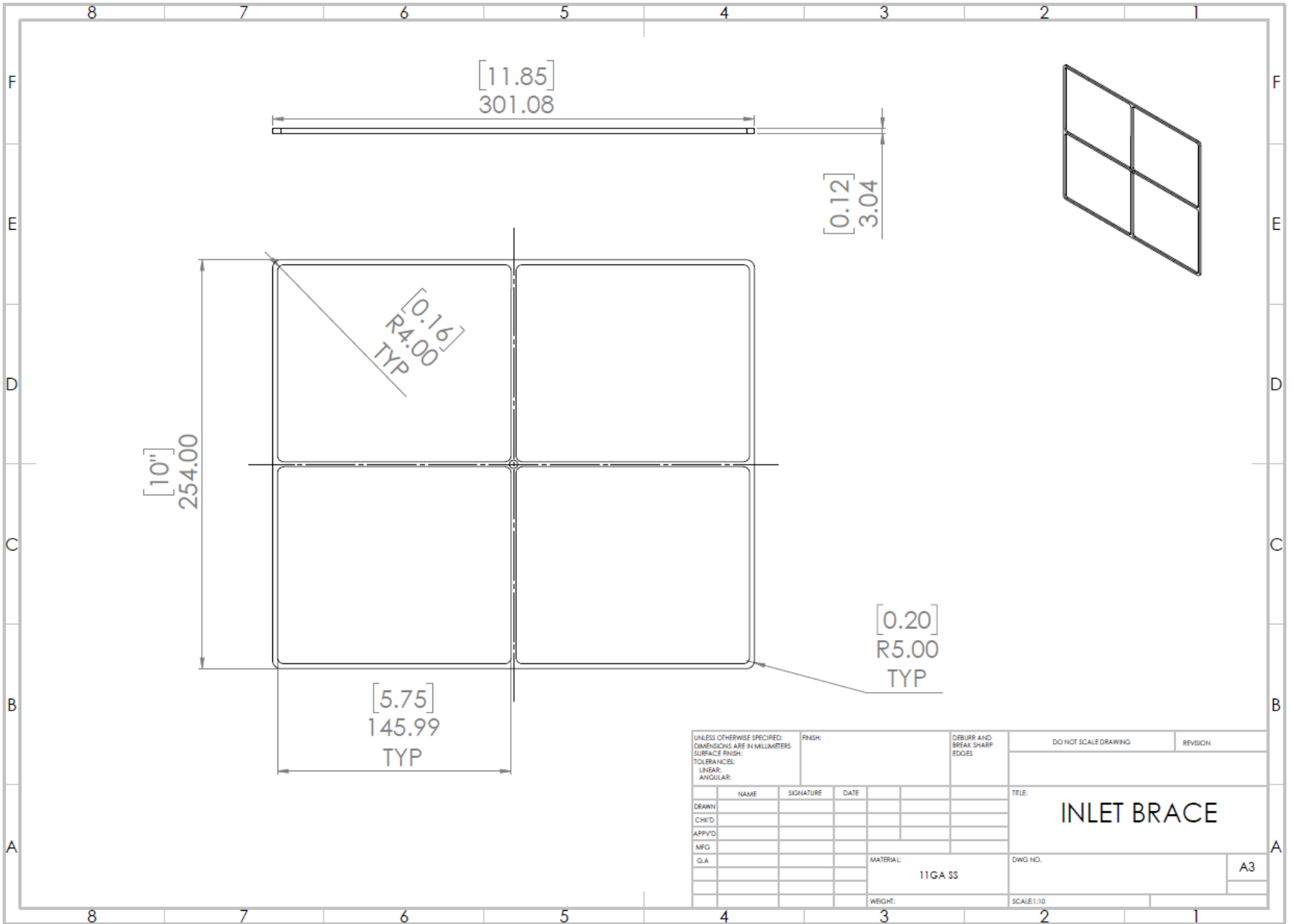
UNLESS OTHERWISE SPECIFIED: DIMENSIONS ARE IN MILLIMETERS SURFACE FINISH: TOLERANCES: LINEAR: ANGULAR:				FINISH:		DEBURR AND BREAK SHARP EDGES		DO NOT SCALE DRAWING		REVISION	
DRAWN				SIGNATURE		DATE		TITLE:		TRAP WELD PLATE	
CHK'D				SIGNATURE		DATE		MATERIAL:		DWG NO.	
APP'VD				SIGNATURE		DATE		11 GA SS		A3	
MFG				SIGNATURE		DATE		WEIGHT:		SCALE:1:10	
Q.A				SIGNATURE		DATE					



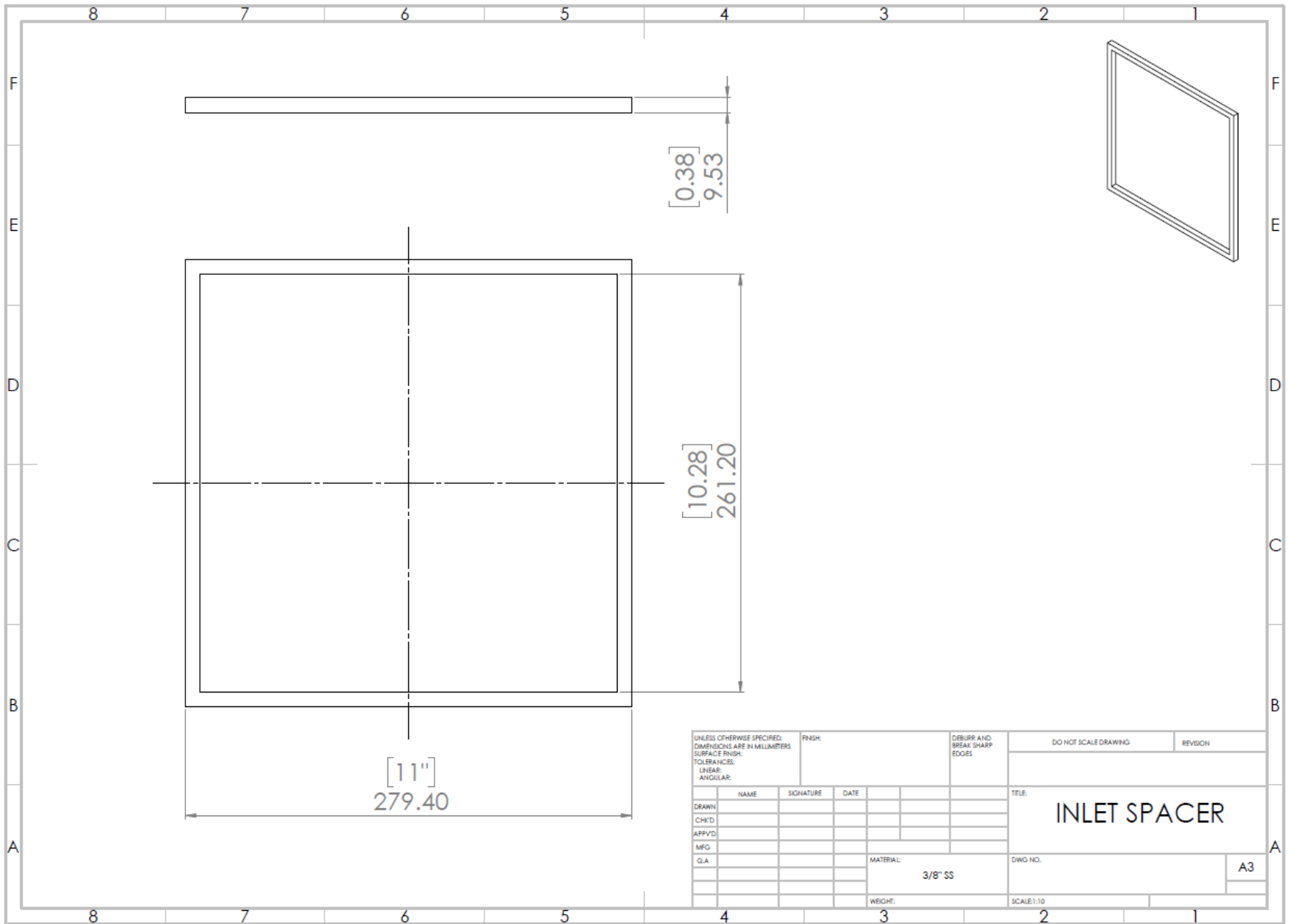
WELD ON ☉  
ALL AROUND  
BOTH LEGS

PLUG WELD  
ALL HOLES

UNLESS OTHERWISE SPECIFIED: DIMENSIONS ARE IN MILLIMETERS SURFACE FINISH: TOLERANCES: LINEAR: ANGULAR:				FINISH:		DEBURR AND BREAK SHARP EDGES		DO NOT SCALE DRAWING		REVISION	
DRAWN	NAME	SIGNATURE	DATE			TITLE: <b>TRAP LID WELD CALL-OUT</b>					
CHK'D											
APP'VD											
MFG											
Q.A					MATERIAL:	DWG NO.					
						SCALE: 1:10					
						A3					

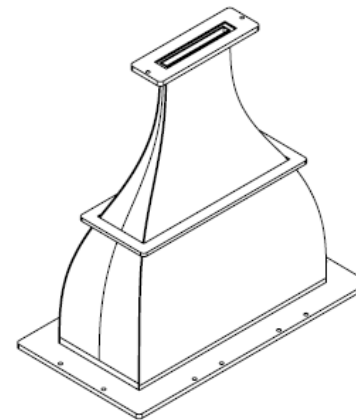
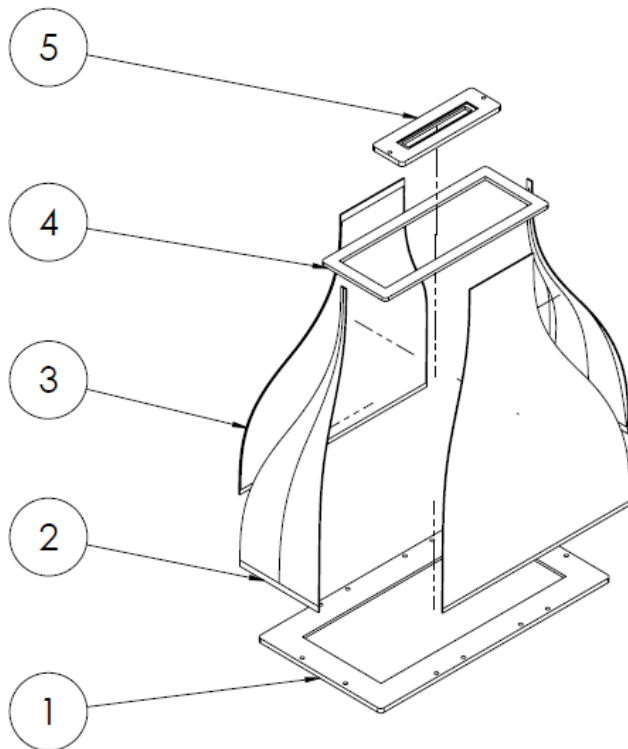


UNLESS OTHERWISE SPECIFIED: DIMENSIONS ARE IN MILLIMETERS				FINISH:		DEBURR AND BREAK SHARP EDGES		DO NOT SCALE DRAWING		REVISION	
SURFACE FINISH:											
TOLERANCES:											
LINEAR:											
ANGULAR:											
DRAWN		SIGNATURE		DATE				TITLE:		INLET BRACE	
CHK'D											
APP'VD											
MFG											
Q.A						MATERIAL:		DWG NO.		A3	
						11GA SS					
						WEIGHT:		SCALE:1:10			

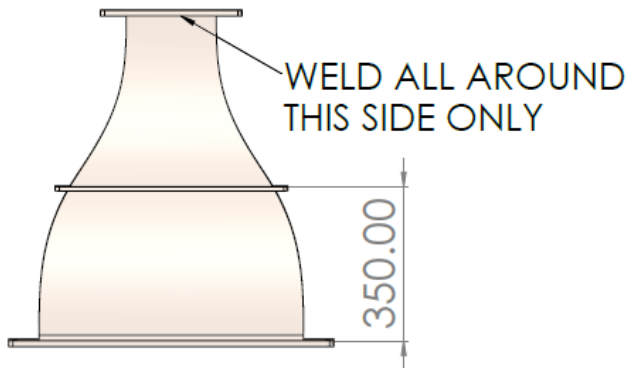


UNLESS OTHERWISE SPECIFIED: DIMENSIONS ARE IN MILLIMETERS				FINISH:		DEBURR AND BREAK SHARP EDGES		DO NOT SCALE DRAWING		REVISION	
SURFACE FINISH:				DATE		TITLE:		INLET SPACER			
TOLERANCES:				SIGNATURE		DWG NO.					
LINEAR:				DATE		MATERIAL:		SCALE: 1:10			
ANGULAR:				DATE		3/8" SS					
DRAWN		NAME		SIGNATURE		DATE					
CHK'D		NAME		SIGNATURE		DATE					
APP'VD		NAME		SIGNATURE		DATE					
MFG		NAME		SIGNATURE		DATE					
Q.A		NAME		SIGNATURE		DATE					

ITEM NO.	PART NUMBER	DESCRIPTION	QTY.
1	ENTRANCE FLANGE	1/2" 304 SS	1
2	TRANSITION_SIDE	11 GAUGE 304 SS	2
3	TRANSITION_SIDE_LARGE	11 GAUGE 304 SS	2
4	RIB	3/8" 304 SS	1
5	EXIT FLANGE	1/2" 304 SS	1



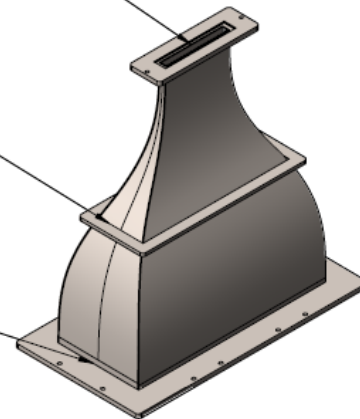
UNLESS OTHERWISE SPECIFIED: DIMENSIONS ARE IN MILLIMETERS SURFACE FINISH: TOLERANCES: LINEAR: ANGULAR:				FINISH:		DEBURR AND BREAK SHARP EDGES		DO NOT SCALE DRAWING		REVISION	
DRAWN	NAME	SIGNATURE	DATE			TITLE: <b>16 MM TRANSITION ASSEMBLY/BOM</b>					
CHK'D						DWG NO. <b>EXPLODED VIEW</b> <span style="float: right;">A3</span>					
APP'VD											
MFG											
Q.A											
					MATERIAL:	SCALE: 1:20					
					WEIGHT:						



FLANGE FACE FLUSH TO TRANSITION FACE

WELD ALL AROUND THIS SIDE ONLY

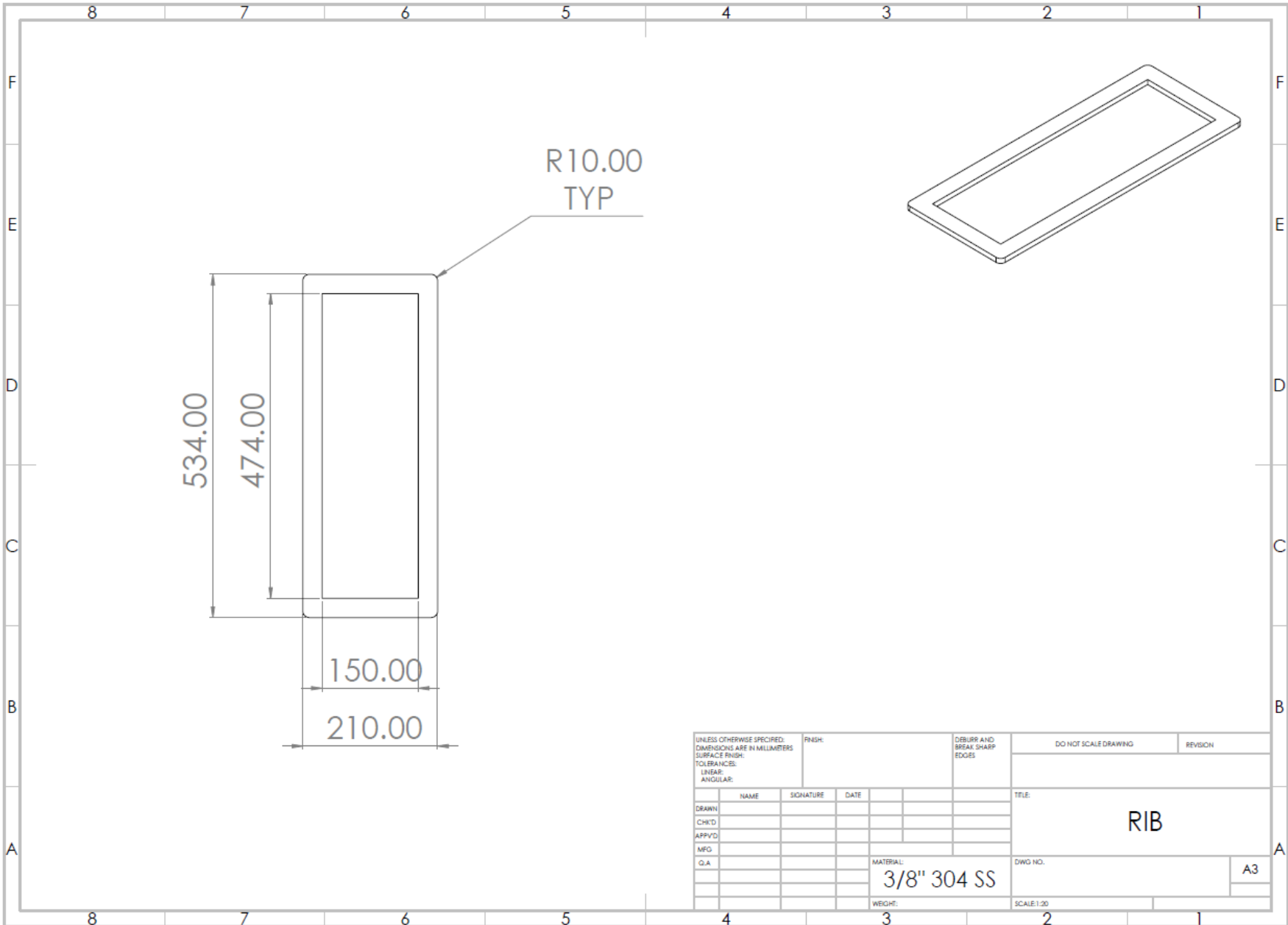
WELD ALL AROUND THIS SIDE ONLY



NOTE:  
IMPORTANT TO MAINTAIN  
GEOMETRIC SHAPE  
MINIMAL WELD DISTORTION  
IS REQUIRED

UNLESS OTHERWISE SPECIFIED: DIMENSIONS ARE IN MILLIMETERS		FINISH:		DEBURR AND BREAK SHARP EDGES		DO NOT SCALE DRAWING		REVISION	
SURFACE FINISH:									
TOLERANCES:									
LINEAR:									
ANGULAR:									
DRAWN	NAME	SIGNATURE	DATE			TITLE: 16 MM TRANSITION ASSEMBLY			
CHK'D									
APP'VD									
MFG									
Q.A					MATERIAL:	DWG NO.		WELD CALL-OUT A3	
					WEIGHT:	SCALE:1:20			





R10.00  
TYP

534.00

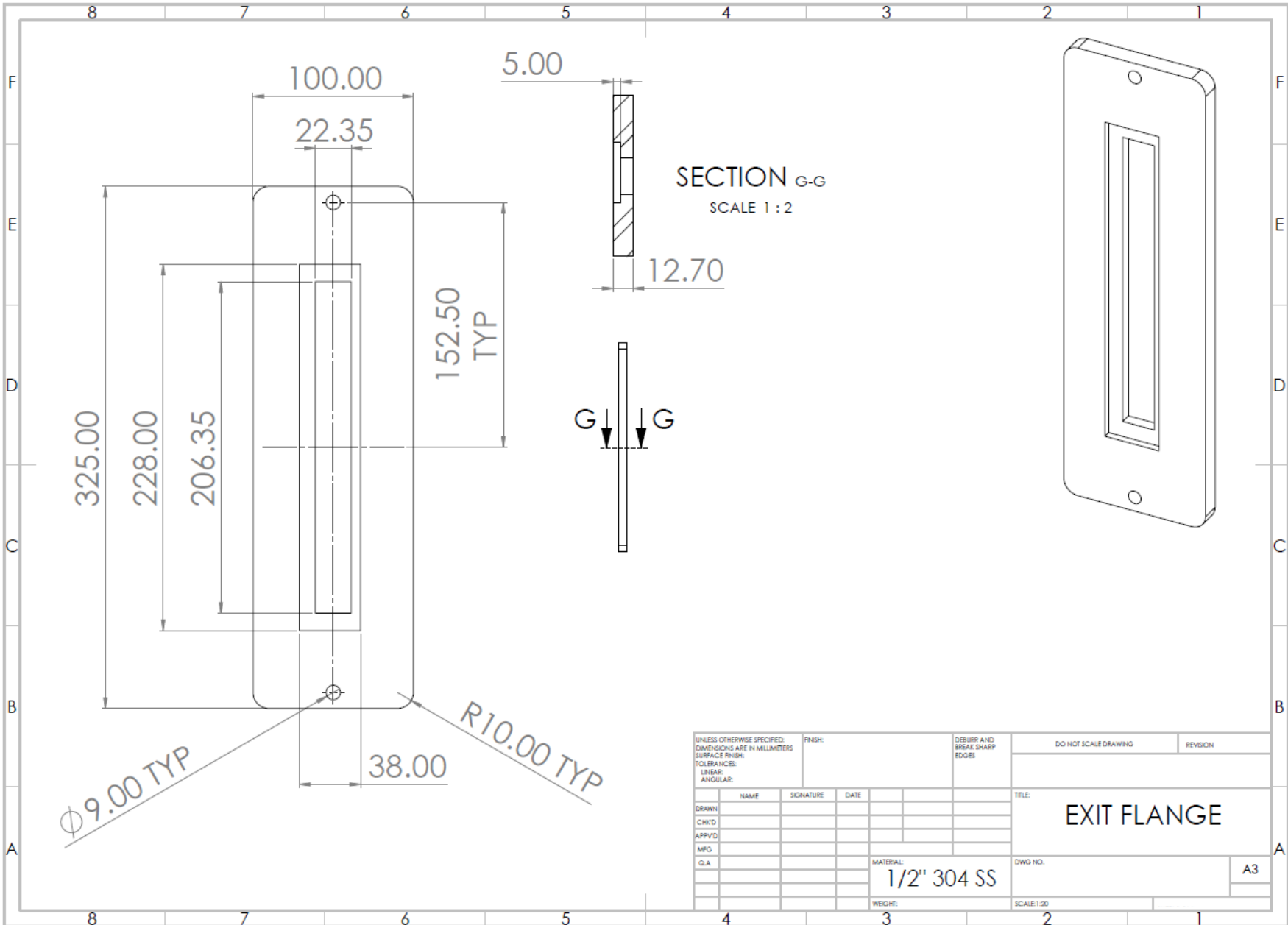
474.00

150.00

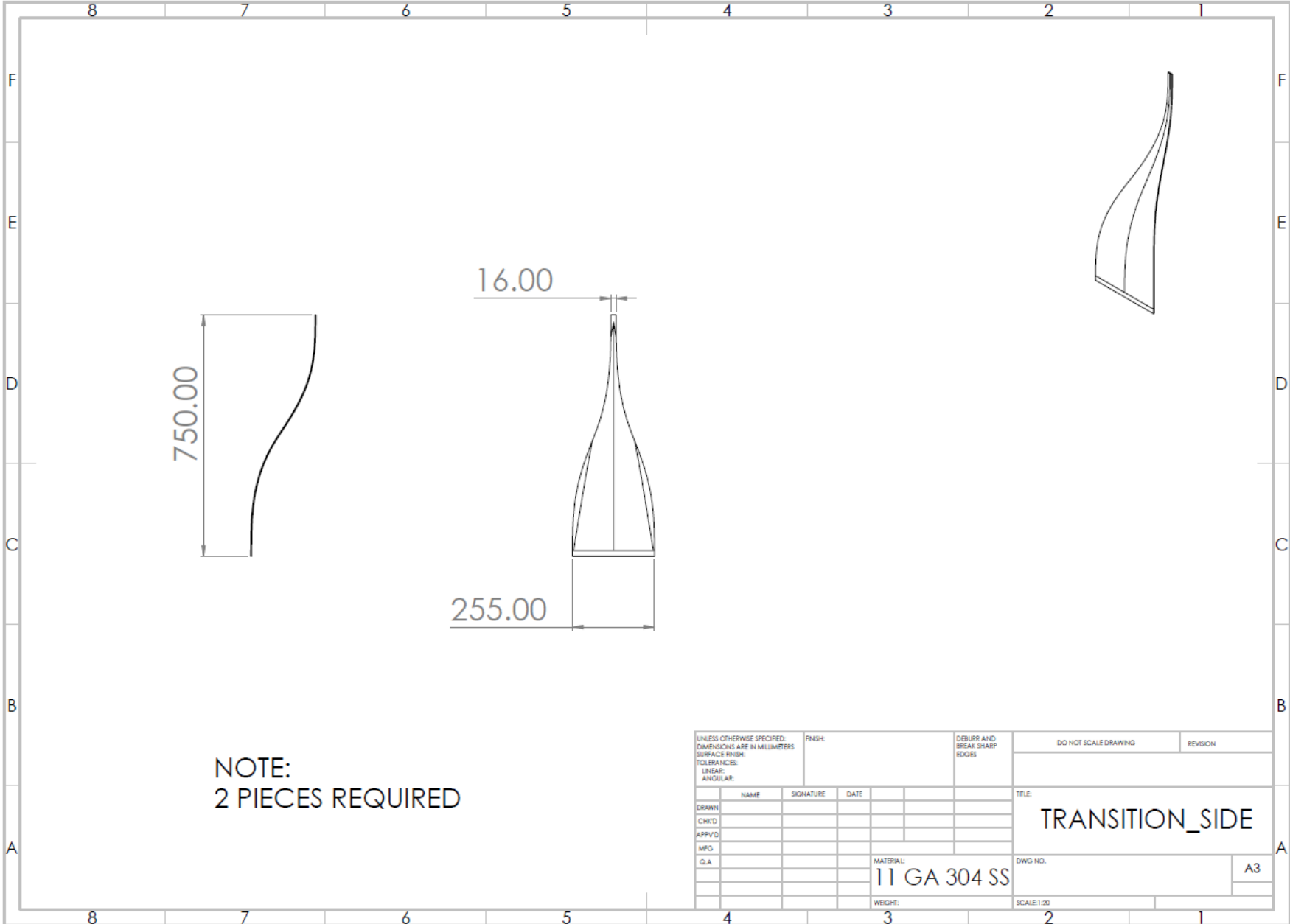
210.00

UNLESS OTHERWISE SPECIFIED: DIMENSIONS ARE IN MILLIMETERS				FINISH:		DEBURR AND BREAK SHARP EDGES		DO NOT SCALE DRAWING		REVISION	
SURFACE FINISH:											
TOLERANCES:											
LINEAR:											
ANGULAR:											
DRAWN		SIGNATURE		DATE				TITLE:		RIB	
CHK'D											
APP'VD											
MFG											
Q.A											
						MATERIAL: 3/8" 304 SS		DWG NO.		A3	
						WEIGHT:		SCALE: 1:20			



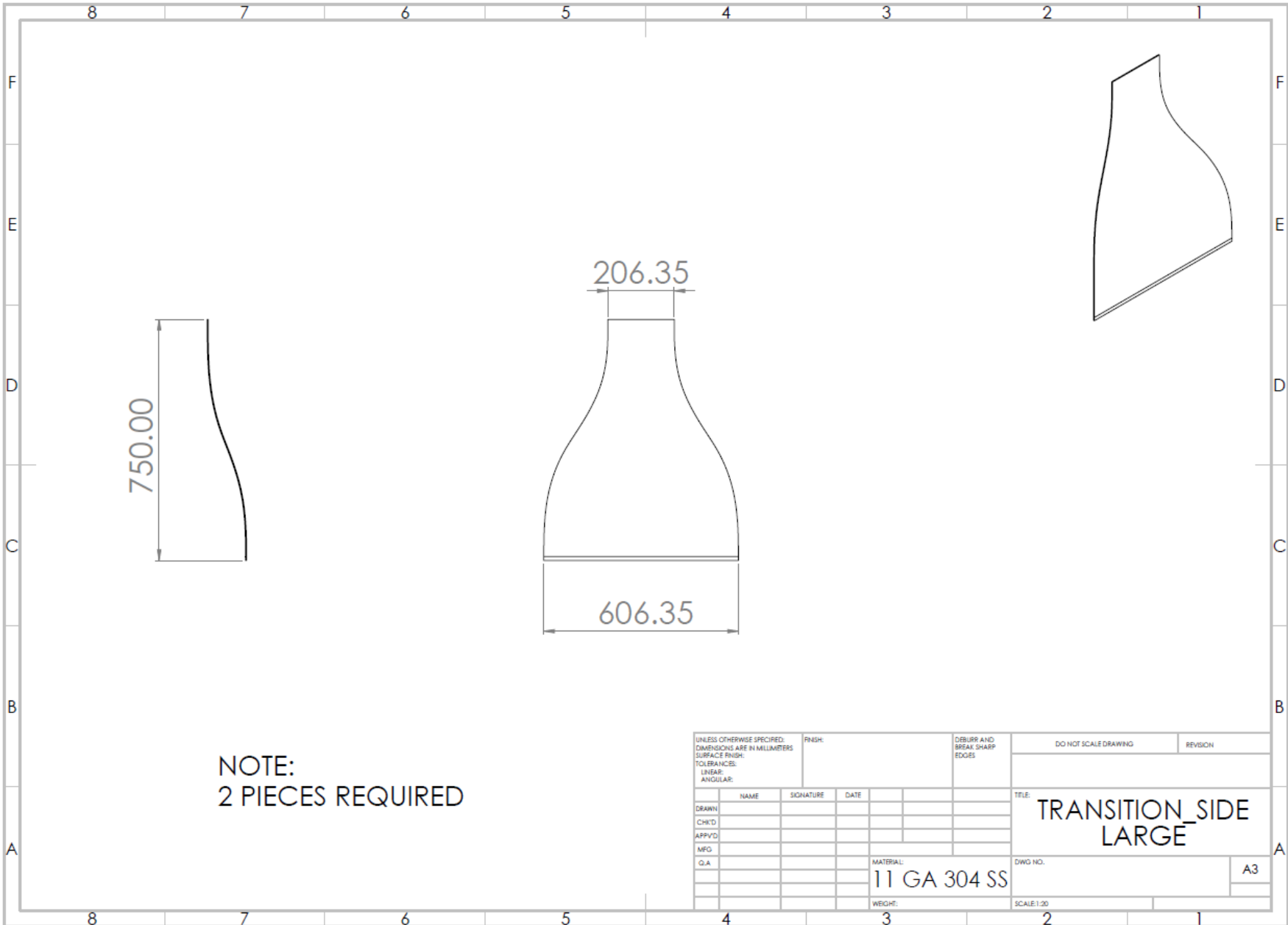


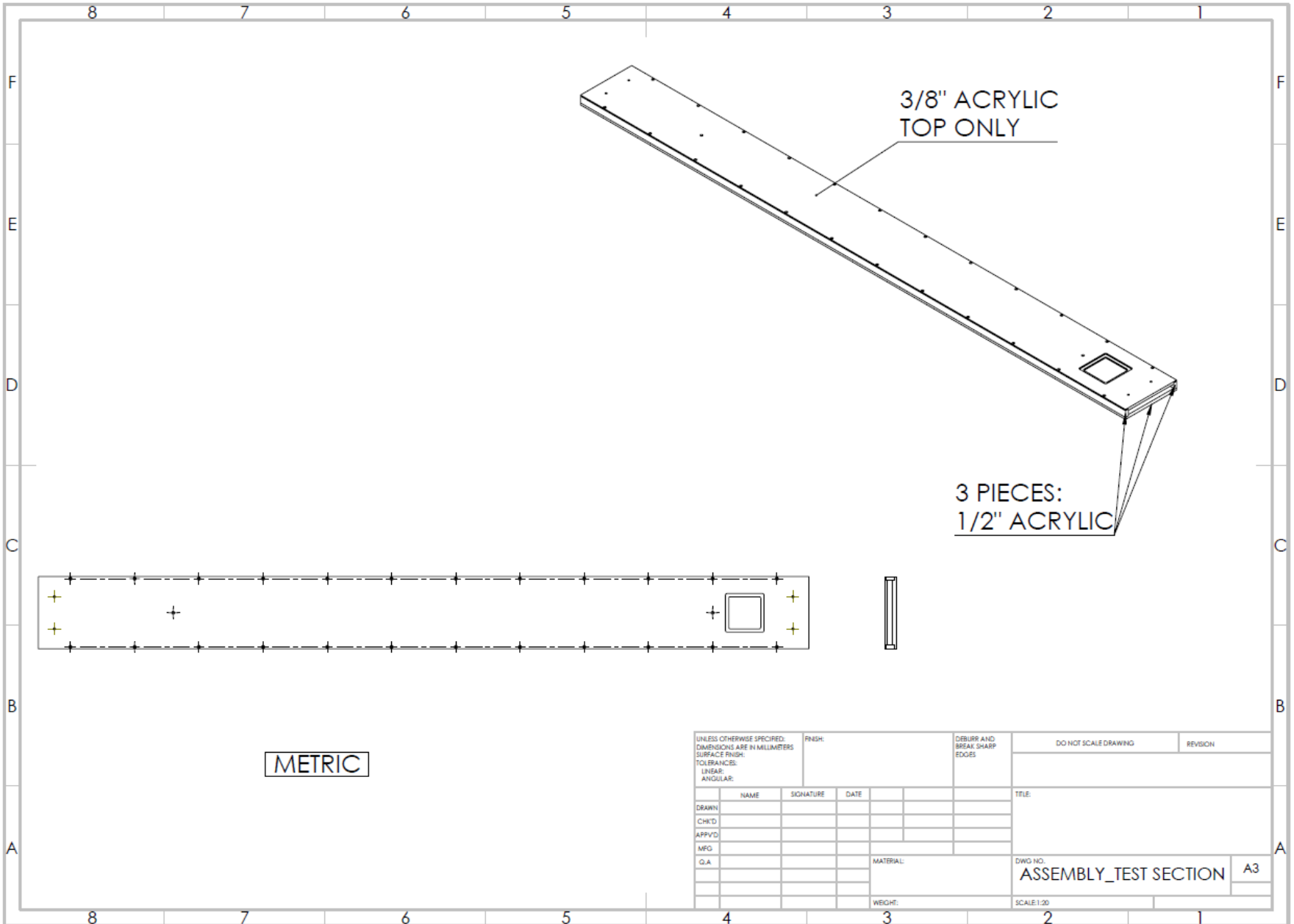
UNLESS OTHERWISE SPECIFIED: DIMENSIONS ARE IN MILLIMETERS SURFACE FINISH: TOLERANCES: LINEAR: ANGULAR:				FINISH:	DEBURR AND BREAK SHARP EDGES	DO NOT SCALE DRAWING	REVISION
DRAWN	NAME	SIGNATURE	DATE			TITLE: <b>EXIT FLANGE</b>	
CHK'D							
APP'VD							
MFG							
Q.A					MATERIAL: <b>1/2" 304 SS</b>	DWG NO.	A3
					WEIGHT:	SCALE: 1:20	



NOTE:  
2 PIECES REQUIRED

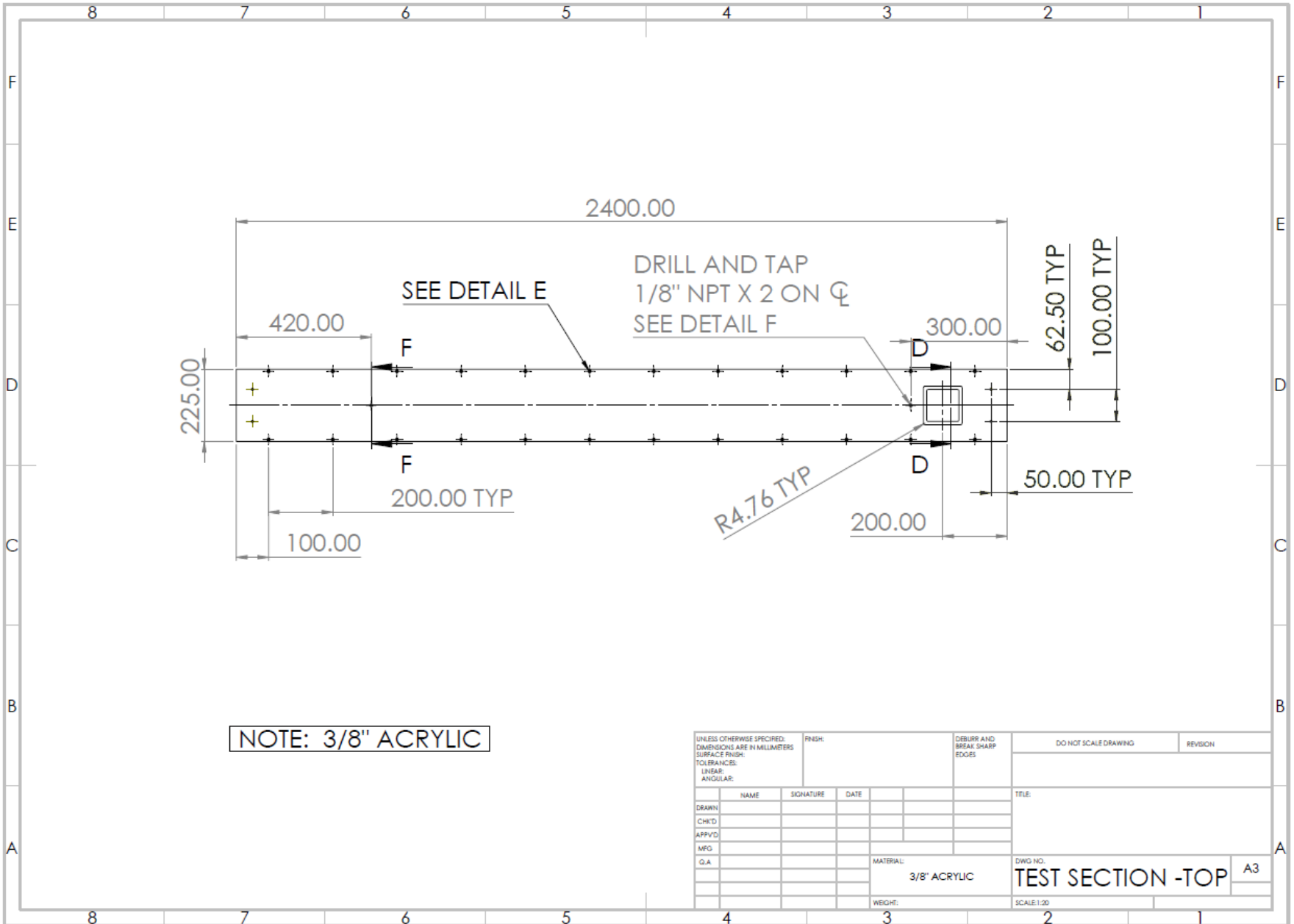
UNLESS OTHERWISE SPECIFIED: DIMENSIONS ARE IN MILLIMETERS				FINISH:		DEBURR AND BREAK SHARP EDGES		DO NOT SCALE DRAWING		REVISION	
SURFACE FINISH:				TOLERANCES:		LINEAR:		ANGULAR:		TITLE:	
DRAWN				NAME		SIGNATURE		DATE		TRANSITION_SIDE	
CHK'D											
APP'VD											
MFG											
Q.A											
								MATERIAL: 11 GA 304 SS		DWG NO.	
										A3	
								WEIGHT:		SCALE: 1:20	





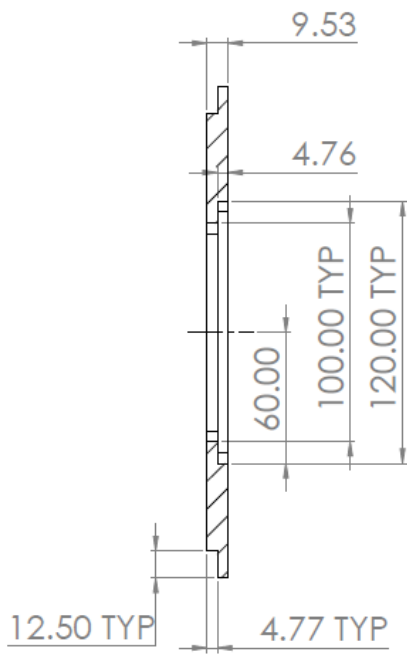
METRIC

UNLESS OTHERWISE SPECIFIED: DIMENSIONS ARE IN MILLIMETERS SURFACE FINISH: TOLERANCES: LINEAR: ANGULAR:				FINISH:		DEBURR AND BREAK SHARP EDGES		DO NOT SCALE DRAWING		REVISION	
DRAWN				SIGNATURE		DATE		TITLE:			
CHK'D											
APP'VD											
MFG											
Q.A								MATERIAL:		DWG NO.	
										ASSEMBLY_TEST SECTION	
										A3	
						WEIGHT:		SCALE:1:20			



NOTE: 3/8" ACRYLIC

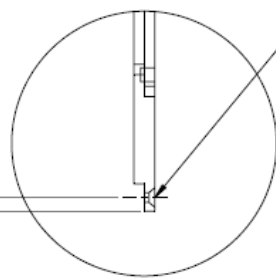
UNLESS OTHERWISE SPECIFIED: DIMENSIONS ARE IN MILLIMETERS SURFACE FINISH: TOLERANCES: LINEAR: ANGULAR:		FINISH:	DEBURR AND BREAK SHARP EDGES	DO NOT SCALE DRAWING	REVISION
NAME	SIGNATURE	DATE		TITLE:	
DRAWN					
CHK'D					
APP'VD					
MFG					
Q.A					
MATERIAL: 3/8" ACRYLIC			DWG NO.:	TEST SECTION -TOP	
WEIGHT:			SCALE:1:20	A3	



SECTION D-D  
SCALE 1 : 2



6.25



DETAIL E  
SCALE 1 : 2

BLIND TAP  
1/8" NPT  $\nabla$  7MM



A

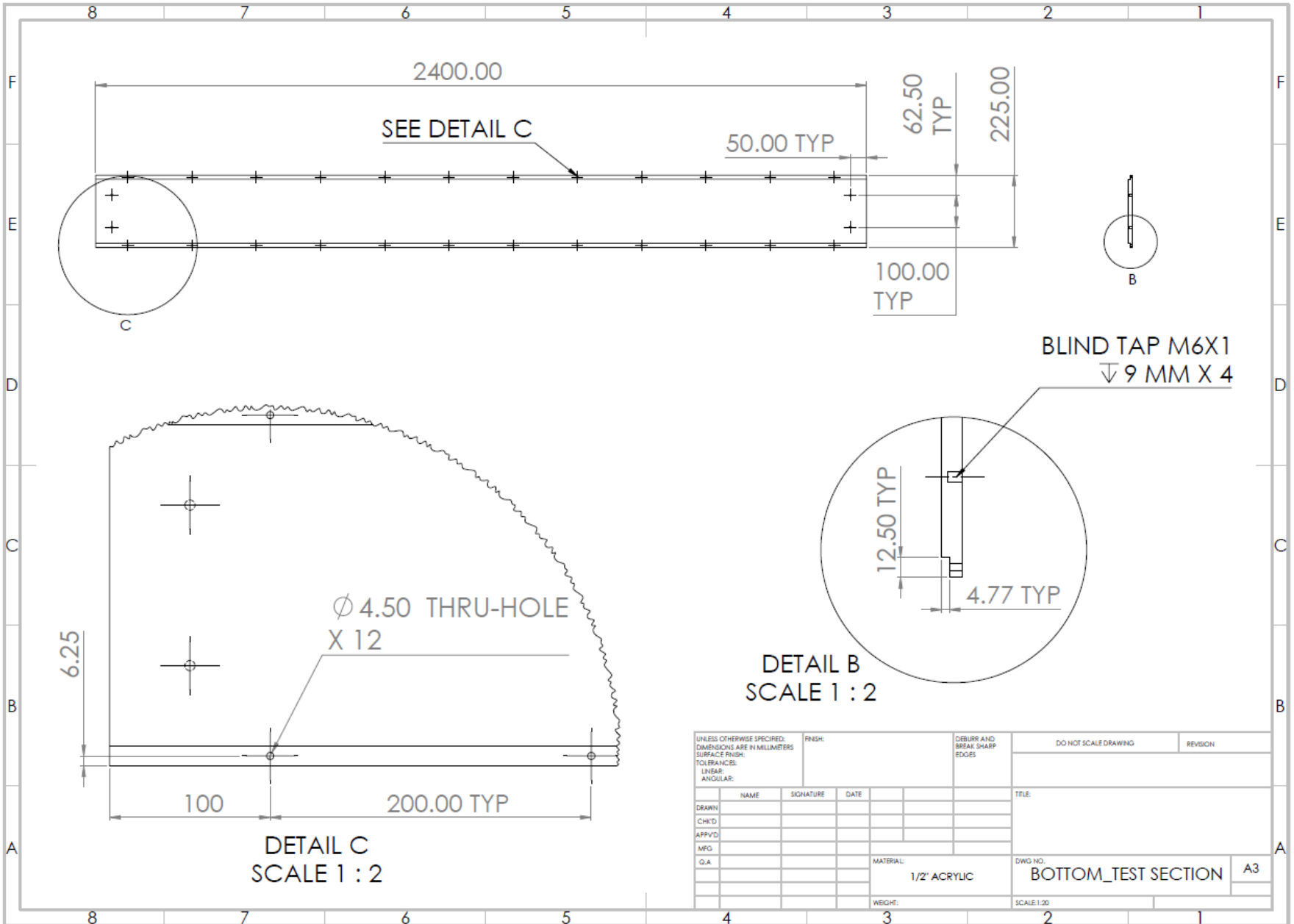
$\phi$ .75 THRU  
DRILL FROM DATUM A:  
DRILL BREAK THRU MUST BE  
OPPOSITE DATUM

SECTION F-F  
SCALE 1 : 2

$\phi$  4.5 THRU  
 $\nabla$  82° COUNTERSINK  
 $\nabla$  3 MM X 12

UNLESS OTHERWISE SPECIFIED: DIMENSIONS ARE IN MILLIMETERS SURFACE FINISH: TOLERANCES: LINEAR: ANGULAR:				FINISH:	DEBURR AND BREAK SHARP EDGES	DO NOT SCALE DRAWING	REVISION
						<b>DETAIL VIEWS</b>	
NAME	SIGNATURE	DATE				TITLE:	
DRAWN							
CHK'D							
APP'VD							
MFG							
Q.A					MATERIAL:	DWG NO.	
						<b>TOP_TEST SECTION</b>	A3
					WEIGHT:	SCALE:1:20	





2400.00

SEE DETAIL C

50.00 TYP

62.50 TYP

225.00

100.00 TYP

BLIND TAP M6X1  
 ∇ 9 MM X 4

12.50 TYP

4.77 TYP

DETAIL B  
 SCALE 1 : 2

∅ 4.50 THRU-HOLE  
 X 12

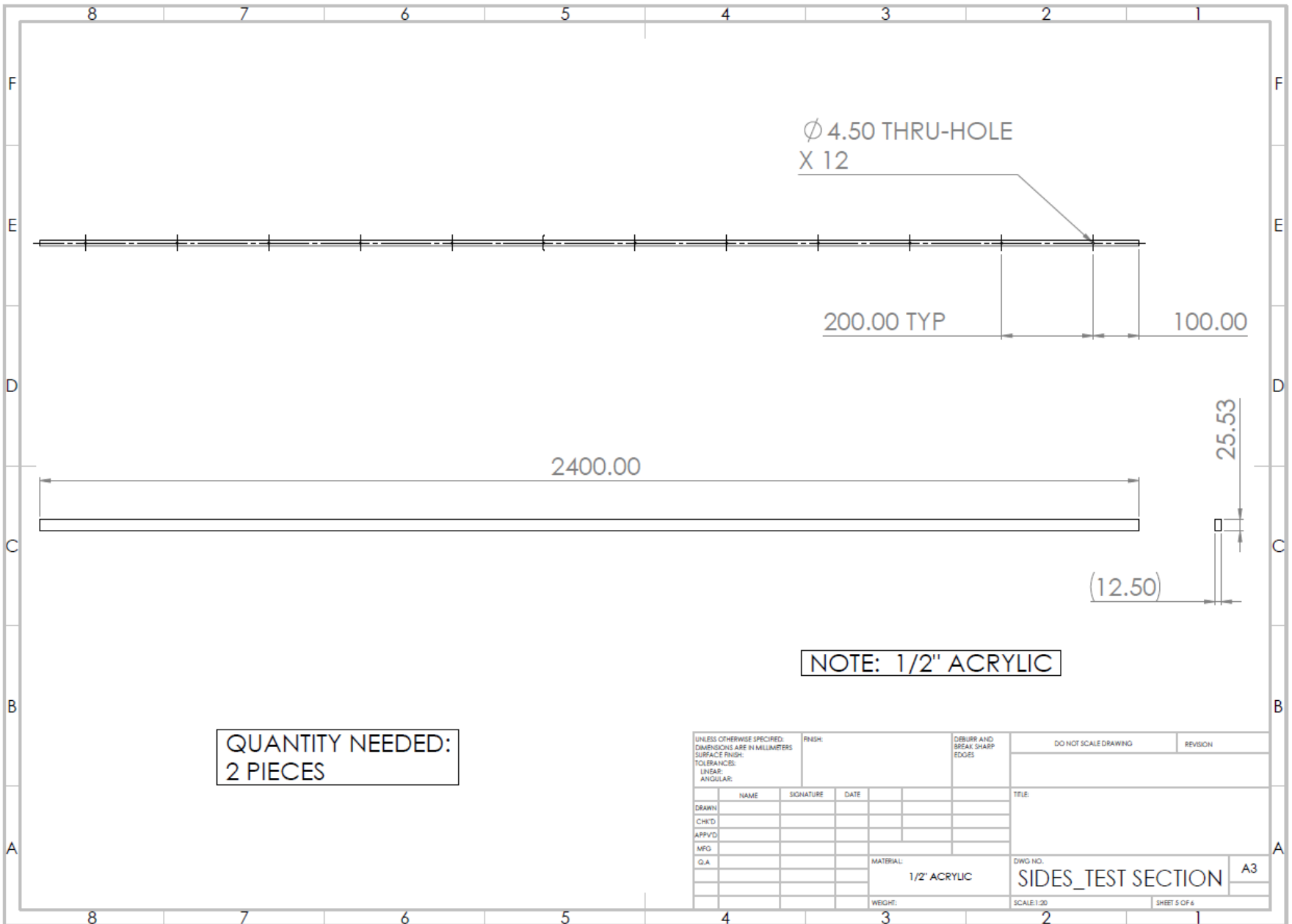
6.25

100

200.00 TYP

DETAIL C  
 SCALE 1 : 2

UNLESS OTHERWISE SPECIFIED: DIMENSIONS ARE IN MILLIMETERS		FINISH:		DEBURR AND BREAK SHARP EDGES		DO NOT SCALE DRAWING		REVISION	
SURFACE FINISH:									
TOLERANCES:									
LINEAR:									
ANGULAR:									
DRAWN	NAME	SIGNATURE	DATE			TITLE:			
CHK'D									
APP'VD									
MFG									
Q.A						MATERIAL:		DWG NO.	
						1/2" ACRYLIC		BOTTOM_TEST SECTION	
						WEIGHT:		SCALE: 1:20	
								A3	



Ø 4.50 THRU-HOLE  
X 12

200.00 TYP

100.00

2400.00

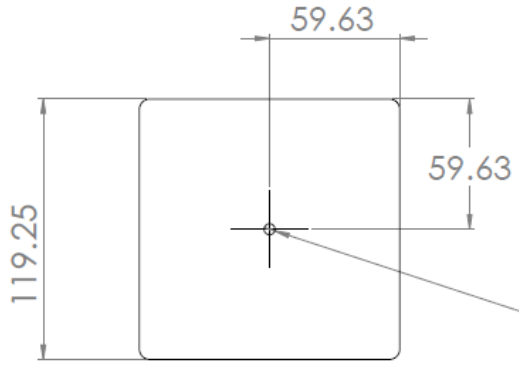
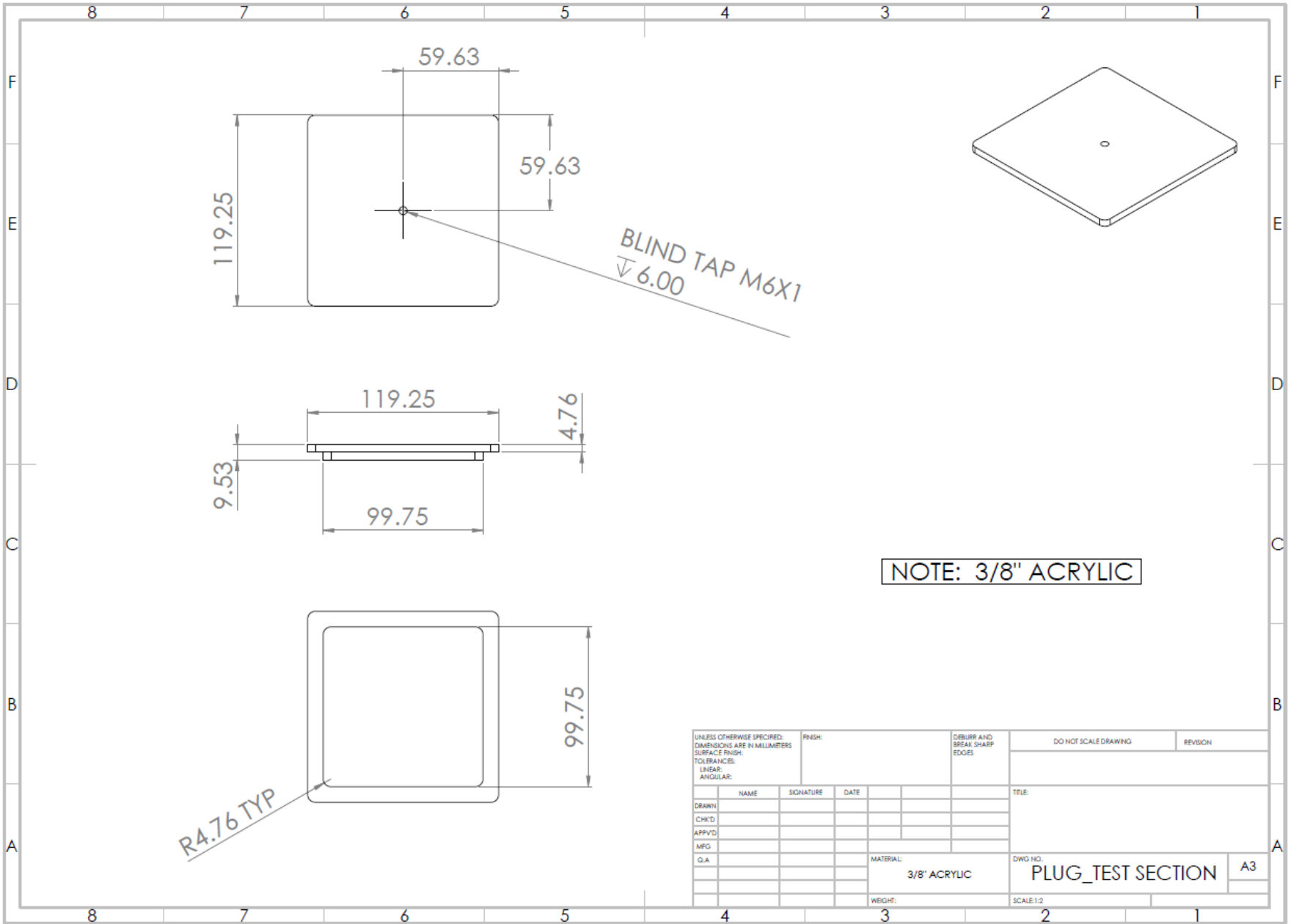
25.53

(12.50)

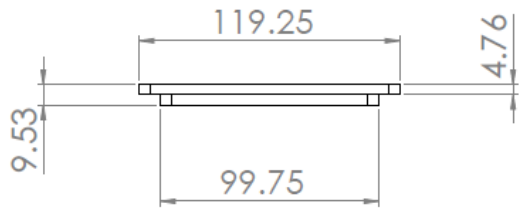
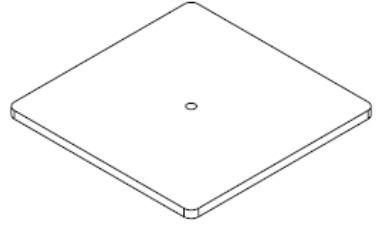
NOTE: 1/2" ACRYLIC

QUANTITY NEEDED:  
2 PIECES

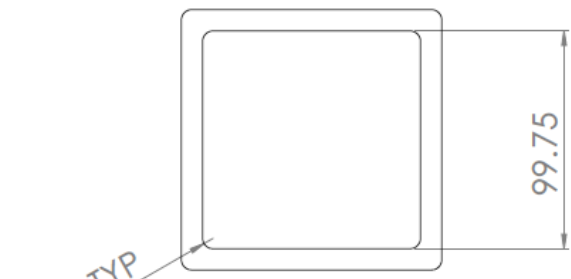
UNLESS OTHERWISE SPECIFIED: DIMENSIONS ARE IN MILLIMETERS SURFACE FINISH: TOLERANCES: LINEAR: ANGULAR:				FINISH:		DEBURR AND BREAK SHARP EDGES		DO NOT SCALE DRAWING		REVISION	
DRAWN	NAME	SIGNATURE	DATE					TITLE:			
CHK'D								DWG NO. <b>SIDES_TEST SECTION</b> A3			
APP'VD											
MFG											
Q.A											
						MATERIAL: 1/2" ACRYLIC		SCALE: 1:20		SHEET 5 OF 6	



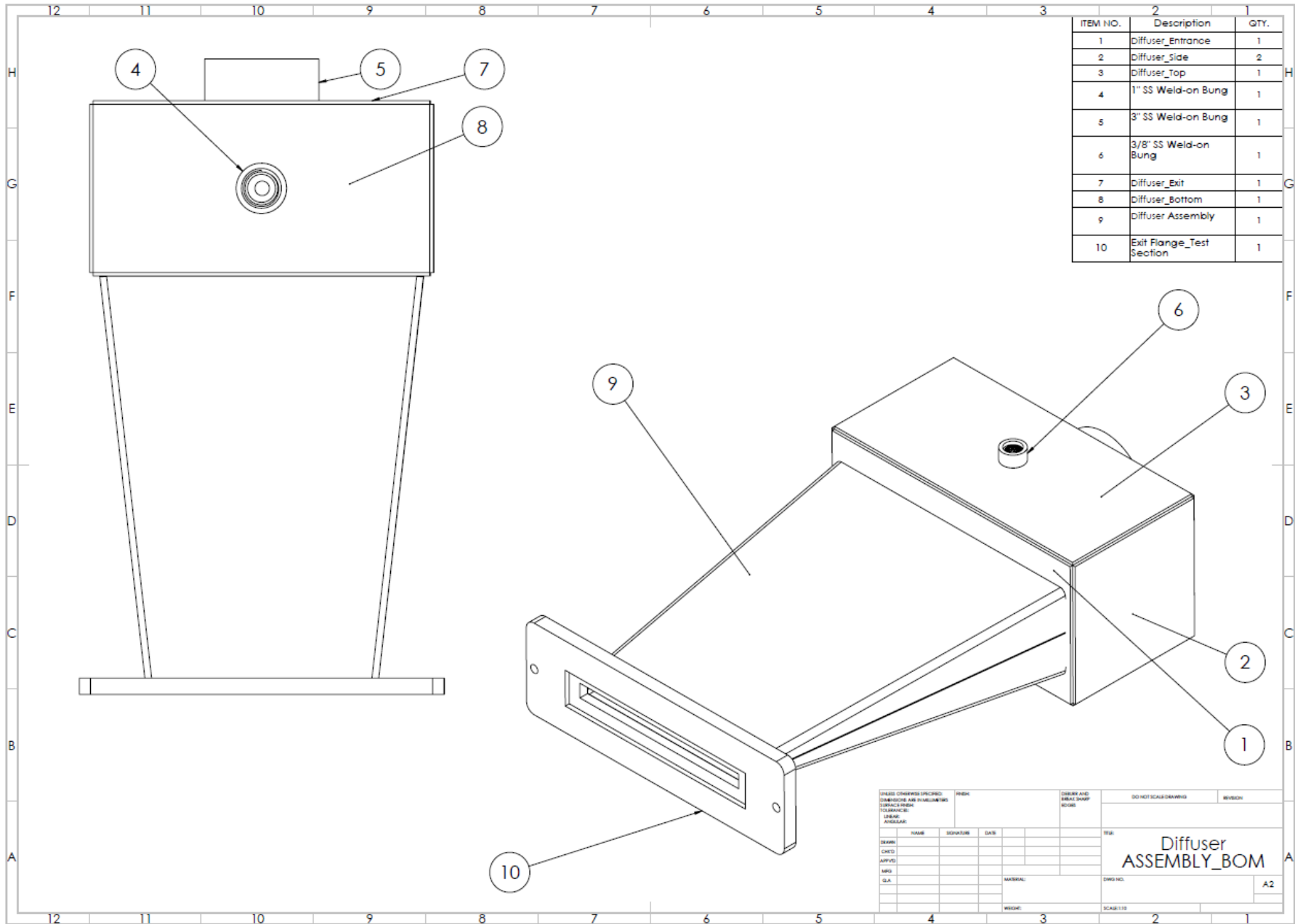
BLIND TAP M6X1  
 ↓ 6.00



NOTE: 3/8" ACRYLIC

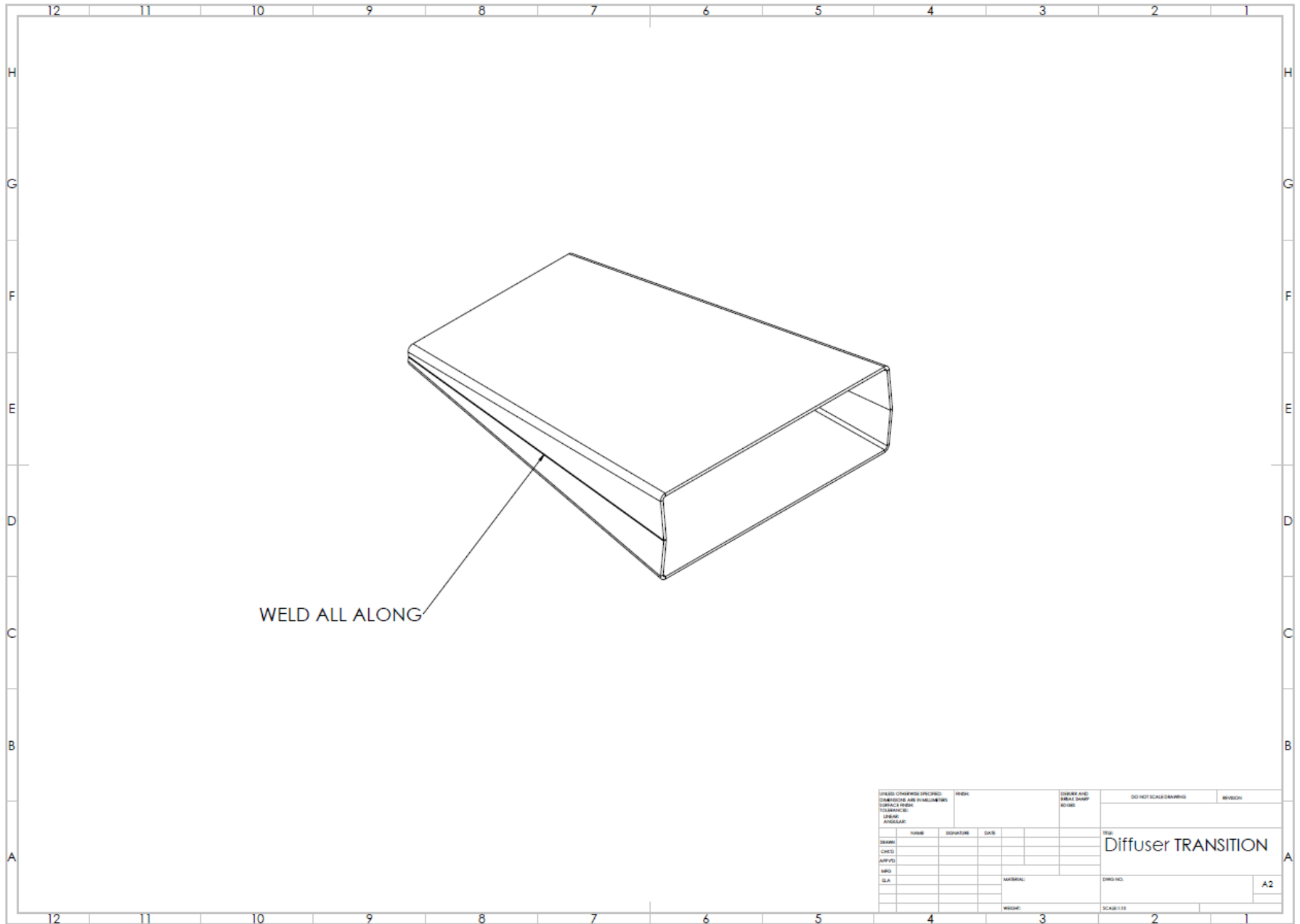


UNLESS OTHERWISE SPECIFIED: DIMENSIONS ARE IN MILLIMETERS SURFACE FINISH: TOLERANCES: LINEAR: ANGULAR:				FINISH:		DEBURR AND BREAK SHARP EDGES		DO NOT SCALE DRAWING		REVISION	
DRAWN	NAME	SIGNATURE	DATE					TITLE:			
CHK'D											
APP'VD											
MFG											
Q/A											
						MATERIAL:	3/8" ACRYLIC		DWG NO.:		PLUG_TEST SECTION
						WEIGHT:			SCALE: 1:2		A3

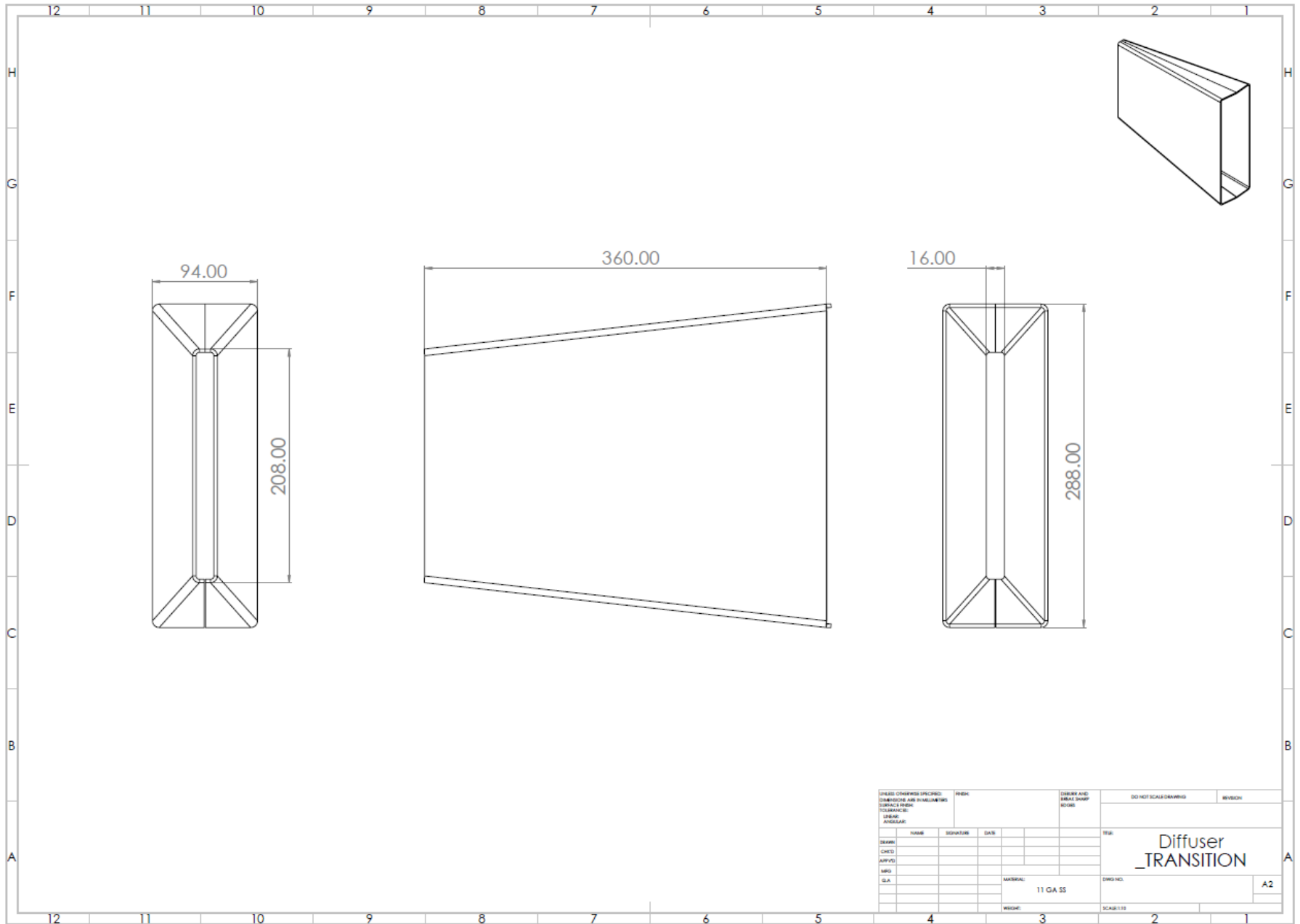


ITEM NO.	Description	QTY.
1	Diffuser_Entrance	1
2	Diffuser_Side	2
3	Diffuser_Top	1
4	1\" SS Weld-on Bung	1
5	3\" SS Weld-on Bung	1
6	3/8\" SS Weld-on Bung	1
7	Diffuser_Exit	1
8	Diffuser_Bottom	1
9	Diffuser Assembly	1
10	Exit Flange_Test Section	1

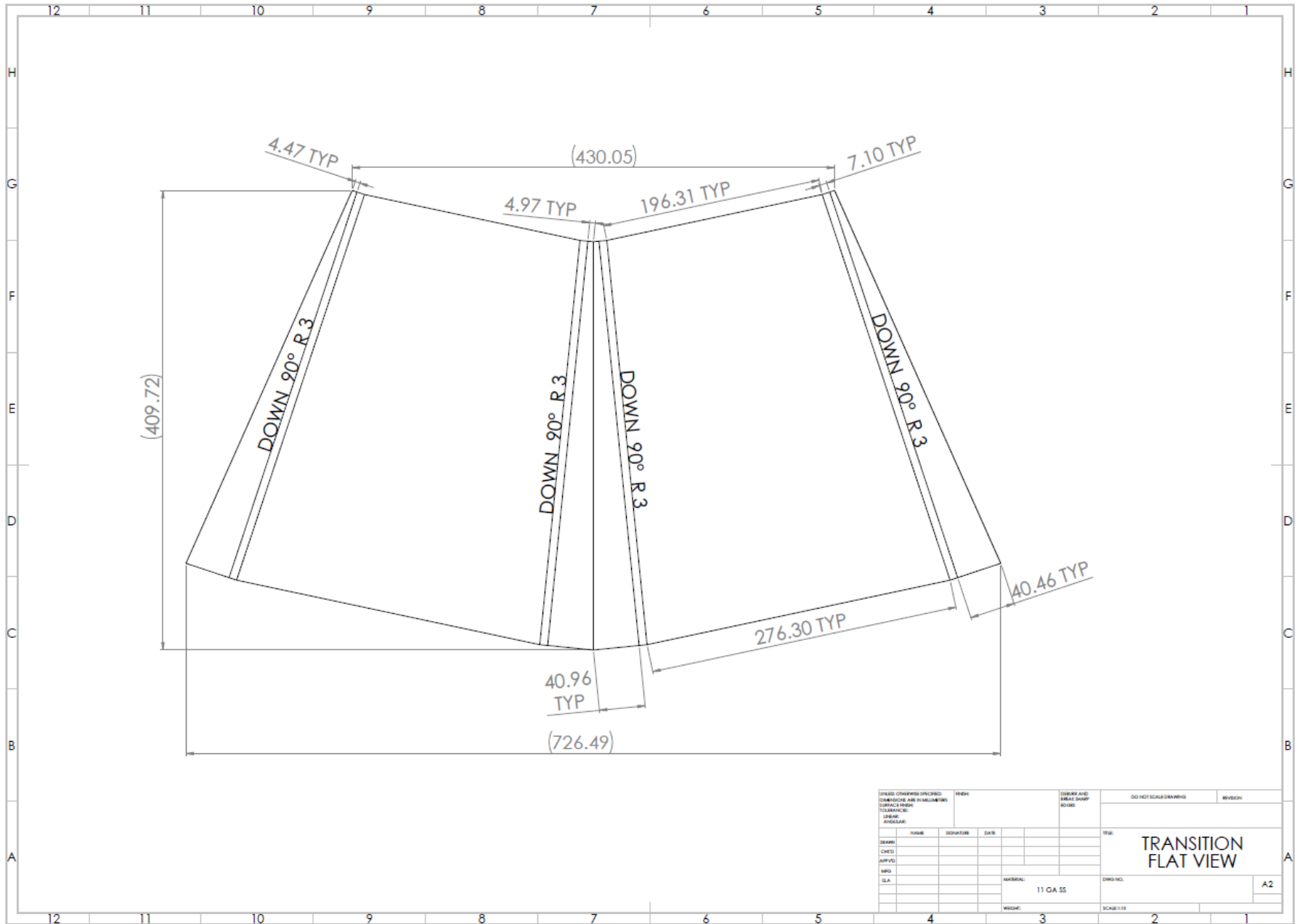
UNLESS OTHERWISE SPECIFIED: DIMENSIONS ARE IN MILLIMETERS TOLERANCES: FRACTIONS DECIMALS				FINISH	DO NOT SCALE DRAWING	WISCH	
DATE:	NAME:	DEPARTMENT:	DATE:		REV:		
APP'VD:					<b>Diffuser ASSEMBLY_BOM</b>		
MFG:				DWG NO.:			A2
QA:				SCALE: 1:1			



UNLESS OTHERWISE SPECIFIED: DIMENSIONS ARE IN MILLIMETERS TOLERANCE: FRACTIONS: DECIMALS: ANGLES:			UNIT:		DRAWN AND CHECKED BY:		DATE:		
DESIGNER:	NAME:	DATE:					TITLE: Diffuser TRANSITION		
DATE:							SCALE: 1:1		
MATERIAL:							SHEET NO. 1 OF 1		
							A2		



UNLESS OTHERWISE SPECIFIED: DIMENSIONS ARE IN MILLIMETERS TOLERANCES UNLESS SPECIFIED: FRACTIONS DECIMALS ANGLES				FINISH	DRYER AND BREATHER SCHE	DO NOT SCALE DRAWING	REVISION
DATE:	NAME:	DESIGNER:	DATE:				
DRAWN:							
CHECK:							
APP'VD:							
MFG:							
QA:							
					MATERIAL: 11 GA SS	DWG NO.:	A2
					FINISH:	SCALE: 1:10	

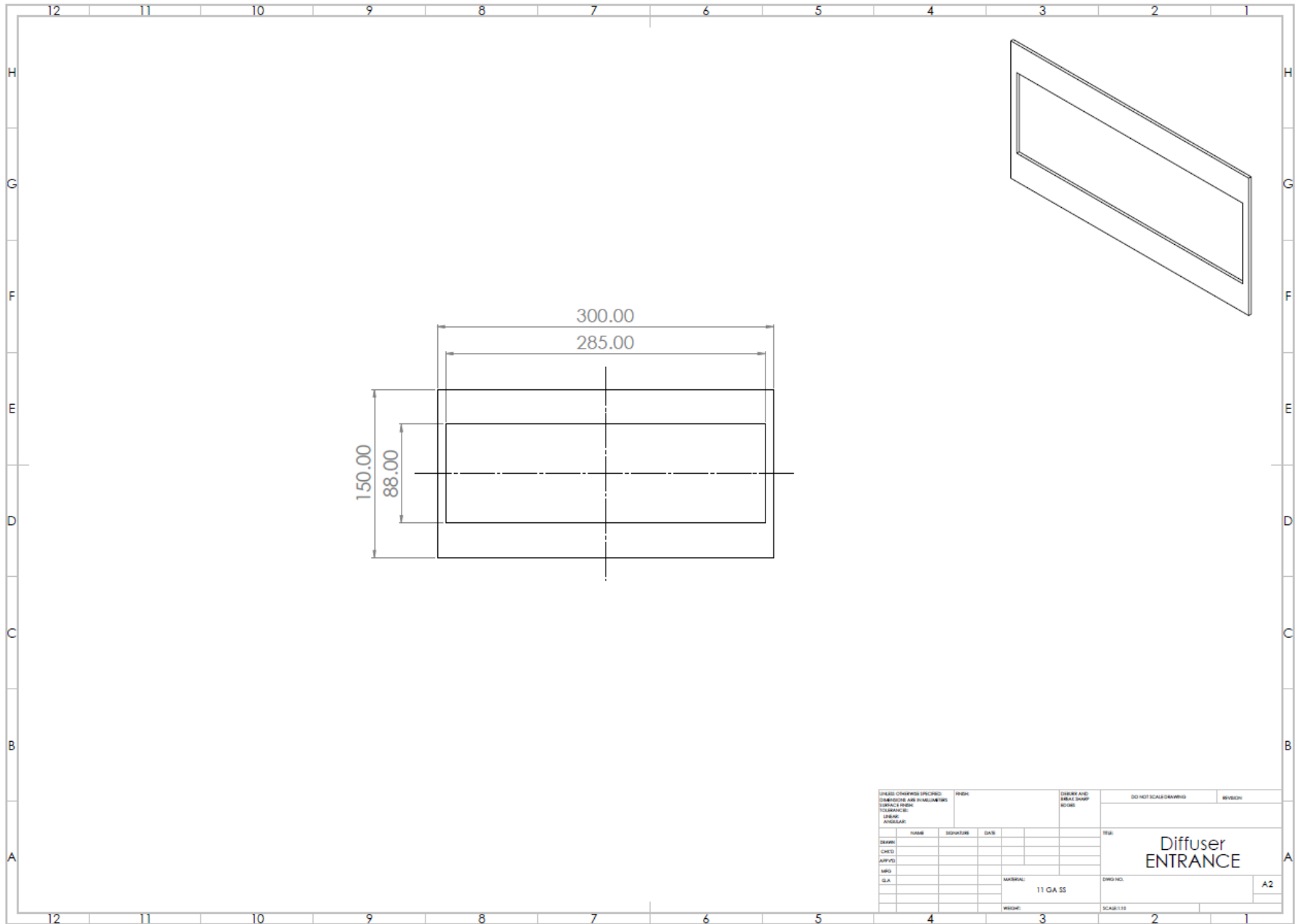


UNLESS OTHERWISE SPECIFIED: DIMENSIONS ARE IN MILLIMETERS TOLERANCES: LINEAR: ANGULAR:				FINISH:	DIMENSION AND HOLE SHARP CORNER		DO NOT SCALE DRAWING	REVISION
DESIGNER:	NAME	DATE						
CHECKED:								
APPROVED:								
MFG:								
QA:								
					MATERIAL:	11 GA SS	DWG NO.:	
					FINISH:		SCALE: 1:10	A2

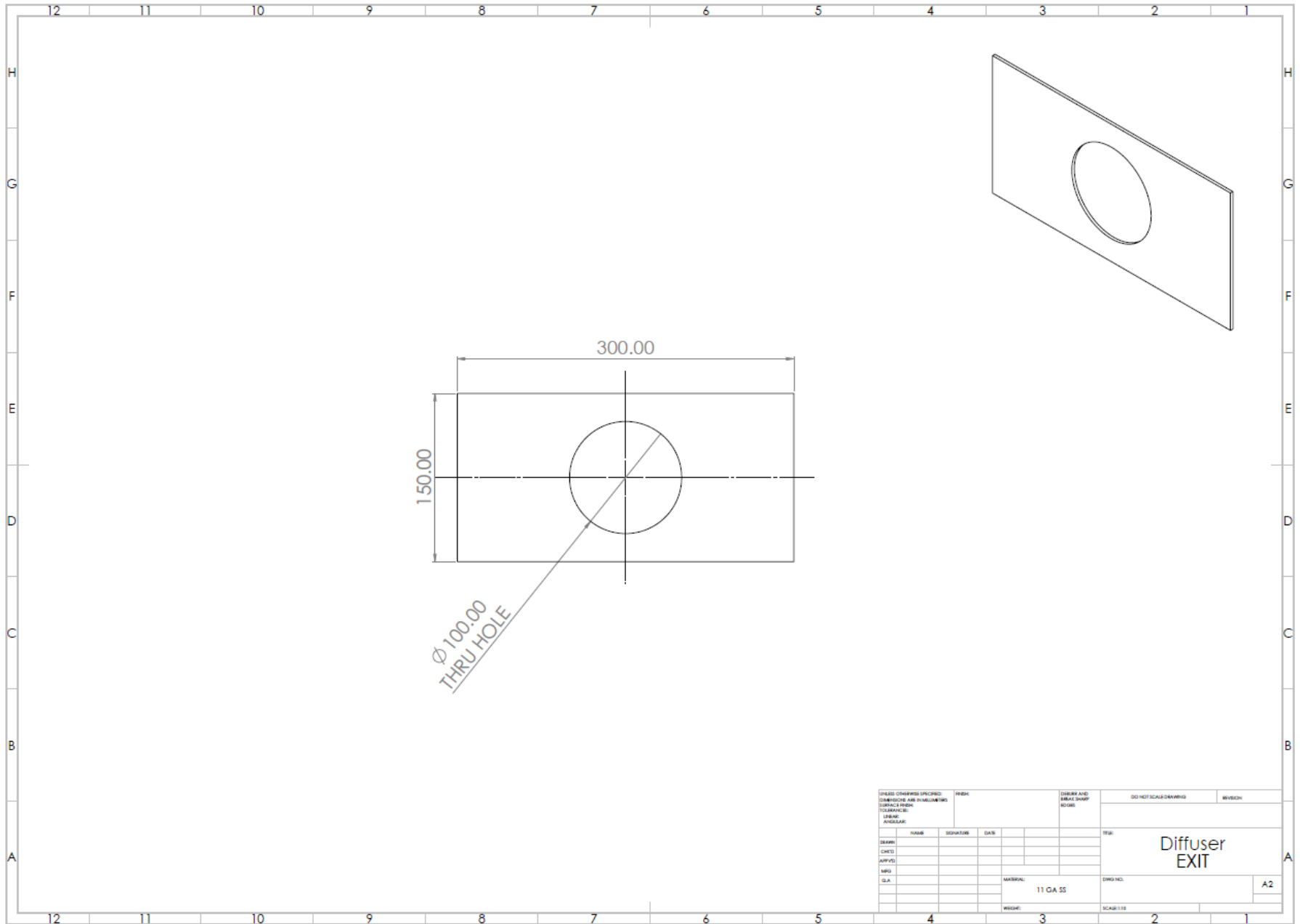




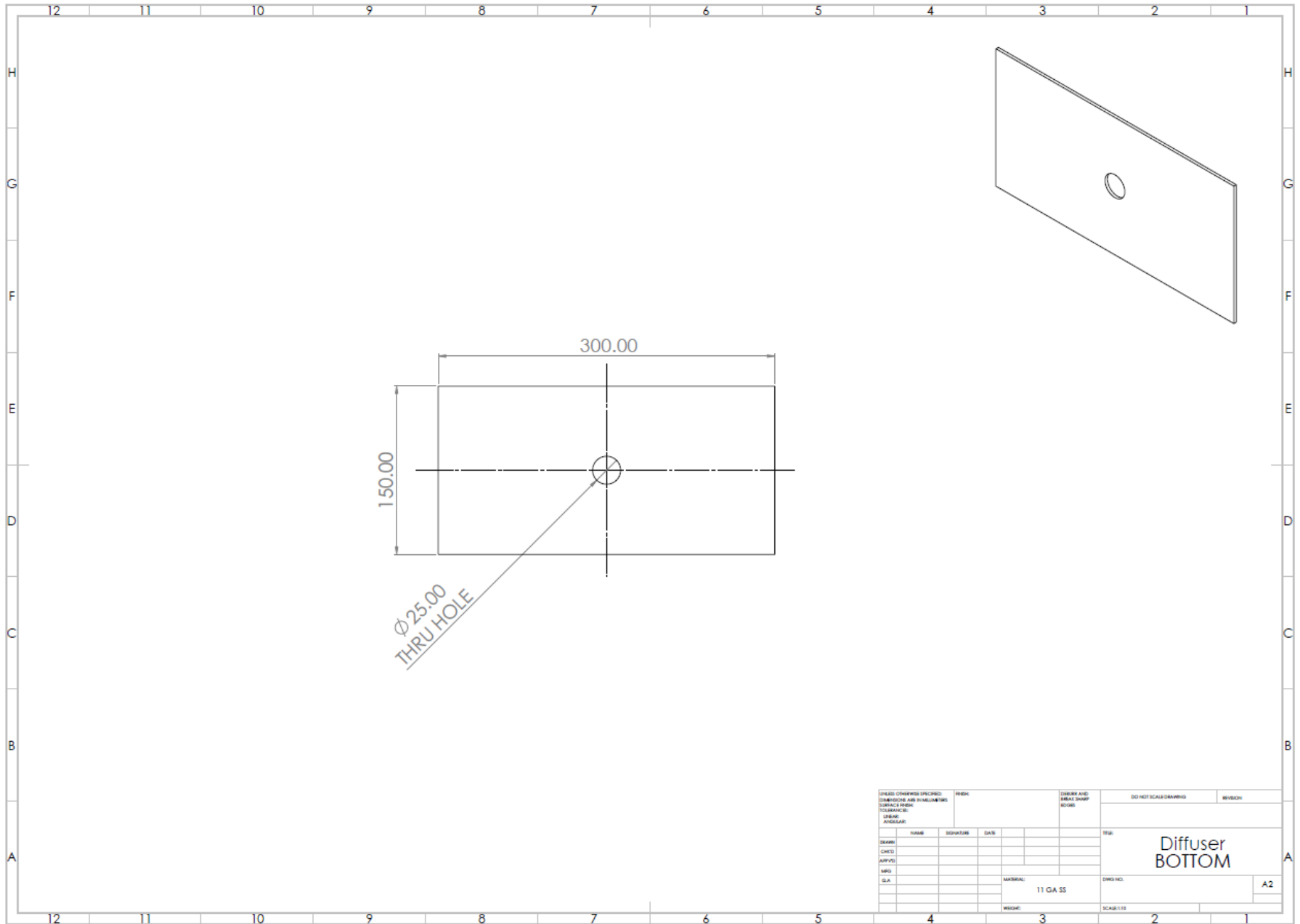




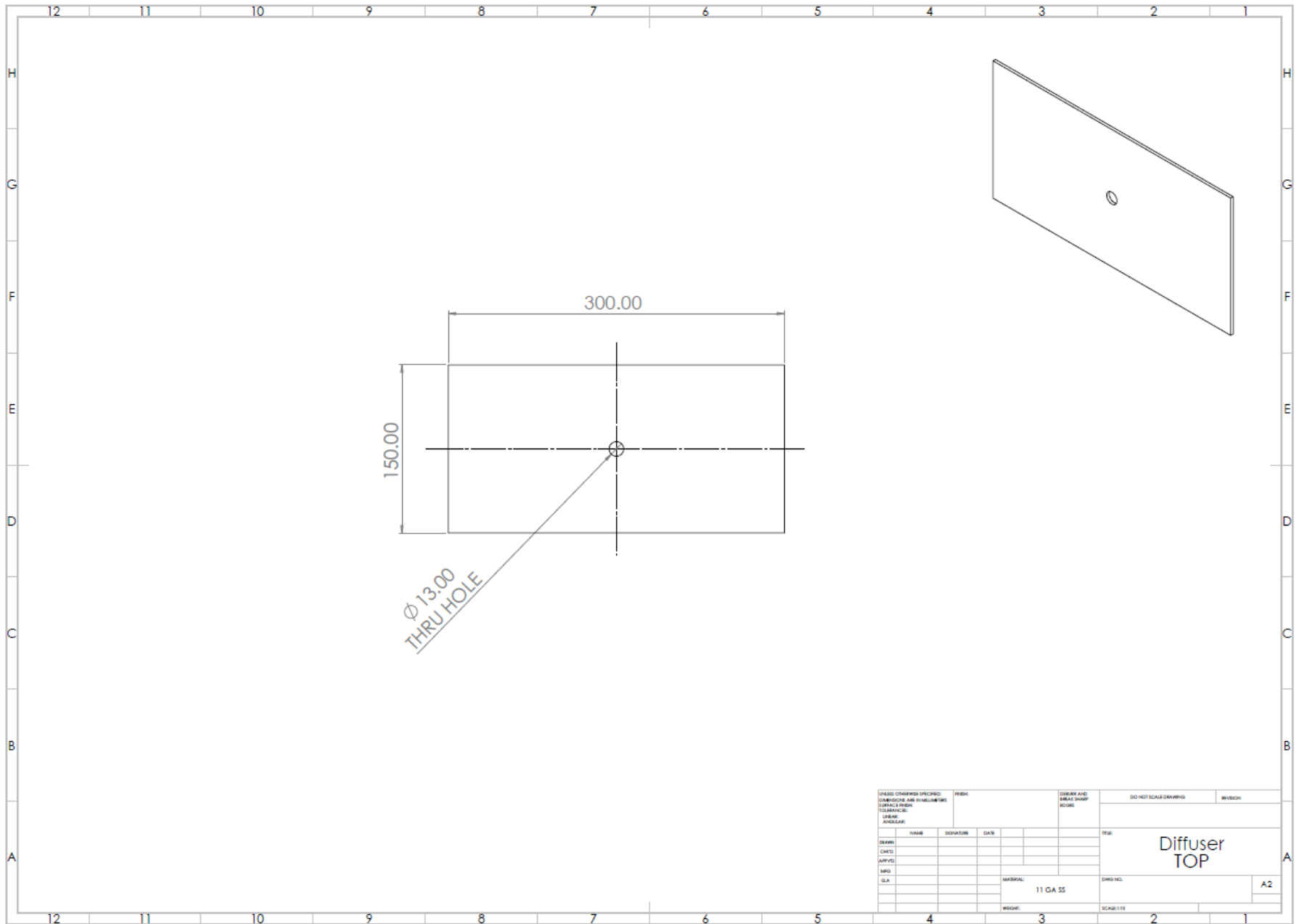
UNLESS OTHERWISE SPECIFIED: DIMENSIONS ARE IN MILLIMETERS TOLERANCE: FRACTIONS DECIMALS			FINISH		DIBBY AND BIBBY SHOP SCALE		DO NOT SCALE DRAWING		REVISION	
DATE:	NAME:	DEPARTMENT:	DATE:						TITLE: <b>Diffuser ENTRANCE</b>	
DRW:										A2
CHKD:										
APP'VD:										
MFG:										
SLA:						MATERIAL: 11 GA SS			DRWG NO.:	
						FINISH:			SCALE:	1:1



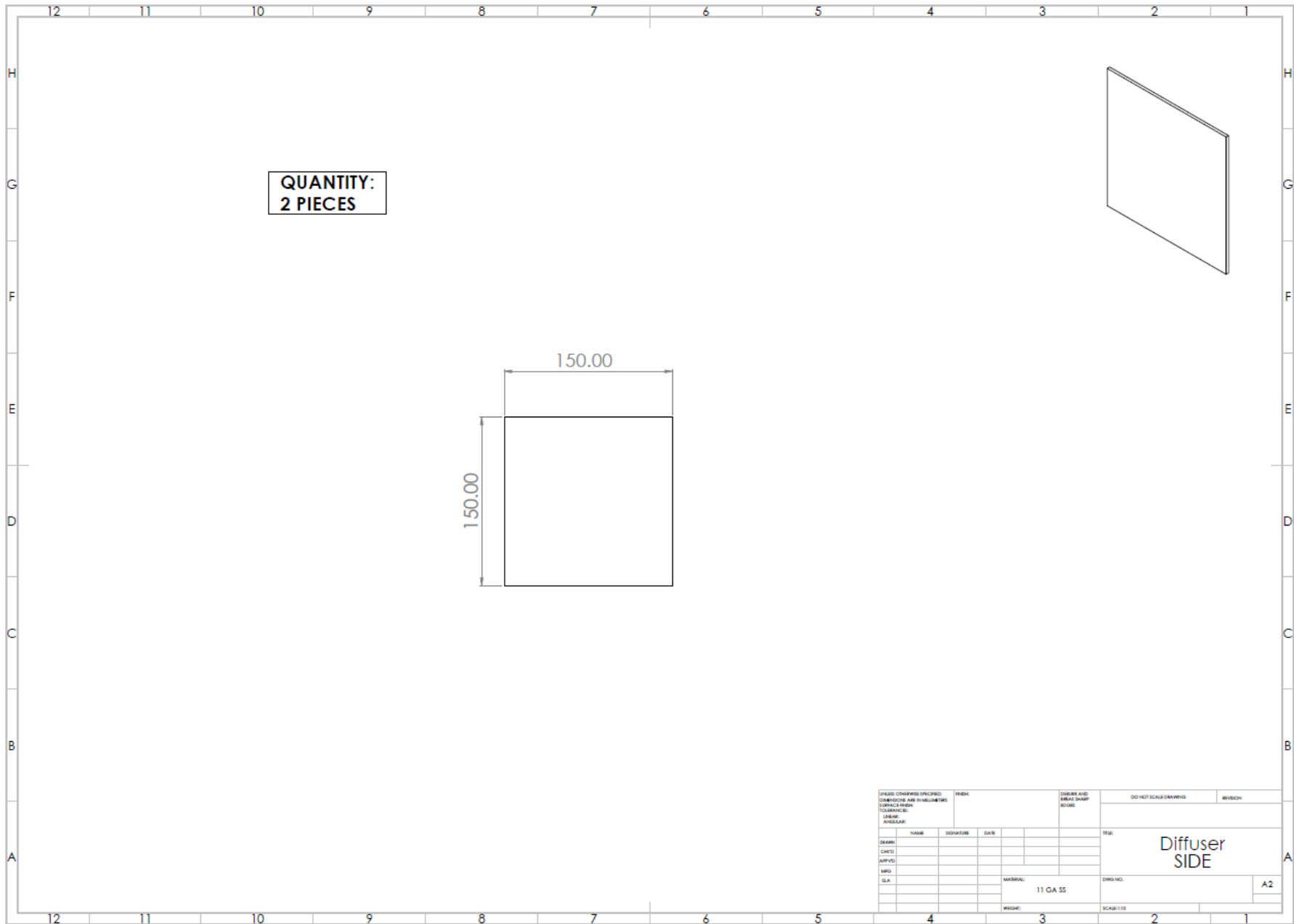
UNLESS OTHERWISE SPECIFIED: DIMENSIONS ARE IN MILLIMETERS TOLERANCES FRACTIONS DECIMALS FINISH ANGLES:			UNITS		DIMENSIONS AND HOLE SHARP CORNER		DO NOT SCALE DRAWING		REVISION	
NAME	DATE								TITLE	
DESIGN									<b>Diffuser EXIT</b>	
CHECK										
APP'VD										
MFG										
QA						MATERIAL		DWG NO.	<b>A2</b>	
						11 GA SS				
						FINISH		SCALE: 1:1		



UNLESS OTHERWISE SPECIFIED: DIMENSIONS ARE IN MILLIMETERS TOLERANCES FRACTIONS DECIMALS FINISH ANGULAR			UNITS		DIMENSIONS AND HOLE SHARP CORNER		DO NOT SCALE DRAWING		REVISION	
DATE:	NAME:	DEPARTMENT:	DATE:						TITLE:	
APP'D:									Diffuser BOTTOM	
MFG:										
QA:						MATERIAL:	11 GA SS	DWG NO.:		A2
						FINISH:		SCALE:	1:1	



UNLESS OTHERWISE SPECIFIED: DIMENSIONS ARE IN MILLIMETERS TOLERANCE: FRACTIONS DECIMALS			FINISH		DRESS AND FINISH SHARP CORNER		DO NOT SCALE DRAWING		REVISION	
DATE:	NAME:	DEPARTMENT:	DATE:						TITLE: <b>Diffuser TOP</b>	
DRW:									DWG NO.:	A2
CHKD:									SCALE:	1:1
APP'VD:										
MFG:										
QA:						MATERIAL: 11 GA SS				
						FINISH:				



UNLESS OTHERWISE SPECIFIED:				FINISH		DIMENSIONS AND HOLE SHARP CORNERS		DO NOT SCALE DRAWING		REVISION	
DIMENSIONS ARE IN MILLIMETERS											
TOLERANCE:											
FRACTIONS											
DECIMALS											
ANGLES											
NAME				DATE		TITLE					
DESIGN		DATE				Diffuser					
CHECK						SIDE					
APP'VD											
MFG											
QA						MATERIAL		DRWG NO.		A2	
						11 GA SS					
						FINISH		SCALE			
								1:1			